INFORMATION TO USERS

This manuscript has been reproduced from the microfilm master. UMI films the text directly from the original or copy submitted. Thus, some thesis and dissertation copies are in typewriter face, while others may be from any type of computer printer.

The quality of this reproduction is dependent upon the quality of the copy submitted. Broken or indistinct print, colored or poor quality illustrations and photographs, print bleedthrough, substandard margins, and improper alignment can adversely affect reproduction.

In the unlikely event that the author did not send UMI a complete manuscript and there are missing pages, these will be noted. Also, if unauthorized copyright material had to be removed, a note will indicate the deletion.

Oversize materials (e.g., maps, drawings, charts) are reproduced by sectioning the original, beginning at the upper left-hand corner and continuing from left to right in equal sections with small overlaps.

Photographs included in the original manuscript have been reproduced xerographically in this copy. Higher quality 6" x 9" black and white photographic prints are available for any photographs or illustrations appearing in this copy for an additional charge. Contact UMI directly to order.

Bell & Howell Information and Learning
300 North Zeeb Road, Ann Arbor, MI 48106-1346 USA
800-521-0600

SMALL SPATIAL AND FAST TEMPORAL IONOSPHERE-MAGNETOSPHERE COUPLING PROCESSES

A

THESIS

Presented to the Faculty

of the University of Alaska Fairbanks

in partial Fulfillment of the Requirements

for the Degree of

DOCTOR OF PHILOSOPHY

By

Hua Zhu, B.S., M.S.

Fairbanks, Alaska

May 2000

SMALL SPATIAL AND FAST TEMPORAL IONOSPHERE-MAGNETOSPHERE COUPLING PROCESSES

By

Hua Zhu

RECOMMENDED:

Advisory Committee Chair

Department Head

APPROVED:

Dean, College of Science, Engineering and Mathematics

Dean of the Graduate School

2-23-00

Date

Abstract

I have developed a two-dimensional, three-fluid model (electrons, ions and neutrals) to simulate small-scale magnetosphere-ionosphere coupling processes. The code includes ionization and recombination processes, the Hall term in Ohm's law, and various heat sources in the energy equations. The electro-dynamic response and the evolution of the collision frequencies are treated self-consistently in a height resolved ionosphere. The model allows for the propagation of Alfvén waves. The simulation is particularly suited for fast temporal variations and small spatial scale ionospheric structures associated with filamentary aurora and ionospheric heating experiments (e.g. HAARP).

I have investigated the evolution of field-aligned currents in the magnetosphere-ionosphere system and found several notable effects: ion heating due to plasma-neutral friction, electron heating resulting from energetic particle precipitation and ohmic dissipation by strong field-aligned currents. The simulation of plasma heating in the ionosphere is motivated by a specific auroral event that was simultaneously observed with optical and radar instruments. The results indicate that a consistent explanation of this event requires ohmic heating of electrons in a strong field-aligned electric current layer. They suggest strongly that the observed sequence of events can be explained only if spatial structure is present in the ionosphere so that it requires at least a two-dimensional model. Electron heating in

strong field-aligned currents also provides a mechanism to deposit energy in the F-region of ionosphere and thus can explain the formation of tall auroral arcs.

The simulation of the formation of field-aligned currents shows a strong plasma density depletion in the region of downward field-aligned current layer. The depletion is due to the divergent flow of the plasma. Similarly, the plasma density increases in the region of upward field-aligned current because of the convergent plasma motion. A modification of the ionospheric conditions by localized particle precipitation has an interesting effect. At the edge of the precipitation region, a new field-aligned current filament is formed. Finally, the simulation code is not limited by steady state assumptions commonly used for the Hall and Pedersen conductivities.

Contents

List of Figures vii

Acknowledgments xii

1 Introduction **1**

1.1 Ionosphere-magnetosphere coupling 3

1.2 Plasma in the ionosphere 4

1.3 Small scale ionospheric dynamics 6

1.4 Outline of the thesis 8

2 Numerical Model **13**

2.1 Basic equations 15

2.2 Boundary conditions 20

3 Ionospheric Heating **21**

3.1 Equilibrium and initial perturbation 22

3.2 Simulation results: Ion and electron heating in the ionosphere 25

3.2.1 Alfvén wave propagation and reflection 27

3.2.2 Ion heating by friction between ions and neutrals 29

3.2.3 Electron heating by particle precipitation 31

3.2.4 Electron heating by ohmic dissipation 33

3.2.5 Sources and losses for the electron temperature 39
3.3 Comparison with radar observation 41
3.4 Summary and discussion 47

4 Field-Aligned Current **50**
4.1 Equilibrium and initial perturbation 53
4.1.1 Boundary conditions 55
4.2 Results 55
4.2.1 Alfvén wave propagation and reflection in the ionosphere and the current layer formation 55
4.2.2 Density depletion 58
4.2.3 Widening of the downward field-aligned current 64
4.2.4 Finite field-aligned current filament 67
4.3 Summary and discussion 72

5 Tall Auroral Red Ray **76**
5.1 Outline of the simulation 77
5.2 Heating and energy balance 79
5.3 Summary and discussion 86

6 Ionospheric Conductivies **88**
6.1 The electric field in the ionosphere 89
6.2 Ionospheric conductivities 90
6.3 Height integrated conductivities 96
6.4 Summary and discussion 108

7 Conclusion **111**

7.1 The two-dimensional three-fluid ionosphere-magnetosphere coupling model . 112
7.2 Main results 113
7.2.1 Ionospheric heating 114
7.2.2 The effects of the field-aligned current in the ionosphere 115
7.2.3 Ionospheric conductivities 116
7.3 Future work 117
7.4 Conclusion 118

Bibliography **120**

List of Figures

1.1 Schematic representation of the magnetosphere 2

1.2 A sketch of thin auroral arc associated with the field-aligned current 7

3.1 Altitude profiles for neutral as well as plasma (ion and electron) density and temperature 23

3.2 Initial perturbations 24

3.3 Contour plots of plasma velocity, magnetic field, and the field-aligned current density 26

3.4 A sketch to illustrate the velocity and magnetic field perturbations for the incoming Alfvén wave and shortly after the reflection 28

3.5 Altitude versus time plots of the ion temperature for the solar-max and the solar-min conditions 30

3.6 Altitude profile of the ionization rate 32

3.7 Electron temperature evolution and number density for the ionization shown in figure 3.6 34

3.8 Field-aligned current without particle precipitation 36

3.9 Parallel resistivity in the upward current layer 37

3.10 Electron temperature evolution for the solar-min case in the upward current layer 38

3.11 Plot of source and loss terms for the electron temperature 40
3.12 Radar observation of small scale processes related to the discrete auroral arcs 42
3.13 Profile of electron density, ion temperature, and electron temperature . . . 43
3.14 Profile of electron density, ion temperature, and electron temperature . . . 46

4.1 Large scale FAC patterns in the high latitude ionosphere 52
4.2 A sketch of the Alfvén wave propagation and field-aligned current formation 54
4.3 Simulation results of the time evolution of the Alfvén wave propagation and reflection in the ionosphere and the field-aligned current layer formation . . 57
4.4 Contour plot of the Alfvén wave propagation and the field-aligned layer formation 59
4.5 A sketch of the electron and ion motion in the downward field-aligned current layer 60
4.6 Simulation results of the FAC, the ion and electron motions related to the FAC layers in the ionosphere, density hole, and Pedersen as well as Hall conductivities 62
4.7 The plots of time evolution of the electron number density at the different locations 63
4.8 The change of plasma number density, the Pedersen and Hall conductivities from time 1.0 s to time 8.2 s at the altitude of $z = 120$ km 65
4.9 The ionospheric current at times $t = 1.0$ s and $t = 8.2$ s , and the downward field-aligned current layer widenning 66
4.10 Ionization profile 68
4.11 Finite FAC filament at the sharp edge of the particle precipitation boundary and the ion as well as electron motion 69

4.12 Contour plots of the plasma number density, Pedersen and Hall conductivities in the simulation of a FAC with particle precipitation in the vicinity of the upward FAC layer 71

4.13 Magnetic field perturbation at the altitude of 250 km and 132 km at the time 6.15 s in the simulation of a FAC with particle precipitation in the vicinity of the upward field-aligned current layer 73

5.1 Current density and electron temperature profiles 78

5.2 Electron temperature profiles inside the field-aligned current layers 81

5.3 Source and loss term contributions to the electron energy 82

5.4 Redline emision in Rayleighs assuming a steady emission conditions and a column of 10 km for different cases. 84

5.5 Contour plots of auroral red line emission 85

6.1 Contribution from different terms to the electric field at the location of large electron pressure gradient 91

6.2 Typical conductivity values for the mid-latitude ionosphere 94

6.3 Ionospheric conductivity profiles from one simulation result 95

6.4 Contour plots of current densities from the simulation compared with the Pedersen and Hall current calculated from ionospheric conductivities 99

6.5 Electric field and conductivity profiles in the field-aligned current layer simulation 101

6.6 Comparison between the height integrated ionospheric current from the simulation and the current calculated from the electric field at 116 km and the height integrated ionospheric conductivities 103

6.7 Comparison between the height integrated ionospheric current from the simulation results and the current calculated from the height integrated ionospheric conductivities using the electric field at 250 km 104

6.8 Electric field and conductivity profiles in the field-aligned current layer simulation with particle precipitation in the vicinity of the upward field-aligned current layer 106

6.9 Height integrated ionospheric current for the field-aligned current simulation with particle precipitation added in the vicinity area of the upward field-aligned current layers 109

Acknowledgments

I would like to express my heartfelt thanks to my dear wife Yanxia Chang. Without her deep love, considerate care and great patience, it would have been impossible for me to finish this hard work. My gratitude also extends to my parents Mr. Fubin Zhu and Ms. Weiying Guan, my lovely son Changhai Zhu, my sister Ms. Ping Zhu, and my brother Mr. Hong Zhu. Their love, expectation and support have encouraged me to finish this thesis with my greatest effort.

It is entirely inadequate to show my sincere appreciation to Professor A. Otto, the chairman of my graduate advisory committee, by simply saying an ordinary "thank you". I am very grateful that I have had him as my thesis advisor. Not only has his continuous guidance, advice, encouragement, and help made the completion of this thesis possible, his broad knowledge and deep-thinking in physics opened my mind, and he has greatly aroused my confidence in conducting scientific research. I am also very thankful to the other members of my advisory committee, Professors J. V. Olson, R. W. Smith, H. Nielsen, D. Lummerzheim, and J. R. Kan, for their helpful discussions, suggestions and words of encouragement in preparing this thesis. Particularly, I would like to thank Dr. D. Lummerzheim for his help in parameterization of the chemical processes in the ionosphere.

It is also a great pleasure to thank Professor M.H. Rees for his interests and helpful

comments on my work.

I would like to give special thanks to Dr. M. J. Heavner, with whom I have shared the same office for several years. We came to the Geophysical Institute at about the same time in the year of 1993 and both finished our Ph.D. work in 1999. He is a nice friend and always willing to help. I benefited a lot from him. I am also thankful to L. M. Peticolas, F. Hall, and other fellow students for their generous help and encouragement.

This research work was financially supported by the U.S. Air Force grant F 19628-96-C-0011.

Chapter 1

Introduction

Of major importance for the physics of the Earth's magnetosphere is the coupling between the magnetosphere and the ionosphere. Magnetospheric dynamics is determined by the physical processes at the boundaries of the magnetosphere. The outer boundary of the system is the magnetopause, i.e., the interface between the magnetosphere and the shocked solar wind plasma. The other, inner boundary of the magnetosphere is the ionosphere. Figure 1.1 shows a sketch of the earth's magnetosphere-ionosphere system (Kelley [1989]).

Most fundamental plasma processes in the magnetospheric system involve plasma convection and plasma waves. These are causing magnetic field-aligned electric currents which propagate into the inner magnetosphere and down into the ionosphere. In the ionosphere these currents must close perpendicular to the magnetic field through horizontal currents. Thus the the ionosphere provides the boundary at which magnetospheric currents must close and the properties of the ionosphere determine how these currents close. It is important to note that these currents are mostly carried by Alfvén waves. Therefore a model for the formation and evolution of field-aligned currents requires the plasma equations that allow for Alfvén wave propagation.

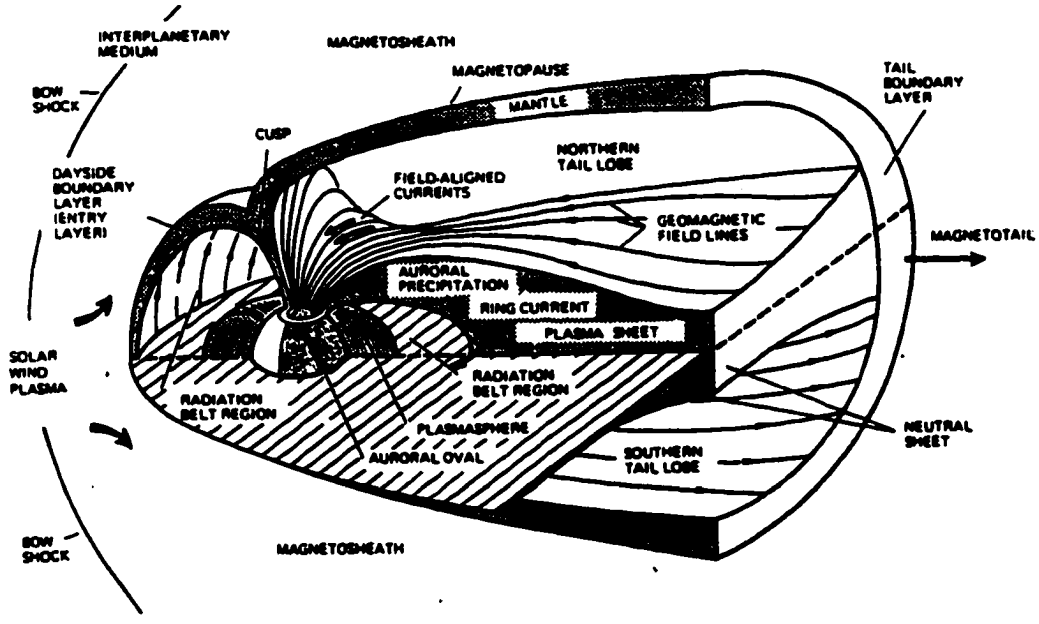

Figure 1.1: Schematic representation of the magnetosphere. (Kelley [1989])

1.1 Ionosphere-magnetosphere coupling

The problem of the coupling between the earth's magnetosphere and the ionosphere has been studied by many researchers for a long time. There are a variety of spatial and temporal scales involved in the ionosphere-magnetosphere system, ranging from the small scale discrete aurora arcs (less than 1 km) to the global scale plasma convection pattern (several thousand kilometers). Various models have been developed to study the ionosphere-magnetosphere coupling processes with different scale sizes (e.g. Wolf *et al.* [1982]; Harel *et al.* [1981]; Kan [1993]; Roble and Rees [1977]; Fuller-Rowell and Rees [1980]; Sojka [1989]; Schunk [1988]; Roble *et al.* [1987]; Maurits and Watkins [1996]).

Different methods have been used in the study of the plasma dynamics due to the differences of the plasma properties in the various regions of the ionosphere-magnetosphere system. In most regions of the magnetosphere, the plasma is collisionless. On sufficiently large scales ions and electrons are frozen into the magnetic field (i.e. $\mathbf{E} + \mathbf{v} \times \mathbf{B} = 0$), so that the ideal MHD equations are widely used to study the plasma dynamics in the magnetosphere. In steady state, and assuming that $E_{||} = 0$, the magnetic field lines are on equal potential such that one can map the electric field in the ionosphere to the magnetosphere. In the ionosphere, collisions (Coulomb, electron-neutral, ion-neutral) lead to a finite conductivity. Thus the ionosphere represents a partially conducting boundary to the magnetosphere. Several large scale steady state ionosphere-magnetosphere coupling models were developed during the 70s (e.g. Axford [1969]; Vasyliunas [1970]; and Vasyliunas [1972]). These models address the large scale magnetospheric plasma convection motion on time scales of the order of hours.

There are also various global models (e.g. the Rice convection model, i.e. Wolf *et al.* [1982] and Harel *et al.* [1981] MHD models) to simulate the large scale magnetospheric dynamics. However, in these global scale models the ionosphere is usually simulated as

a partially conducting boundary, and for years it seemed that people only treated the ionosphere as a passive recipient of the magnetospheric dynamics. Thus these models do not resolve the explicit ionospheric dynamics.

1.2 Plasma in the ionosphere

The basic physical principles which determine the properties of the ionosphere are well understood (Schunk [1988]). Different from the magnetosphere, the plasma in the ionosphere (at altitudes below 150 km) is characterized by high collision frequencies between electrons, ions and neutral particles. Above 150 km, the ion-neutral and electron-neutral collision frequencies are much smaller than the ion and electron gyro-frequencies respectively. Thus the drift motion of the ions and electrons associated with the horizontal electric field does not give any considerable electric current. But in the lower E-region (below 120 km), the ion-neutral collision frequency can be as high as about 10^5 s^{-1}, which is much higher than the ion's gyro-frequency (about 300 s^{-1} in a 0.5 gauss geomagnetic field) such that the ion mean free path is much shorter than the gyro-radius. So the ions in the lower E-region are no longer drifting in the $\mathbf{E} \times \mathbf{B}$ direction. The electron motion in these lower altitudes, however, is still subject to the $\mathbf{E} \times \mathbf{B}$ drift. Although the electron-neutral collision frequency can reach a value above 10^5 s^{-1}, it is still much smaller than the electron's gyro-frequency which is about 9×10^6 s^{-1} (assuming a 0.5 gauss geomagnetic field). This difference between the ion and electron drift motions causes the horizontal ionospheric currents. The component of the ion motion in the direction parallel to the electric field gives the so called ionospheric Pedersen current which closes the field-aligned current, the electron's $\mathbf{E} \times \mathbf{B}$ drift contributes to the ionospheric Hall current. As the altitude increases (from 120 km to 150 km), due to the decreasing of the ion-neurtal collision frequencies, the ion velocity vector rotate towards the $\mathbf{E} \times \mathbf{B}$ direction.

From the concept of the Pedersen and Hall current, the ionospheric current can be expressed by the ionospheric conductivities as

$$\mathbf{j} = \sigma_0 \mathbf{E}_{||} + \sigma_P \mathbf{E}_{\perp} + \sigma_H \hat{\mathbf{b}} \times \mathbf{E} \tag{1.1}$$

where σ_0, σ_P, and σ_H are parallel, Pedersen and Hall conductivities, respectively, $\hat{\mathbf{b}}$ is the unit vector of the magnetic field, $\mathbf{E}_{||}$ and $\mathbf{E}_{\perp}$ are parallel and perpendicular components (with respect to the magnetic field) of the electric field, respectively. The ionospheric conductivities are determined by the ion-neutral and electron-neutral collision frequencies.

The conductivities also require an approximate steady state for the ion flow because the ion inertia term is ignored in the derivation. This is reasonable for many applications because the time scale for the ion-neutral collision in the lower ionosphere (below 150 km) can be less than 10^{-4} second which is much shorter than the time scale of most ionospheric structures. But for the extreme case such as very fast moving or evolving thin auroral arcs, these ionospheric conductivities might not be applicable. For very fast processes the ion inertia term becomes important compared to ion-neutral friction such that neglect of ion inertia, as assumed for Hall and Pedersen conductivity, is not justified. In addition to the high ion-neutral collision rate that causes the Pedersen current, there are also ionization (associated with photo ionization or particle precipitation) and recombination processes in the ionosphere that are very important to the ionospheric plasma dynamics.

Similar to global magnetospheric simulations various models have been developed to simulate the large scale convection in the ionosphere (e.g. Roble and Rees [1977]; Fuller-Rowell and Rees [1980]; Sojka [1989]; Schunk [1988]; Roble *et al.* [1987]; Maurits and Watkins [1996]). In these models the convection is prescribed at the topside ionosphere in terms of a perpendicular velocity or in terms of the corresponding convective electric field. This field is not self-consistent but is determined either from large scale radar and *insitu* satellite observations (combined with satellite images) or is taken from convection models

which are parameterized by solar wind conditions and the interplanetary magnetic field (IMF) orientation.

While these models can be very useful to predict large scale ionospheric convection, they are not suitable to model fast temporal scales or small spatial structures. In order to model the larger scale ionosphere, global convection models must be able to use a relatively long time step for the simulation. To facilitate this they neglect the inertia term in the momentum equations and determine the convection velocity through the plasma-neutral friction in this equation (equation (2.3)). However in doing so they eliminate the usual fluid plasma waves (Alfvén, slow, and fast waves) and the dynamics related to such waves. They are therefore not capable of modelling the physics of field-aligned current formation and evolution associated with these waves.

1.3 Small scale ionospheric dynamics

It has been established for many years that discrete auroral arcs are often very narrow (100 m to 1 km) (e.g. Maggs and Davis [1968]; Borovsky [1993]). These auroral arcs move often with considerable velocity (several kilometers per second) and faster than the typical ionospheric plasma convection. The thin curtains of aurora are accompanied by thin layers (of the order of 1 km) of field-aligned currents. Figure 1.2 shows a sketch of a thin auroral arc associated with the field-aligned current layer. This type of aurora is typical for high magnetic latitudes and in particular for periods of enhanced geomagnetic activity. During periods of southward IMF magnetic reconnection at the day-side ionosphere increases the amount of open geomagnetic flux, i.e., magnetospheric magnetic field which is connected to the solar wind (Dungey [1961]). As a consequence the Earth's magnetic field undergoes a major reconfiguration which is associated with strongly enhanced field-aligned currents (e.g. Akasofu [1984]; Vasyliunas [1984] and Iijima [1984]). In the high latitude

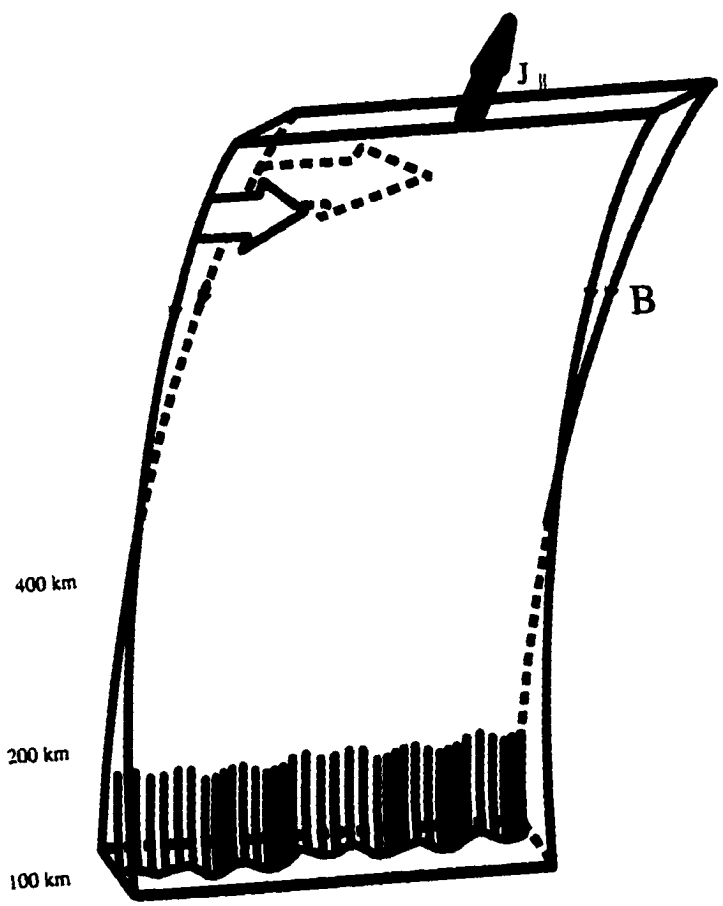

Figure 1.2: A sketch of thin auroral arc associated with the field-aligned current.

region the corresponding process is the auroral substorm (Akasofu [1964]). This period of time is characterized by strongly enhanced magnetic perturbations, particle precipitation, ionospheric currents, and field-aligned currents. These currents are highly filamentary and strongly time dependent.

Thus a proper understanding of the magnetosphere-ionosphere coupling requires to resolve the physics associated with field-aligned current formation and evolution on the relevant spatial and temporal scales. It has been the goal of this work to provide the first model (chapter 2) capable of doing this. Important properties which are obtained by this model are electron heating, ion heating and energy deposition in the neutral atmosphere, ionospheric density irregularities associated with field-aligned currents, electric conductivity of the ionosphere, and the evolution of field-aligned currents in the presence of electron precipitation. The results from our simulation show some very interesting aspects that indicate the ionosphere is not just a passive recipient of the magnetospheric dynamics, it can play a important role in the ionosphere-magnetosphere coupling system.

1.4 Outline of the thesis

The two-dimensional, three-fluid (neutral, ion and electron) model (chapter 2) I have developed for this thesis is the first model that can quantitatively simulate the dynamics of the fast temporal and small spatial scale ionospheric structures particularly related to the discrete aurora. By using this model, I have studied the ionosphere-magnetosphere coupling processes with the emphasis on the dynamics of the small scale ionosphere structures and achieved several interesting and relevant results. These results show that the small scale ionospheric structure plays an important role in the coupled ionosphere-magnetosphere system.

The results of chapters 2, 3, 4, and 5 present largely the contents of publications that

are submitted or about to be submitted for publication in the Journal of Geophysical Research (chapters 2, 3, and 4, e.g., Zhu *et al.* [1999]; and Zhu *et al.* [2000]) and Geophysical Research Letters (chapter 5, Otto *et al.* [1999]). I had the lead role in contributing to these publications (developing the simulation model, designing the model runs, stating the scientific objective and analizing and interpreting the results and associated physics). In the papers Zhu *et al.* [1999] and Zhu *et al.* [2000], I developed the original idea, designed the model runs, and analized the results. The role of coauthors included input for the parameterization of transport parameters, provision of optical and radar observations to be compared to my results and helpful discussions on various details of the simulation model. For the tall ray paper (Otto *et al.* [1999]), Dr. Rees first raised the topic of research on the tall auroral red-ray. Based on my simulation results of electron heating by field-aligned current, Otto *et al.* [1999] have suggested the mechanism for the tall auroral red-ray.

The detailed description of the two dimensional three-fluid model is given in chapter 2. The model was originally developed by Birk and Otto [1996]. I modified the original model and improved it to a quantitative, realistic ionospheric dynamic model. The new model includes a full set of dynamic equations for the neutrals, ions and electrons. The height profile for the neutral number density and temperature is set at the beginning of the simulation according to the solar conditions which provides a realistic quantitative neutral ionospheric environment. This neutral ionospheric environment makes it possible to calculate the plasma-neutral collision frequencies (including ion-neutral and electron collisions) and thus to compute the ionospheric conductivities self-consistently during the simulation time. The code also includes the particle precipitation as well as recombination processes that are important in studying the ionospheric dynamics. The inertia term in the plasma momentum equation allows the Alfvén wave to propagate in the ionosphere-magnetosphere system which enables us to simulate the evolution and formation of the

field-aligned electric current. There are various source and loss terms in the plasma energy equations so that we can compute the ion and electron heating and temperatures by different mechanisms in the ionosphere.

Motivated by optical and radar (EISCAT) observations of small scale discrete aurora, chapter 3 shows the first results of the ionospheric heating using this code. The simulation shows that Alfvén waves propagate along the magnetic field lines from the magnetosphere down to the ionosphere and set ions in the ionosphere into motion. Due to the high ion-neutral collision in the ionosphere, ions in the ionosphere are strongly heated. The altitude range of the ion heating differs depending on the ionospheric neutral condition (which is related to the solar conditions). Both the energetic particle precipitation and the ohmic dissipation inside the field-aligned current are the sources for heating the electrons in the ionosphere. The electron heating by the particle precipitation is localized at certain altitude regions depending on the characteristic parameters (spectrum) associated with the precipitating particles, while the electron heating by the ohmic dissipation extends along the entire field-aligned current layer. The results of the simulation from the spatial structure used in this chapter show a good agreement with the radar (EISCAT) observations in both the ion and electron heating and the plasma number density variation. The heating effects discussed in chapter 3 depend on the local plasma and neutral conditions and can in principle be determined by a one-dimensional model provided that ion velocities and field-aligned current profiles are known.

In chapter 4, I investigate the formation of the field-aligned current layers in the ionosphere-magnetosphere system and the effects that are caused by the field-aligned current in the ionosphere. Several interesting results are achieved with clear physical mechanisms. The up and downward field-aligned current layers (with a width of about 2 km) are formed when the two sheared magnetic perturbations in the magnetosphere propagate with the Alfvén

wave speed along the magnetic field lines into the ionosphere. Due to the high ion-neutral collision frequencies, the field-aligned currents are closed by the so called Pedersen current in the lower E-region of the ionosphere. The field-aligned current is carried mostly by the electrons, while the contribution to the closing Pedersen current is largely from ions. As a result of the different flow patterns of the ions and electrons in the up and downward field-aligned current layer, irregularities are found in the plasma number density and the ionospheric conductivities (Pedersen and Hall conductivities) at the altitude of the closing Pedersen current. The convergent flow of ions and electrons at the base of the upward field-aligned current layer causes the increase of the plasma number density as well as the ionospheric conductivities, while the divergent flow of the plasma at the base of the downward field-aligned current layer, on the other hand, generates a plasma density hole and thus decreases both the Pedersen and Hall conductivities. The downward field-aligned current layer widens with time because of the evolution of the plasma density depletion. Interesting finite field-aligned current filaments are found at the edge of the sharp particle precipitation boundaries.

In chapter 5, I suggest a mechanism that causes the tall auroral red-ray emission which is often seen in the solar maximum years. During the solar maximum, the neutral atmosphere extends to higher altitudes and increases the density of neutral oxygen atoms. The hot electrons in the upward field-aligned current layers can provide enough energy for the $O(^1D)$ excitation and generate the observed tall auroral red rays.

The ionospheric conductivities and the height integrated ionospheric current are discussed in chapter 6. Since the large Pedersen and Hall conductivities are very localized in the lower ionosphere (E-region), the ionospheric currents (Pedersen and Hall currents) are meaningful only in the lower ionosphere (below 150 km). The Pedersen and Hall conductivities derived in the usual way have ignored the effect of the plasma pressure gradient and

the inertia terms in the plasma momentum equations. I found that in the region where the plasma pressure gradient is large (such as the case discussed in chapter 4), there is a significant contribution from the electron pressure gradient term to the Hall current. When the discrete auroral arcs move fast enough such that the contribution from the inertia term is not negligible, the use of the ionospheric conductivities derived in the usual way is also highly questionable.

A summary of the simulation results and suggestions for future works are given in the chapter 7.

Chapter 2

Numerical Model

The motivation for the present model is the need to better understand the electromagnetic effects of small scale ionosphere-magnetosphere coupling, with emphasis on the ionospheric physics. There are ionospheric models which focus on the ionospheric vertical transport and therefore are one-dimensional (i.e., they treat the altitude dependence of the relevant transport property) (e.g. Nagy and Banks [1970]; Mantas [1974]; Strickland *et al.* [1976]; Link [1992]; Lummerzheim and Lilensten [1994]; Lanchester *et al.* [1997]; Lanchester *et al.* [1998]). Others are large scale ionospheric convection models (e.g. Roble and Rees [1977]; Sojka [1989];Schunk [1988]; Raeder *et al.* [1996]; Raeder *et al.* [1998]; Slinker *et al.* [1999]; Lyons [1998]; Roble *et al.* [1987]; Maurits and Watkins [1996]) that determine convection by a steady-state ion momentum equation. However, neglecting the ion inertial term leaves out the physics of Alfvén wave propagation. The assumption of a steady state implies $\partial B/\partial t = 0$ and a potential electric field. While this assumption is reasonable for large length scale, it is violated on small length scale. My model does not have this limitation. Consequently it is able to model, for instance, the formation of a field-aligned current layer through the propagation of Alfvén wave packets into the ionosphere. Such currents

and Alfvén waves may be of central importance for filamentary aurora (e.g., Lanchester and Rees [1987]; Seyler [1988]; Seyler [1990]; Otto and Birk [1992]; Otto and Birk [1993]; Haerendel [1994]; Lanchester *et al.* [1997]; Stasiewicz *et al.* [1998]).

The present work introduces results of an improved two-dimensional, three-fluid code. The original code (Birk and Otto [1996]; Birk and Otto [1997]) incorporated basic plasma transport coefficients such as ionization, plasma-neutral friction, resistivity, etc., but most of these parameters were kept constant in time. Values of these transport parameters were assumed such that the model yielded a reasonable ionospheric response to magnetospheric input such as the reflection of Alfvén waves, but the result of the simulation was unable to describe properly the corresponding ionospheric modifications, similar to the model by Dreher [1997]. The improvements which are detailed in this chapter address a realistic altitude profile of ionization rates, electron and ion cooling rates, and the modifications in the plasma parameters (density, electron and ion temperatures) are fed back into the transport parameters. Thus, the model includes the nonlinear 2-D ionospheric dynamics. In the following chapters, I will present a number of examples of such nonlinear effects. Electron inertia is not included in the model for the present work because the length scale of the electron inertia term is about 20 m, much smaller than the typical horizontal length scale in the simulation (1 km). The electron inertia term is much smaller than other terms in Ohm's law.

Small scale filamentary structure is very frequent in the auroral ionosphere (e.g., Borovsky [1993]; Lanchester *et al.* [1994]; Lanchester *et al.* [1997]). This is a strong indication for the importance of time dependent processes which require ion inertia. In order to address the physics adequately it is also necessary to incorporate realistic ionospheric transport. However, there are always limitations to the degree that this is possible. For instance, to avoid including a complex electron transport code, the ionization rates in my model are

parameterized by a characteristic energy and energy flux and then computed for an equilibrium neutral atmosphere with a prescribed temperature distribution. For the ionization rates (and electron cooling rates) it is important to identify the neutral species. These are obtained from a height profile of an average neutral molecular mass, since the neutrals are modeled as one fluid. The code can accommodate an altitude varying ion mass. However, the present results are obtained for a fixed ion mass, representative of O^+. A variable ion composition would require expansion of the three-fluid to a multi-fluid code. Therefore, effects that are specific to the presence and dynamics of more than one distinct ion species are not addressed. Extensions to multiple ion species and anisotropic pressures can be incorporated as the physical problems require such effects.

2.1 Basic equations

In this study, I use a full set of three fluid equations (electrons, ions and neutrals). This model is based on the three-dimensional plasma-neutral gas-fluid model developed by Birk and Otto [1996]. The original model is a two-fluid model which includes equations of fluid neutral and plasma dynamics. Since the plasma equations only solve total plasma dynamics (i.e. $p = p_e + p_i$, $T = T_e + T_i$, $\rho = \rho_e + \rho_i \approx \rho_i$, and $\mathbf{v} \approx \mathbf{v}_i$), the old model cannot distinguish ion and electron motion seperately and thus is not suitable to quantitatively simulate the ionospheric dynamics, especially that associated with the ionospheric currents. Although collision frequencies between plasma and neutral gas are included, they are prescribed and not computed self-consistently with time during the simulation. To do the research for this thesis, I have added various new terms that are necessary and important for the small scale ionosphere-magnetosphere coupling processes associated with thin auroral arcs and field-aligned current. These new terms include ionization and recombination processes, electron pressure gradient and Hall terms in Ohm's law, electron velocity to distinguish the electron

and ion motions (which is very important for field-aligned current simulation), temperature contact terms between electrons, ions, and neutrals and heat conduction term in energy equations. An equation of electron temperature is added into the model to separate the different heating mechanisms for electrons and ions. Collision frequencies between electrons, ions, and neutrals are calculated self-consistently during the simulation which makes sure that the change of ionospheric conductivity is correctly computed. To quantitatively simulate the real ionosphere-magnetosphere coupling processes, height resolved neutral density (includes n_O, n_{O2}, and n_{N2}) and temperature profiles are prescribed at the beginning of the simulation depending on solar condition.

The following are normalized equations used in this research, where the terms in red color are my additions to the old model (Birk and Otto [1996]):

$$\frac{\partial \rho}{\partial t} = -\nabla \cdot \rho \mathbf{v} + \iota\rho - \beta\rho^2 \tag{2.1}$$

$$\frac{\partial \rho_n}{\partial t} = -\nabla \cdot \rho_n \mathbf{v}_n - \iota\rho + \beta\rho^2 \tag{2.2}$$

$$\begin{aligned} \frac{\partial \rho \mathbf{v}}{\partial t} &= -\nabla \cdot (\rho \mathbf{v}\mathbf{v}) - \frac{1}{2}\nabla p + \rho \mathbf{g} \\ &\quad + (\nabla \times \mathbf{B}) \times \mathbf{B} + \rho \mathbf{v}(\iota - \beta\rho) \\ &\quad - \rho\nu_{in}(\mathbf{v} - \mathbf{v}_n) \end{aligned} \tag{2.3}$$

$$\begin{aligned} \frac{\partial \rho_n \mathbf{v}_n}{\partial t} &= -\nabla \cdot (\rho_n \mathbf{v}_n \mathbf{v}_n) - \frac{1}{2}\nabla p_n + \rho_n \mathbf{g} \\ &\quad - \rho \mathbf{v}_n(\iota - \beta\rho) - \rho\nu_{in}(\mathbf{v}_n - \mathbf{v}) \end{aligned} \tag{2.4}$$

$$\begin{aligned}\frac{\partial \mathbf{B}}{\partial t} &= \nabla \times \left(\frac{1}{ne}\nabla p_e\right) + \nabla \times (\mathbf{v} \times \mathbf{B}) \\ &\quad -\nabla \times \left(\frac{1}{ne}(\nabla \times \mathbf{B}) \times \mathbf{B}\right) \\ &\quad -\nabla \times (\eta \nabla \times \mathbf{B}) \end{aligned} \tag{2.5}$$

$$\begin{aligned}\frac{\partial p}{\partial t} &= -\mathbf{v} \cdot \nabla p - \gamma p \nabla \cdot \mathbf{v} + (\iota - \beta\rho)T_n \\ &\quad +(\gamma - 1)\Big(2\eta(\nabla \times \mathbf{B})^2 \\ &\quad +\iota e_c - 3\frac{\nu_{in}\rho}{m_i + m_n}(T_i - T_n) \\ &\quad +(\frac{m_n \nu_{in}\rho}{m_i + m_n} + \iota m_i)(v - v_n)^2\Big) \\ &\quad +3\nu_{eff}\rho(T_n - T_e) + \frac{\partial}{\partial z}(\lambda_e \frac{\partial T_e}{\partial z}) \end{aligned} \tag{2.6}$$

$$\begin{aligned}\frac{\partial T_e^\kappa}{\partial t} &= -\nabla \cdot (T_e^\kappa \mathbf{v}_e) \\ &\quad +T_e^{\kappa-1}\Big(3\nu_{ei}(T_i - T_e) \\ &\quad +3\nu_{eff}(T_n - T_e) + \frac{2\eta}{n}(\nabla \times \mathbf{B})^2 \\ &\quad +\frac{\iota e_c}{n} - \frac{\iota T_e}{(\gamma - 1)n} \\ &\quad +\frac{1}{n}\frac{\partial}{\partial z}(\lambda_e \frac{\partial T_e}{\partial z})\Big) \end{aligned} \tag{2.7}$$

$$\begin{aligned}\frac{\partial p_n}{\partial t} &= -\mathbf{v_n} \cdot \nabla p_n - \gamma_n p_n \nabla \cdot \mathbf{v_n} - (\iota - \beta\rho)kT_n \\ &\quad +(\gamma_n - 1)\Big(3\frac{\nu_{ni}\rho_n}{m_i + m_n}(T_i - T_n) \\ &\quad -\iota\rho T_n + \frac{m_i \rho_n \nu_{in}}{m_i + m_n}(v_n - v)^2\Big) \\ &\quad +3\nu_{eff}\rho(T_e - T_n) \end{aligned} \tag{2.8}$$

here, ρ and ρ_n are the total plasma and neutral mass density; m_i and m_n are the ion and neutral particle mass; T_e, T_i and T_n are the electron, ion and neutral temperatures; p, p_e and p_n are the total plasma pressure, electron pressure and neutral pressure; n is the plasma number density; $\mathbf{v}$, $\mathbf{v}_e$, and $\mathbf{v}_n$ are plasma, electron, and neutral velocities; $\mathbf{B}$ is the magnetic induction vector; $\mathbf{g}$ is the gravitational acceleration; ι is the ionization rate; ν_{in} is the ion-neutral, ν_{ei} the Coulomb, and ν_{eff} the effective collision frequency between electrons and neutrals; η is the resistivity; γ and γ_n are the ratios of specific heats for the plasma and neutrals; e_c is the average energy that goes into electron heating for each ionization process (a typical value is $2eV$); λ_e is the electron heat conduction coefficient; and $\kappa = \frac{1}{\gamma-1}$. Energy conservation requires $\gamma_n = \gamma = 5/3$.

The ionization rate ι, the recombination rate β, and the electron heating rate associated with ionization e_c are parameterized by using input from an ionospheric transport computation (Lummerzheim [1992]). The electron heat conduction coefficient λ_e and the effective electron-neutral collision frequency ν_{eff} are from the NCAR Thermosphere-Ionosphere-Mesosphere-Electrodynamics General Circulation Model (TIME-GCM) (Roble [1996]). The resistivity in the simulation is given by:

$$\eta = \eta_{ei} + \eta_{en} + \eta_{in} \tag{2.9}$$

with

$$\eta_{ei} = \lambda \nu_{ei} \tau_A$$

$$\eta_{en} = \lambda \nu_{en} \tau_A$$

$$\eta_{in} = \lambda \nu_{in} \tau_A$$

where ν_{ei}, ν_{en}, ν_{in} are the electron-ion, electron-neutral, and ion-neutral collision frequencies; $\tau_A = l_0/v_A$ is Alfvén time; and $\lambda = (\frac{c}{\omega_{pe} l_0})^2$ is a normalization coefficient. The parameterization of collision frequencies ν_{ei}, ν_{en} and ν_{in} is given by Schunk [1983].

In the computation, I assume singly charged ions, charge neutrality, and the following definitions:

$$
\begin{aligned}
n &= n_e = n_i \\
\rho &= n(m_e + m_i) \\
p &= p_e + p_i \\
\rho \mathbf{v} &= \rho_e \mathbf{v}_e + \rho_i \mathbf{v}_i
\end{aligned}
$$

The results are presented in physical units. In the simulation, all the quantities in equations (2.1) through (2.8) are normalized to characteristic values of the system, i.e., the horizontal length scale to the typical length $l_0 = 1.0$ km, the vertical length scale to $l_{z0} = 500$ km, plasma and neutral number density n and n_n to $n_0 = 50000$ cm^{-3}, mass m_e, m_i and m_n to the oxygen mass $m_0 = m_{O+}$, mass density ρ and ρ_n to $\rho_0 = n_0 m_0$, magnetic field B to $B_0 = 0.5$ gauss, vertical velocity v_z, v_{ez}, and v_{nz} to the Alfvén velocity $v_A = B_0(\mu_0\rho_0)^{-1/2}$ (1220 km s^{-1}), horizontal velocity $\mathbf{v}_x$ and $\mathbf{v}_y$ to $l_0/l_{z0}v_A$ (2.44 km s^{-1}), pressure p, p_e, and p_n to $P_0 = B_0^2/(2\mu_0)$, T_e and T_n to $T_0 = P_0/(n_0 k)$, where k is the Boltzmann constant, and time t to characteristic Alfvén transit time $\tau_A = l_{z0}/v_a$.

I use cartesian coordinates in the simulation with x and y (invariant) perpendicular to the magnetic field. z is along the unperturbed magnetic field, which in the northern hemisphere is in the negative B direction. The equations are solved with a modified Leapfrog scheme (Potter [1973]; Birn [1980]) of second-order accuracy in space and time. The grid points in the horizontal (x) direction are uniformly spaced. In the vertical direction, a nonuniform grid is used with the best resolution of 4 km at the bottom boundary of the simulation domain.

2.2 Boundary conditions

In the simulation, I use periodic boundary conditions in the x direction which allows waves to propagate freely through the system. At the lower boundary of the simulation box (z = 100 km), the densities ρ, ρ_n, pressures p, p_e, p_n, and temperatures T_e and T_n, are given by continuous boundary conditions, i.e. the boundary values of these quantities are computed by extrapolation. But, for the magnetic field $\mathbf{B}$, current $\mathbf{j}$, and plasma velocity $\mathbf{v}$, I determine the boundary values using Ohm's law.

After obtaining the boundary values for ρ and p, I compute the collision frequencies ν_{en}, ν_{in}, and ν_{ei} and the Pedersen and Hall conductivities. I extrapolate the electric field from the physical boundary to a mathematical boundary and use Pedersen and Hall conductivities to compute the current density from $\mathbf{j} = \sigma \cdot \mathbf{E}$ on this boundary. Similarly, the boundary value for the plasma velocity $\mathbf{v}$ is determined by

$$\mathbf{v}_i = \frac{e}{m_i}\left(\frac{\nu_{in}}{\omega_{ci}^2 + \nu_{in}^2}\mathbf{E}_\perp + \frac{\omega_{ci}}{\omega_{ci}^2 + \nu_{in}^2}\mathbf{E} \times \hat{\mathbf{b}}\right) \tag{2.10}$$

where ω_{ci} is the ion gyrofrequency, and $\hat{\mathbf{b}}$ is the unit vector of unperturbed magnetic field. Finally, the magnetic field $\mathbf{B}$ is determined from the relation $\mathbf{j} = \nabla \times \mathbf{B}$.

At the top boundary of the model system (z = 1100 km) I use free boundary conditions for most quantities, that is, I calculate the value at the boundary from its value inside the physical boundary of the system by extrapolation. This maintains the initial perturbation for the Alfvén waves and allows the transmission of the waves which are reflected in the lower ionosphere.

Chapter 3

Ionospheric Heating

The simulation results in this chapter are motivated by optical and radar (EISCAT) observations of small scale discrete aurora. These observations and results from transport simulations are presented by Lanchester *et al.* [1999] hereafter referred to as Lanchester99. The one-dimensional transport simulations in Lanchester99 treat the ion chemistry, electron transport, and variations of the precipitating flux more accurately than is possible in the two-dimensional approach. Thus this work complements my results on the electrodynamics and spatial structure. The event in Lanchester99 shows an unusual evolution of plasma number density, ion temperature, and electron temperature. The observations and a comparison of my model results with these are presented in section 3.3. Motivated by this, the simulation results in this chapter focus on the formation of field-aligned current (FAC) layers, the associated heating of ions by the plasma motion in the Alfvén waves, and electron heating by precipitation and in particular by ohmic dissipation in the FAC. Other aspects of the two-dimensional dynamics such as nonlinear effects for FAC's, electron densities, and conductivities will be the topic of the following chapters.

3.1 Equilibrium and initial perturbation

The simulation region extends from 100 km (lower E-region) to 1100 km altitude with the main magnetic field in the vertical direction. The neutral fluid is initially in hydrostatic equilibrium with a temperature T_n and density n_n chosen for solar-min and solar-max conditions from the MSIS model (Hedin [1991]) (see Figure 3.1). The neutral number density and temperature profiles are significantly different at high altitudes for solar-min and solar-max conditions. These differences yield ion heating at different altitudes. The neutral number density n_n in the simulation is the sum of three species, i.e. n_{N2}, n_O, and n_{O2}; all contribute to ionization and electron cooling.

I assume that the ions initially have the same temperature profile as the neutrals. The electron temperature equals the neutral only at the lower boundary of the system, but gradually increases (above 250 km) with altitude to a value of about 1300 K for solar-min conditions and 1750 K for the solar-max case at 600 km. To determine the initial plasma density profile, I assume a high altitude number density of 5×10^4 cm^{-3}. Using force equilibrium and the $T_e + T_i$ profile, I obtain the ion density profile. This profile is adjusted at lower altitudes to a typical density measured by the EISCAT radar during the event being analyzed. A small resulting force imbalance at low altitudes is negligible because the plasma is strongly collision dominated and corresponding effects occur on much longer time scales than considered here.

An initial perturbation of the plasma velocity and the horizontal magnetic field is applied at the top boundary with (Figure 3.2)

$$v_y = \frac{v_{y0}}{2}\Big(1 + \tanh\big(0.015(z-800)\big)\Big)\tanh\big(2.0(x+6.0)\big) \tag{3.1}$$

for $x < 0$ and,

$$v_y = -\frac{v_{y0}}{2}\Big(1 + \tanh\big(0.015(z-800)\big)\Big)\tanh\big(2.0(x-6.0)\big) \tag{3.2}$$

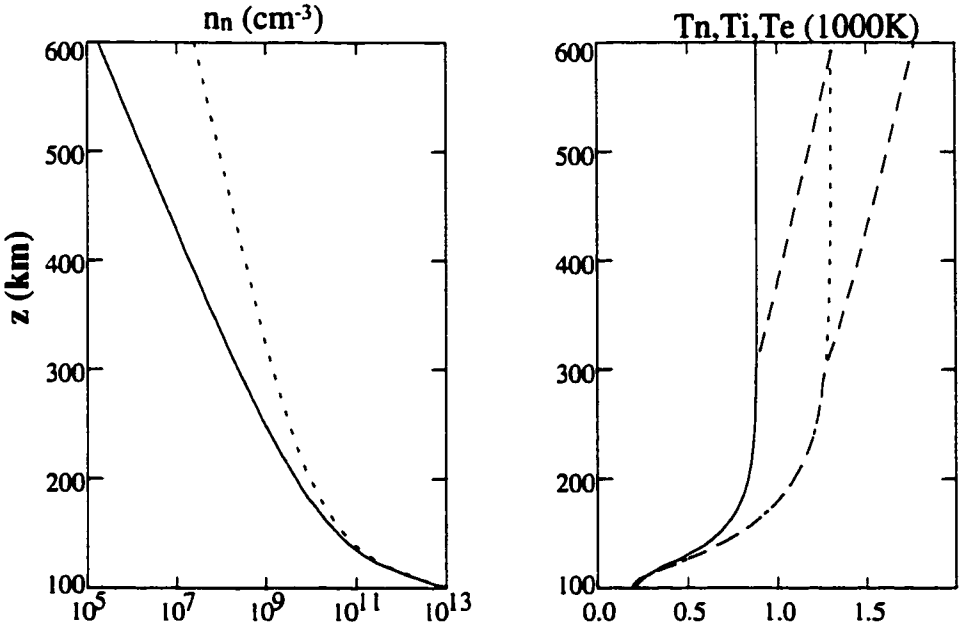

Figure 3.1: Altitude neutral density profile (left plot) for solar-min (solid) and solar-max (dotted) conditions and temperature profiles (right plot) for the neutral atmosphere (solid for solar min, dashed and dotted for solar max), for ions (initially identical to the neutrals) and for electrons (short dashes branching off the neutral temperature).

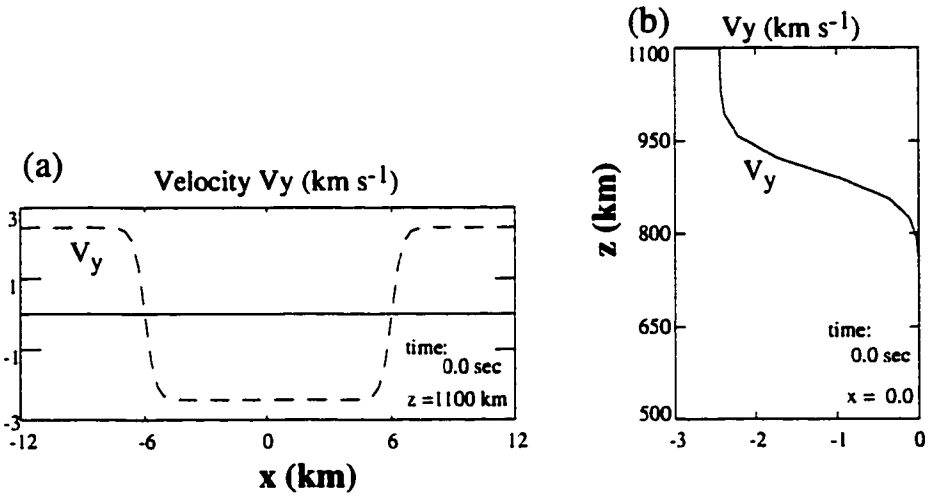

Figure 3.2: Initial velocity perturbation associated with the Alfvén waves in a horizontal cut at the top boundary (a) and in a vertical cut at $x = 0$ (b).

for $x \geq 0$, and the magnetic field pertubation is given by

$$B_y = -v_y(\mu_0\rho)^{1/2} \tag{3.3}$$

Note that the perturbation defined in (10), (11), and (12) contributes to the initial conditions and must be consistent with the boundary conditions.

This initial perturbation propagates into the ionosphere as a pair of Alfvén waves which produce two field-aligned current layers at $x = -6$ km (upward) and $x = 6$ km (downward). The amplitude is $v_{y0} = 1.0$ (in simulation units) which corresponds to 2.44 km/s. The velocity profile of the initial perturbation is shown in Figure 3.2 as a function of x and the plot in Figure 3.2b illustrates the altitude profile of the amplitude. The magnetospheric boundary condition is chosen such that the wavetrain maintains its amplitude. The structure of the Alfvén wave and the pair of FAC's is presented in the upper plot of Figure 3.3. The field-aligned current is closed by polarization currents at the leading edge of the wavetrains.

3.2 Simulation results: Ion and electron heating in the ionosphere

Various terms in equations (2.6) and (2.7) can increase the ion or electron temperature in the ionosphere. In the electron temperature equation (2.7) two source terms can heat electrons, i.e., the ohmic heating term $\eta j^2/\rho nk$ ($\mathbf{j} = \nabla \times \mathbf{B}$), and heating from energetic particle precipitation $\iota e_c/nk$. Thermal energy loss is due to thermal contact between electron and other particles, e.g., cooling due to electron-neutral collisions $\nu_{eff}(T_n - T_e)$ (rotational, vibrational, electronic excitations Roble [1996]), and cooling by ions $\nu_{ei}(T_i - T_e)$. The total pressure equation also includes a frictional (Joule) heating term $(\rho\frac{m_n\nu_{in}\rho}{m_i+m_n} + m_i\iota)(v - v_n)^2$ in addition to ohmic heating and particle precipitation. Ions and neutrals are heated by this

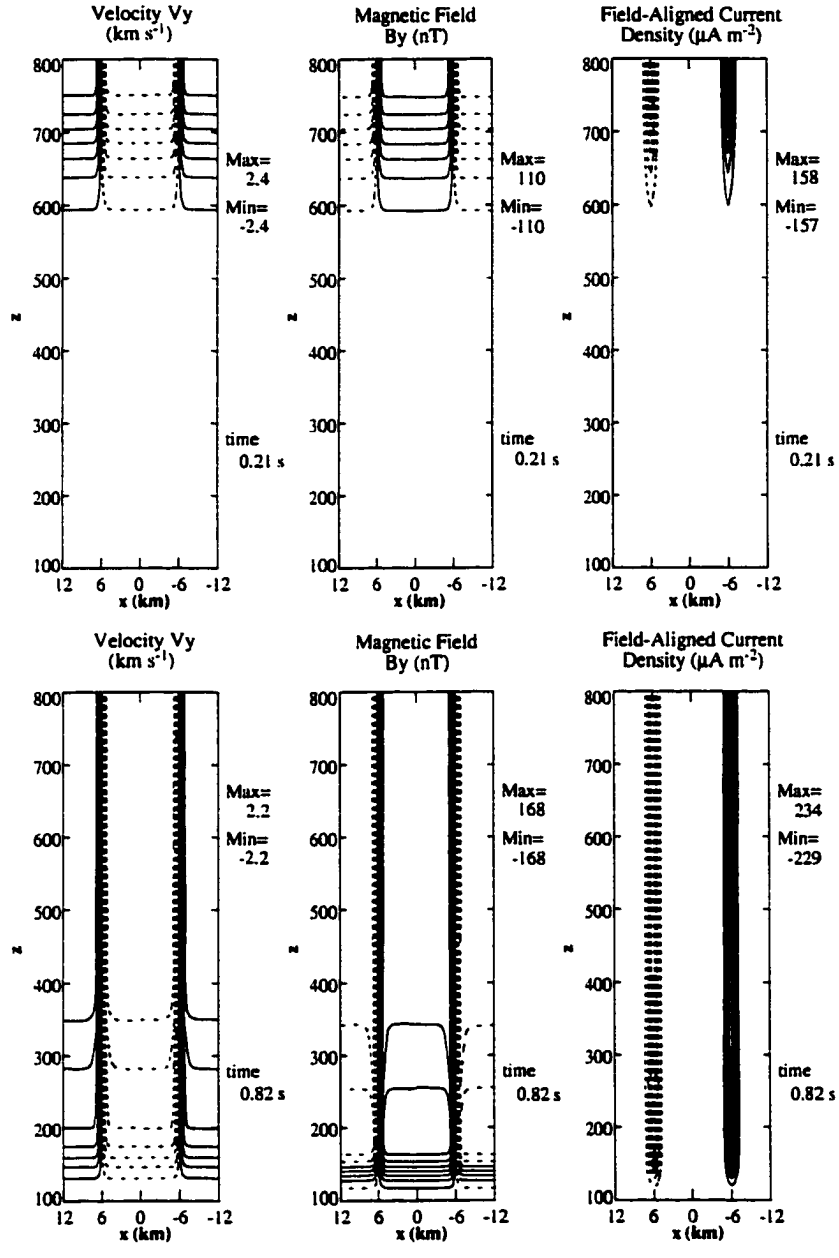

Figure 3.3: Two-dimensional contour plots for the velocity V_y, the magnetic field B_y, and the field-aligned current density j_y at time $t = 0.21$ second (top) and at $t = 0.82$ second (bottom).

process. Further, advection and heat conduction can alter the local temperature. Before I discuss my results, it seems helpful to give a brief illustration of the propagation of Alfvén waves in the ionosphere-magnetosphere system.

3.2.1 Alfvén wave propagation and reflection

The initial perturbation launches a pair of Alfvén waves carrying the velocity and magnetic field perturbations along the magnetic field. The pair of Alfvén waves is separated by upward and downward field-aligned currents. The waves travel with a speed of about 1000 km/s. In the lower ionosphere the waves are reflected in the region of enhanced Pedersen conductivity (i.e. larger collision frequency and friction) (e.g. Hughes and Southwood [1976]). The reflection coefficient is given by Maltsev *et al.* [1977]. The top plots of Figure 3.3 show the wave perturbations for v_y and B_y and the associated field-aligned current shortly after the start of the simulation. The lower plots in Figure 3.3 show the wave perturbations and the field-aligned current density shortly after the leading edge of the wave is reflected. The velocity of the reflected wave decreases while the magnetic field perturbation increases. The magnetic field perturbation and the field-aligned current density are about 50% larger at 200 km indicating a reflection coefficient of roughly 50%. The major portion of the field-aligned current is closed through a Pedersen current in the E region. A smaller polarization current is associated with the leading edge of the reflected wave.

A decrease in the plasma convection is caused by the upward wave vector of the reflected wave. Figure 3.4 shows a schematic of the wave propagation and reflection in terms of the magnetic field and velocity perturbation. This work considers only the case of very long wave lengths corresponding to frequencies larger than about 10 seconds. Ions are heated by the plasma-neutral friction in the convection which is switched on and modulated by the Alfvén waves and in the Pedersen current regions. A particular source for electron heating

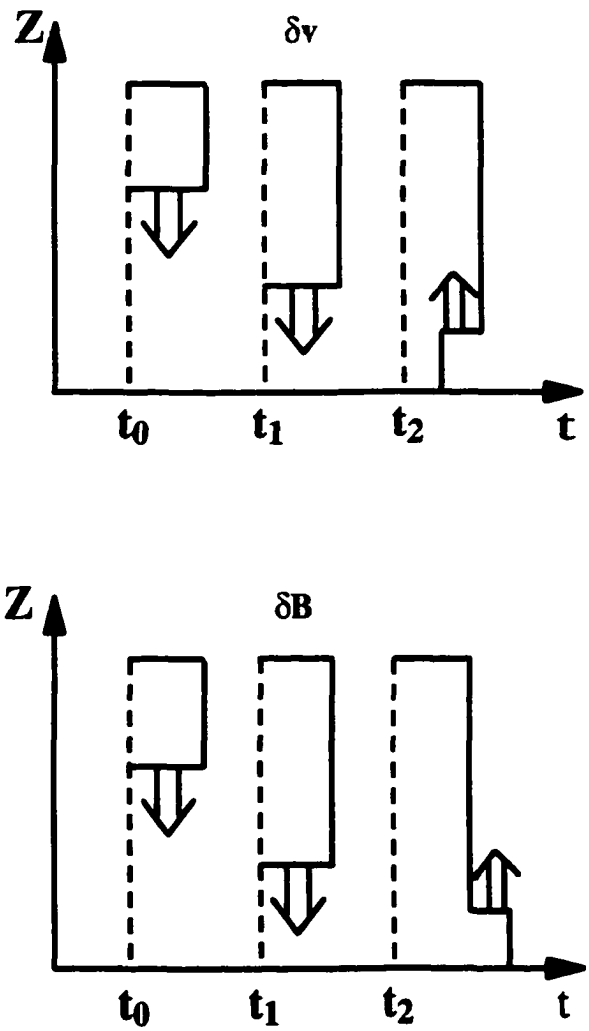

Figure 3.4: A sketch to illustrate the velocity and magnetic field perturbations for the incoming Alfén wave (t_0 and t_1) and shortly after the reflection (t_2).

associated with this configuration is the ohmic heating in the field-aligned current regions.

3.2.2 Ion heating by friction between ions and neutrals

We examined the ion heating by the frictional force between ions and neutrals for solar-min and solar-max conditions (Figure 3.1) with neutral temperature profiles from the MSIS model (Hedin [1991]). The simulation uses the initial perturbation given by equations (3.1), (3.2), and (3.3). Ion heating occurs for instance in the region between the two field-aligned current layers, i.e. around $x = 0$, where the ions are driven by the Alfvén wave. Figure 3.5 shows the ion temperature increase by frictional heating as a function of time for solar-min and solar-max conditions. The magnitude of the temperature increase and the height profiles are very different for the two cases, due primarily to the ionospheric conditions responsible for the reflection of the Alfvén waves. The simulation shown in Figure 3.5 was started with a symmetric perturbation and no initial Pedersen current. The presence of an initially asymmetric Pedersen current would yield asymmetric heating across the current layers, as observed by Lanchester99, and by Opgenoorth *et al.* [1990].

The ion heating $(\frac{m_n \nu_{in} \rho}{m_i + m_n} + m_i \iota)(v - v_n)^2$ in the total plasma energy (pressure) equation (2.6) is proportional to the collision frequency and to the square of the ion velocity (I assume $\mathbf{v_n} = 0$) when there is no particle precipitation. The collision frequency between ions and neutrals increases exponentially with decreasing height, thereby heating significantly the ions as the Alfvén wave propagates into the E region of the ionosphere. Heating increases with decreasing height until the wave is reflected (Hughes and Southwood [1976]). The reflected wave decreases the ion velocity with a corresponding decrease of the ion heating rate. Thermal contact between ions and neutrals cools the ions efficiently at low altitudes. As shown in Figure 3.5, the ion temperature initially reaches a maximum at low altitude. After reflection of the Alfvén wave, the maximum shifts to higher altitude. A deceleration

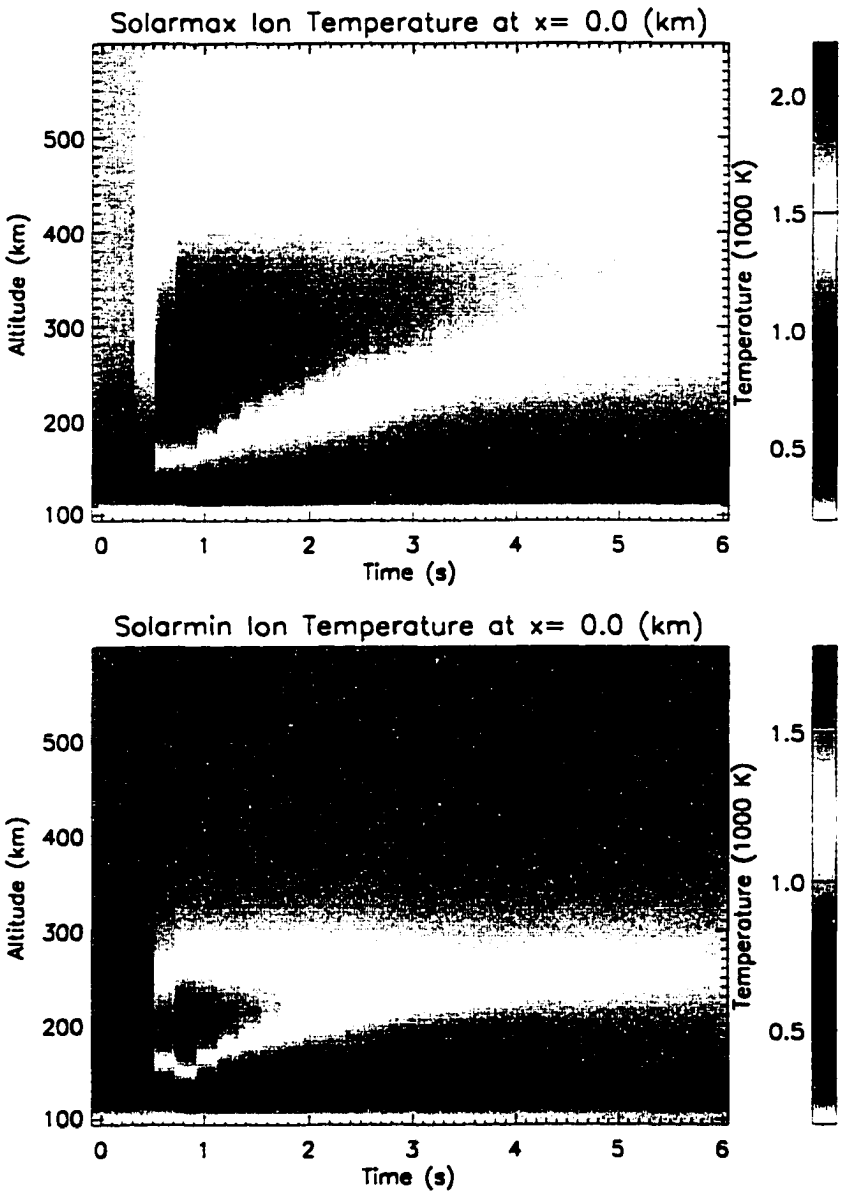

Figure 3.5: Altitude versus time plots of the ion temperature for solar-max (top) and solar-min (bottom) conditions.

of the convection velocity due to friction contributes to the decrease of ion heating.

3.2.3 Electron heating by particle precipitation

The simulation results on Alfvén wave propagation show that ions are strongly heated in the region outside the field-aligned current sheets. The electron temperature remains mostly unchanged during the process of increasing ion temperature. There are two source terms in the electron temperature equation (2.7), i.e., ohmic heating $\eta j^2/\rho nk$ in a field-aligned current layer and heating from ionization $\iota e_c/nk$.

Before discuss the results of electron heating by ionization, I first illustrate some basic physics. In the electron temperature equation (2.7), if we only consider the ionization source:

$$\frac{\partial T_e^\kappa}{\partial t} = \frac{\iota e_c}{nk} T_e^{\kappa-1} - \frac{\iota}{(\gamma-1)n} T_e^\kappa \tag{3.4}$$

Defining $T_c = \frac{\gamma-1}{k} e_c$, (14) can be rewritten

$$\frac{\partial T_e}{\partial t} = \frac{\iota}{n}(T_c - T_e) \tag{3.5}$$

For a typical value of $e_c = 2$ eV, we obtain $T_c = 1.55 \times 10^4$ K, which is much higher than the usual electron temperature in the ionosphere. Equation (3.5) shows that electron heating by ionization is proportional to the ionization rate and inversely proportional to the plasma number density. Electron heating by ionization is fast when the electron temperature is low, i.e. at the beginning of ionization. As the electron temperature increases, the heating rate by ionization slows down.

In my simulation the ionization rate is parameterized from the output of a 1-D tansport code (Lummerzheim [1992]). The input to the transport calculation is an energy flux of 40 mW m^{-2} with a characteristic energy E_{char} of 1.0 keV in a Maxwellian spectrum. The resulting height profile is shown in Figure 3.6. The ionization peak is at about 130 km. The

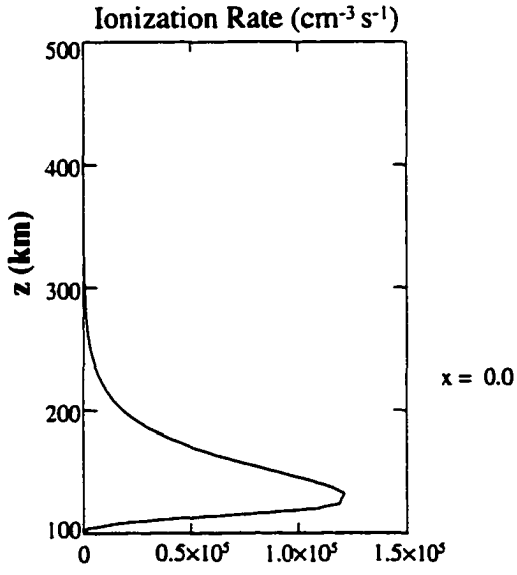

Figure 3.6: Height profile for the ionization rate for the solar-min case and an incident Maxwellian energy flux of 40 mW m^{-2} with a characteristic energy E_{char} of 1.0 keV.

resulting electron temperature from the simulation, adopting the ionization profile of Figure 3.6 for solar minimum conditions, is shown in the top panel of Figure 3.7. The ionization was applied only in a limited vicinity around $x = 0$.

The evolution of the electron temperature profile follows the physical arguments implied by equation (3.5). At early times the maximum electron temperature increase is at about 170 km, slightly higher than the altitude of maximum ionization rate. The initial number density increases with decreasing altitude (down to about 130 km, bottom panel of Figure 3.7). Thus the initial energy deposition per electron has a maximum slightly above the region of maximum density. As time proceeds the plasma number density at lower altitude increases faster due to ionization, such that energy deposition per electron decreases further. In addition, the cooling term $\nu_{eff}(T_e - T_n)$ in the electron temperature equation is large at lower altitudes. The combined effect shifts the maximum electron temperature to higher altitude. Heat conduction also contributes to this shift as we will show later.

The ion temperature change, in this case, is very similar to that shown in Figure 3.5 (solar-min). The only difference is that the ionization changes the density profile and reflection properties for the Alfvén wave which, however, does not change the heating profile significantly.

3.2.4 Electron heating by ohmic dissipation

A strong field-aligned current heats the electrons by ohmic dissipation. The heating rate is given by ηj^2 where η is the resistivity and $\mathbf{j}$ is the current density. In the field-aligned current layer simulation (Figure 3.3), the initial plasma flow and the sheared magnetic field generate two field-aligned current layers, with the upward current layer at $x = -6$ km and downward current layer at $x = 6$ km. As the perturbation propagates with the Alfvén wave into the ionosphere, the two field-aligned current layers expand over the entire

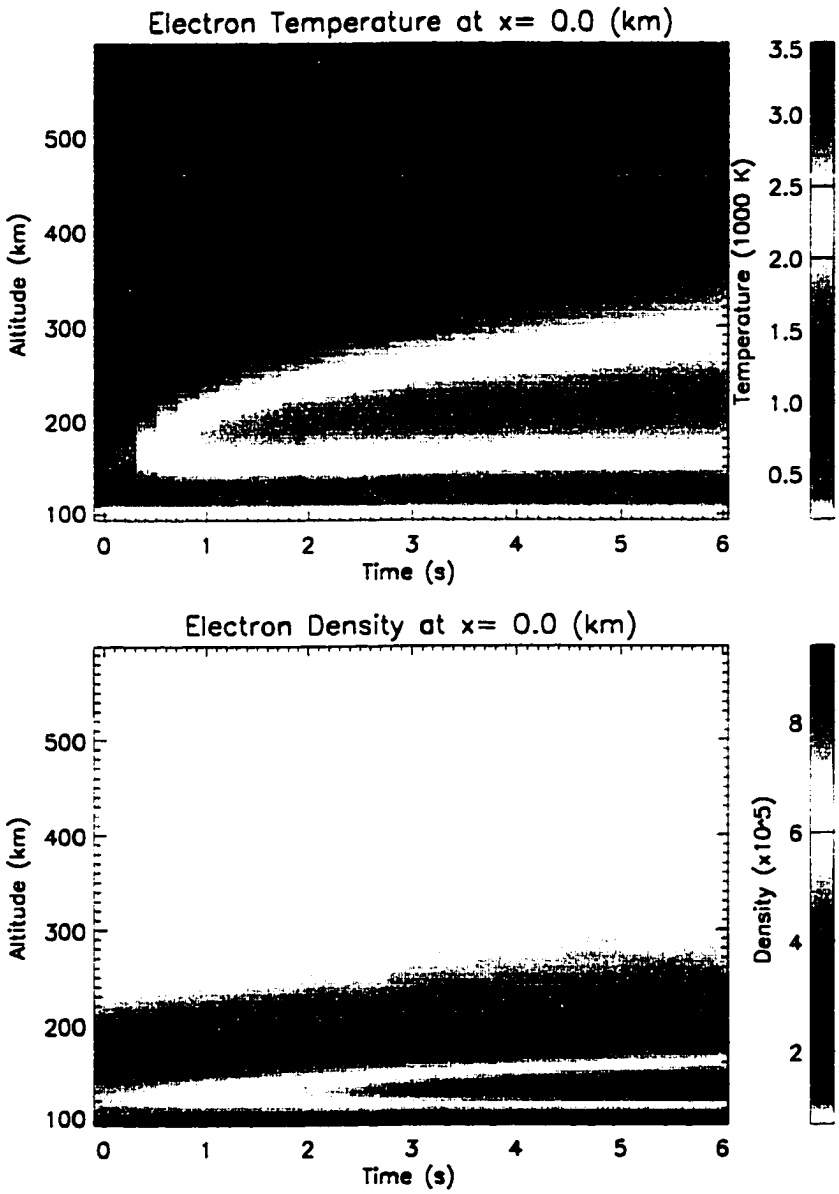

Figure 3.7: Electron temperature evolution (top) and number density (bottom) for the ionization shown in figure 3.6.

simulation box. Reflection of the Alfvén wave increases the amplitude of the magnetic field perturbation, resulting in an increase of the current density with time as the current sheets develop. In Figure 3.3, it is shown that at $t = 0.82$ second, just after the wave is reflected, the magnetic field perturbation is enhanced from 110 nT to 170 nT, and the field-aligned current is increased to about 230 μA m^{-2}. Such values are large but not unreasonable for filamentary aurora (e.g., Lanchester *et al.* [1997]; Stasiewicz and Potemra [1998]; Stasiewicz *et al.* [1998]).

Figure 3.8a shows details of the field-aligned current structure, the velocity perturbation, v_y, the magnetic field perturbation, b_y and the field-aligned current, j_z at $t = 4$ second. Figure 3.8b shows the vector plot of the field-aligned current and the electron velocity as well as the ion velocity. Note that both upward and downward field-aligned currents are carried by electrons, while the closing Pedersen current at about 117 km is carried by ions.

I examine electron heating by ohmic dissipation in the absence of precipitation at the center of the upward current layer. Figure 3.9 shows a plot of the parallel resistivity at the center of the upward current layer. The resistivity decreases exponentially with altitude. Since the current density is almost constant with altitude, the ohmic heating rate should be maximum at the lower end of the field-aligned current layer and decrease exponentially with the altitude. Electron cooling by collisions with neutrals and ions increases with decreasing altitude. Therefore the change of electron temperature is the result of both heating and cooling.

Figure 3.10 shows the electron temperature evolution at the center of the upward field-aligned current. The electron temperature changes are due to the combined effect of ohmic heating and collisional cooling. As the field-aligned current propagates into the ionosphere, the electrons at higher altitude are heated first. The heat source moves down to lower altitudes with the Alfvén wave. It takes only about 0.6 seconds for the Alfvén wave to

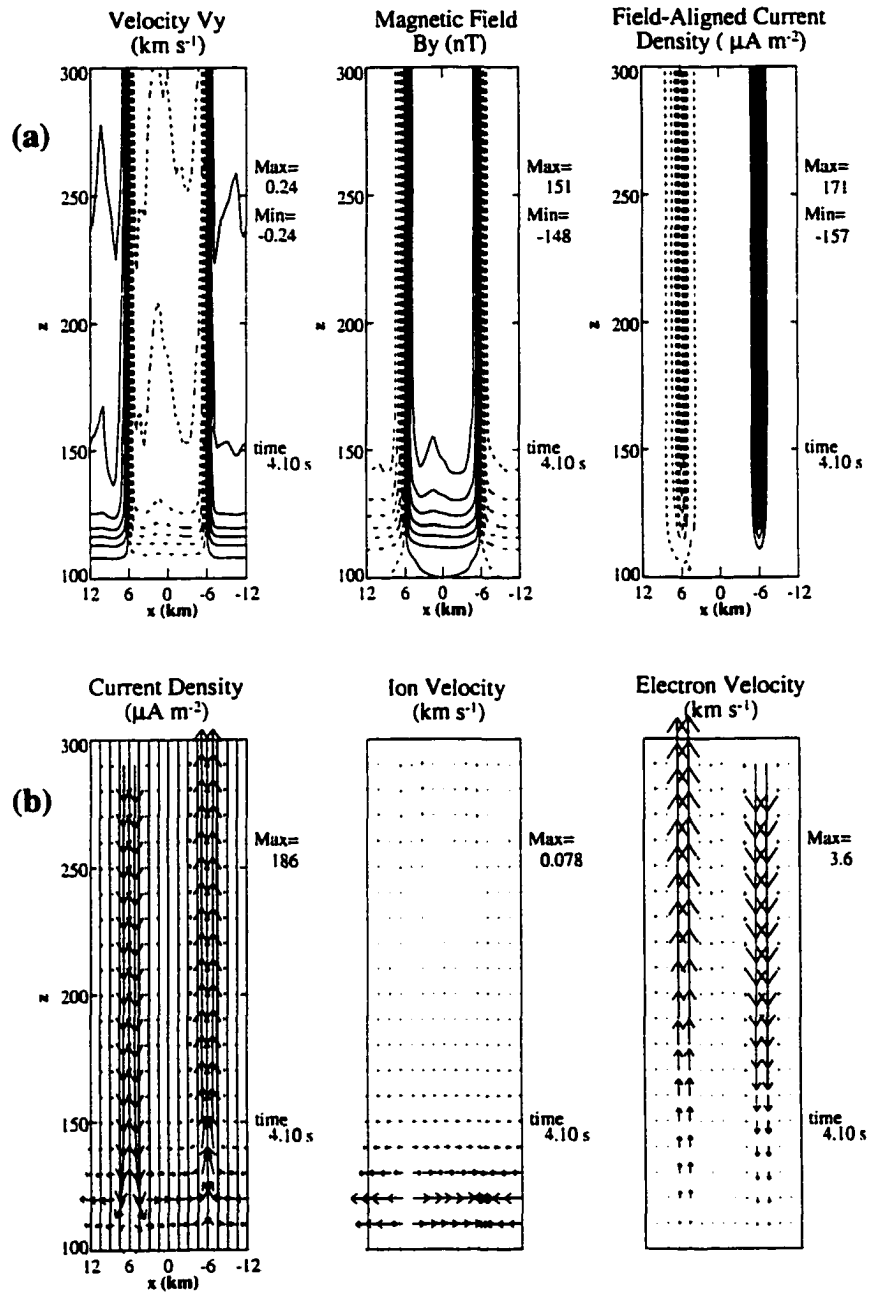

Figure 3.8: Two-dimensional contour plots of velocity V_y, magnetic field B_y, field-aligned current density j_y (top row), and vector plots of current density, ion velocity, and electron velocity (bottom row) for the solar-min case without precipitation.

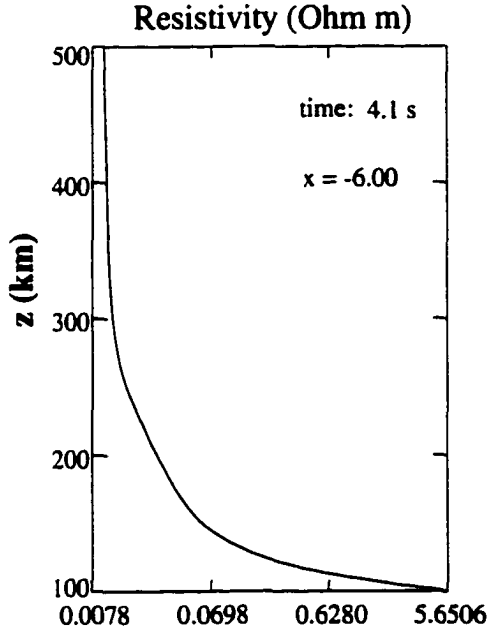

Figure 3.9: Parallel resistivity in the upward current layer ($x = -6$ km) at time $t = 4.1$ seconds.

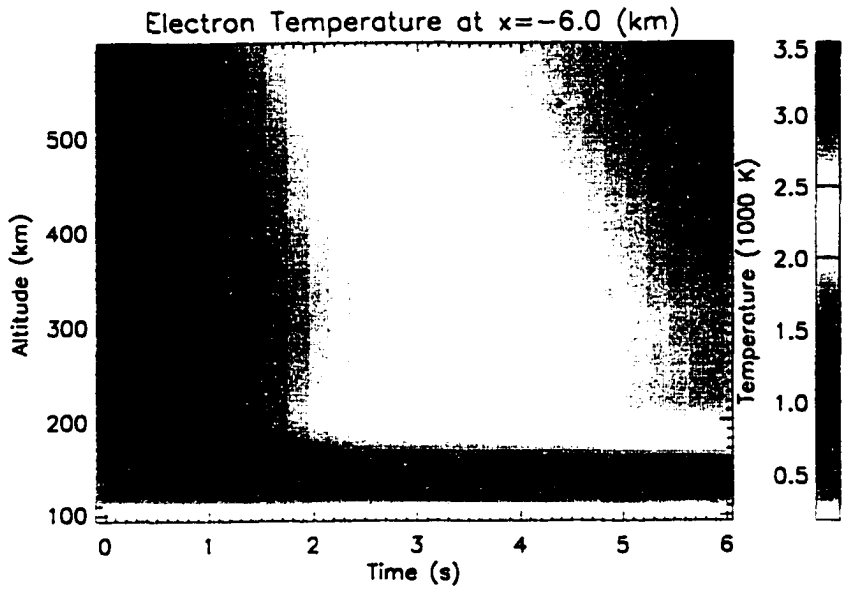

Figure 3.10: Electron temperature evolution for the solar-min case in the upward current layer at ($x = -6$ km).

arrive at the lower boundary. After about 2 seconds, the balance between heating and cooling yields a maximum electron temperature at about 200 km. The lower boundary of the large electron temperature increase appears as low as 170 km. Note that ohmic dissipation has a negligible effect on ion heating.

3.2.5 Sources and losses for the electron temperature

Figures 3.11a and 3.11b illustrate the contributions of various source and loss terms to the evolution of the electron temperature in eV s^{-1} per particle for the cases of precipitation (3.11a) and ohmic heating in the upward FAC region (3.11b). The heavy solid line in the plots represents the sum of all source and loss terms. For the case of precipitation, electron heating in the upper ionosphere is due to heat conduction. In the lower portion of the ionosphere the electron temperature is close to a steady state where the heating by particle precipitation and losses due to electron-neutral interaction and heat conduction balance each other. There is a small negative residual in the overall temperature evolution at lower altitudes. This is caused by the increasing number of electrons due to precipitation such that the heating per particle from precipitation is slowly decreasing in time. The temperature maximum at this time is at about 220 km altitude. Neutral collisions become rare at this altitude that the dominant transport is through heat conduction.

In the case of ohmic heating (Figure 3.11b) the lower portion of the electron temperature is also close to a steady state. However, different from the precipitation case, the upper part of the current layer (above 250 km) is still heated. Since the upper temperature profile shows a very small gradient, heat conduction is less important than in the precipitation case. The dominant source for energy input is the ohmic heating. A significant additional source for energy deposition or transport is advection in the region with a large gradient in the electron temperature. Note that the field-aligned current implies an electron drift

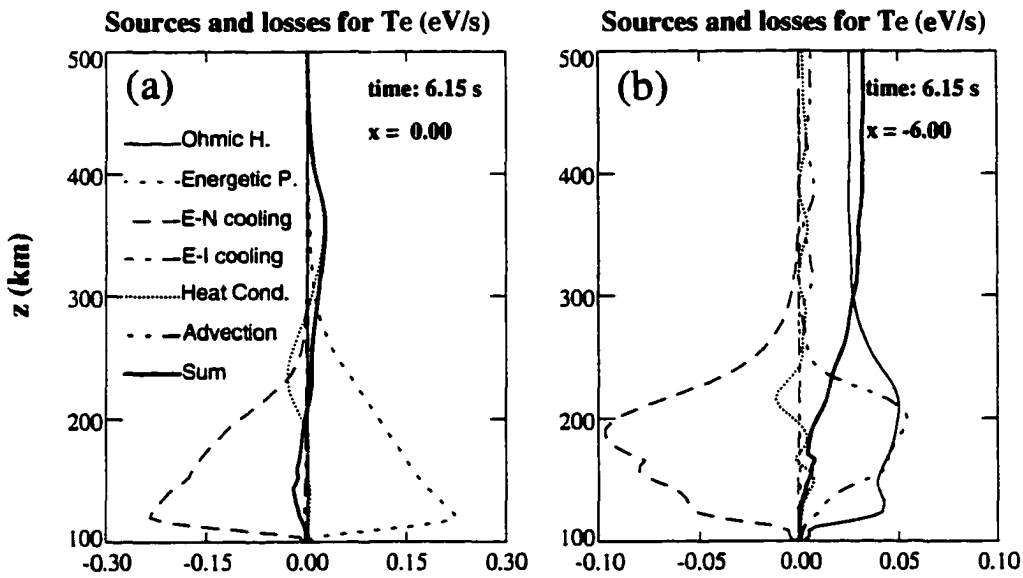

Figure 3.11: Plot of source and loss terms for the electron temperature for the precipitation case (a) shown in 3.7 and for the ohmic heating case (b) shown in 3.10.

of about 4 km s^{-1}. The transport by convection provides a positive contribution in the upward current layer and (without illustration) a negative one in the downward current layer (because cold material is carried upward). In the lower portion of the ionosphere the positive source terms are efficiently compensated by electron neutral collisions.

The characteristic time scale to achieve a steady state increases with height because the electron-neutral collision frequency is exponentially decreasing with altitude. This leads to an evolution where a steady electron temperature is assumed to occur faster in the lower ionosphere.

3.3 Comparison with radar observation

The EISCAT radar and optical observations (January 28, 1995) are presented and discussed in detail in Lanchester99. The event was characterized by the presence of filamentary aurora in the field of view of the radar and imagers. Figure 3.12 (contributed by B. Lanchester) shows radar observation data of a discrete aurora event on January 28, 1995. From the top, the first three panels show the ion temperature, electron temperature, and the electron number density variations, respectively, in the altitude range between 150 km and 350 km. The bottom panel shows a better resolved electron number density change at the altitude below 140 km.

The data show an initial increase of the ion temperature in a region of decreasing electron density and temperature. During the subsequent decrease in ion temperature the electron temperature suddenly increased. The increase in T_e occurred without a corresponding electron density increase, which followed a few seconds later.

Figure 3.13 shows the ion and electron temperatures and the electron density as functions of horizontal distance across the current layer (x) for three fixed altitudes and time $t = 6.15$s for the case without particle precipitation. Early in the simulation, ions are strongly heated

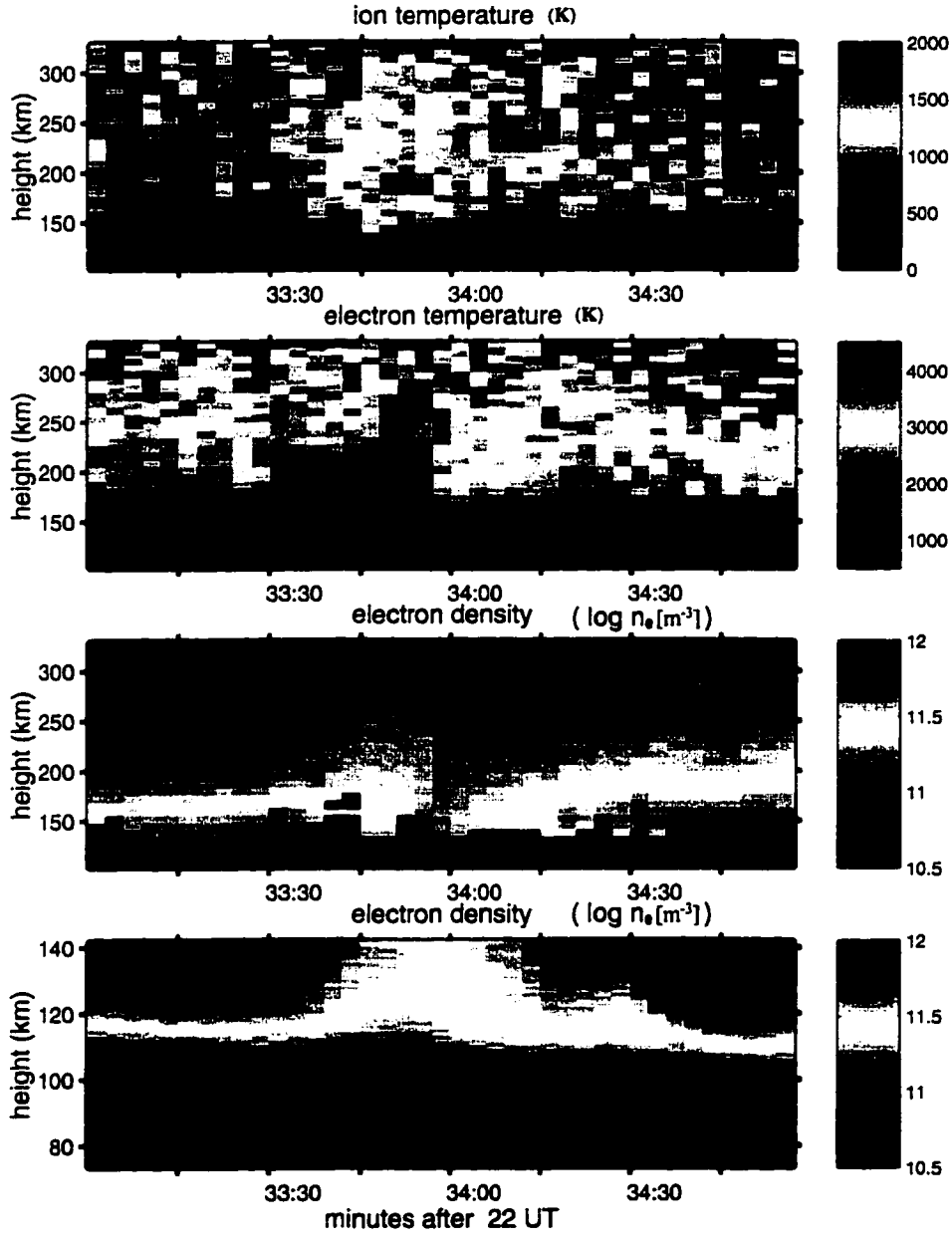

Figure 3.12: Radar observation of a discrete auroral event on January 28, 1995 (Provided by B. Lanchester). Notice that there are no data below 140 km in the second and third panels, and below 90 km in the bottom panel.

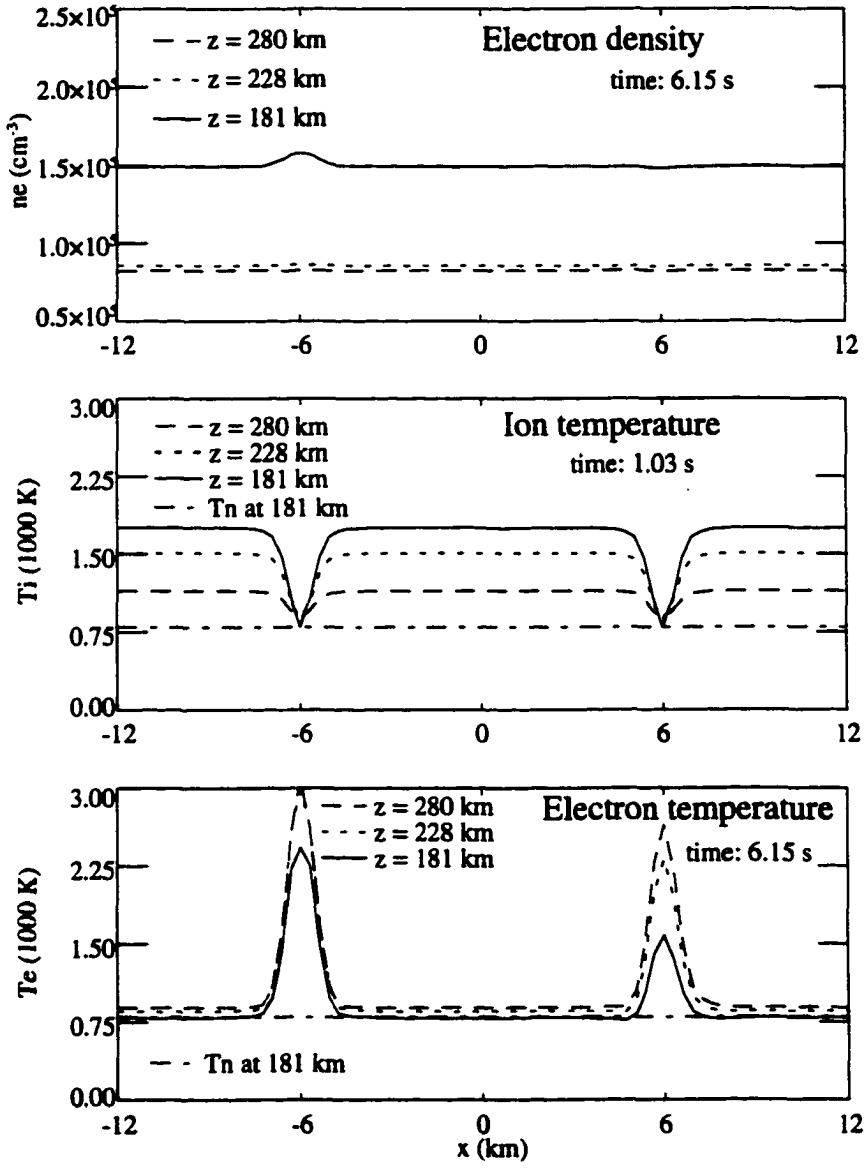

Figure 3.13: Profile of electron density (top), ion temperature (middle), and electron temperature (bottom) as a function of x for time $t = 6.15$ seconds and for three fixed altitudes (181 km, 228 km, and 281 km). The plot is for the case without precipitation.

in the region outside the current layers. The maximum ion heating appears below 200 km (compare Figure 3.5). After 6 seconds the electron temperature inside both current layers ($x = \pm 6$ km) increases significantly, up to 3000 K.

My simulation shows a number of the properties which characterize the observed event. Assuming that the radar field of view is first in a region outside the field-aligned current, then inside the field-aligned current, and finally in a region with enhanced electron precipitation, one would expect to observe:

1. Ion temperature with a temporal profile similar to that illustrated in Figure 3.5; since there is no significant precipitation in this region, electron density and temperature are constant or slowly decreasing. The event starts with ion heating shortly after 22:33:30 (UT) (Lanchester99). The initially strong ion heating starts at about 170 km. The ion temperature maximum then moves to higher altitudes. The observations were acquired during solar-min conditions. Both the altitude progression and the temporal profile of the ion temperature are similar to the ion temperature for solar-min conditions in our simulation (bottom panel of Figure 3.5). During ion heating, both the electron density and temperature slowly decrease.

2. A rapid increase in electron temperature when the FAC comes into the field of view: At the same time, the ion temperature should decrease to the background level (Figure 3.13) because the fast ion flow is outside the FAC region. EISCAT data (Figure 3.12) show a sudden increase of electron temperature just after the ion heating. At the beginning of the electron heating, the electron density decreases. The initial electron heating region extends from about 170 km to higher altitudes. The electron temperature increases to above 3000K. Since the electron density is decreasing at this time, the heating is expected to be due to a source other than precipitation. Our simulation results (top panel of Figure 3.10) show that the electron temperature inside the current layer increases up to about 3000K in a

few seconds. The altitude extent of electron heating also agrees with the observed data, i.e., from 170 km to higher altitudes. At the time of electron heating by the field-aligned current, the ion temperature decreases to the background level.

3. An increase of the electron density when the precipitation comes into the field of view. This is not a self-consistent result of the present 2D fluid model but has to be assumed as a boundary condition for the incoming electron flux, similar to the 1D transport model of Lanchester99. Shortly after the start of the electron heating, the electron density increases, which indicates that the field of view is in a region of particle precipitation. From 22:34:00 (UT) to about 22:34:30 (UT), the electron density continues to increase, with a maximum at about 130 km, which corresponds to particle precipitation with characteristic energy 1.0 keV (Figure 3.6). The electron temperature further increases at the same time with the maximum slightly above 3000 K. However, the bottom edge of the electron heating region moves to higher altitude, and there is strong electron heating at altitudes above 200 km. Our simulation results of electron heating by particle precipitation (top panel of Figure 3.7) shows reasonably good agreement. After 22:34:30 (UT), the electron density increases at lower altitude with a maximum at about 125 km. This indicates that the characteristic energy of precipitation increased to a higher value, resulting in energy deposition at lower altitudes.

Figure 3.14 illustrates a result where I included two additional properties compared to the results shown in Figure 3.13. I added an Alfvén wave with constant amplitude of half the value for the two original Alfvén wave trains to include a large scale convection. This yields a larger convection velocity in the region $x < -6$ km (and $x > 6$ km). We also included particle precipitation in the region -5 km $\leq x \leq 5$ km with the same energy flux and characteristic energy as for the result of Figure 3.7. The result in Figure 3.14 shows density, ion temperature, and electron temperature in time intervals of 1 second (covering

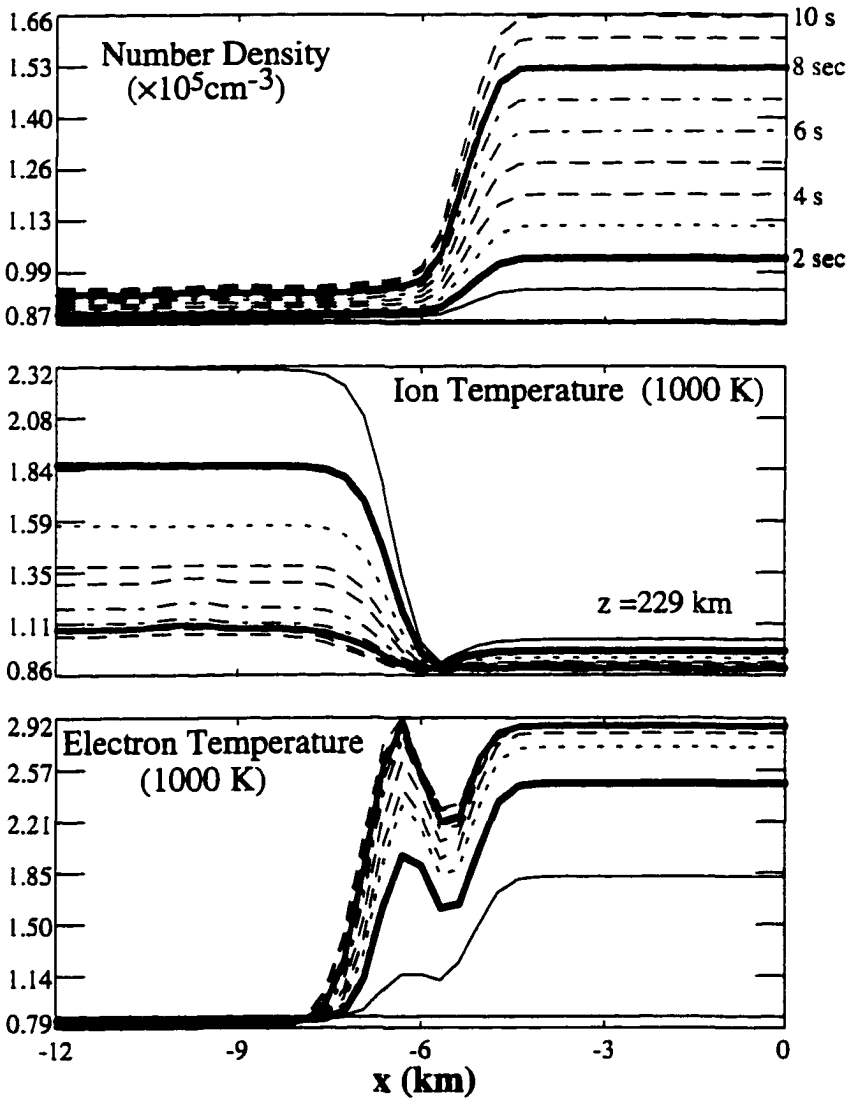

Figure 3.14: Profile of electron density (top), ion temperature (middle), and electron temperature (bottom) as a function of x for 11 different times (1 second apart) for the altitude 229 km. The case uses precitpitation in the region -5 km $\leq x \leq 5$ km and a modification of the Alfvén waves (see text).

a total of 10 seconds) as a function of x for a constant altitude of 229 km. A scan through this structure from left to right shows the basic sequence of the EISCAT event. It should, however, be noted that this is not a unique quantitative result for such a scan because this depends on how fast the the scan is performed (or how fast the stucture moves). Note that I also used an average over about 1 km to emulate the field of view of the radar. I did not average over time in Figure 3.14. The small gap in the electron temperature depends on the precise location of the precipitation region relative to the location of the field-aligned current.

While the overall situation seems to be captured relatively well, quantitative aspects of the 2-D simulation are certainly different. In my simulation, I did not attempt to introduce a time varying ionization rate to obtain a best fit. Figure 3.14 illustrates that a scan through a two-dimensional fast evolving structure cannot yield a unique result. The precise distribution and time history of the Alfvénic perturbations are not known and are likely more complicated than in the simplified smooth model adopted here. However, it is shown that a strong filamentary current layer has characteristic properties in terms of convection, ion heating, and electron heating.

3.4 Summary and discussion

In this chapter, I have reported the first results from a new two-dimensional three-fluid code with application to electromagnetic coupling between the ionosphere and the magnetosphere. The simulation solves the continuity, momentum, and energy equations for neutral, ion, and electron fluid components. The ionospheric transport parameters are computed from standard formulations for the collision frequencies and the code uses methods typically applied in one-dimensional transport computations to determine ionization, recombination, and electron cooling rates. The model includes ion inertia, such that the

typical fluid plasma waves are a part of the simulation. This is particularly important for the magnetosphere-ionosphere system in which Alfvén waves are central for the interaction between the two systems. Consequently, the simulation code is well suited to describe fast temporal and small spatial changes in the ionosphere.

The two-dimensional model cannot address the deformation of FAC and discrete aurora along the auroral curtain, which requires three dimensions. However, it provides a realistic model for the formation of FAC layers by Alfvénic perturbations.

The results of this chapter focus on various mechanisms of ion and electron heating. The motivation for this focus is three-fold. First it demonstrates that the code obtains reasonable quantitative results for these heating mechanisms. Second, the demonstrated heating processes depend on a temporal and spatial variation of the magnetospheric input. Finally, radar and optical observations of ion and electron temperatures and ionization in an auroral event are reproduced in many respects by the 2-D simulations. Based on my results I suggest that the sequence of events reported in Lanchester99 is in part caused by the spatial structure of convection, field-aligned currents, and precipitation, in or close to the particular auroral arc structure.

For the simulation I employ boundary and initial conditions that cause Alfvén waves to propagate from the magnetosphere into the ionosphere. If the velocity and flow perturbation of the waves changes (reverses sign) across a vertical boundary the waves carry a field-aligned current into the ionosphere.

I have demonstrated that the impact of the horizontal ion flow carried by the wave leads to fast ion heating first at lower ionospheric altitudes. The partial reflection of the wave (with a corresponding decrease in the flow velocity) and the large ion-neutral thermal contact at lower altitudes leads to a subsequent shift of the maximum ion temperature to higher altitudes. This heating does not affect the electrons. Our model predicts the

correct temporal evolution on short time scales from wave reflection, ion-neutral friction, and cooling by neutrals.

The results demonstrate very significant electron heating by ohmic dissipation within a strong field-aligned current. The ohmic heating in field-aligned currents is neglected by most other models since it is of no significance on sufficiently large scales. Our model determines the current density self-consistently as a function of time for given magnetospheric boundary conditions. The horizontal ion velocity is much smaller in the current layer than outside such that ion heating is small inside the layer.

It is often assumed that discrete auroral arcs are associated with upward field-aligned current regions and corresponding Alfvénic perturbations (e.g. Lanchester and Rees [1987]; Seyler [1988]; Seyler [1990]; Otto and Birk [1992]; Otto and Birk [1993]; Haerendel [1994]; Lanchester *et al.* [1997]; and Stasiewicz *et al.* [1998]). Thus, electron precipitation should be expected in a small region within or next to the current layer. The transport model results of Lanchester99 demonstrate excellent agreement for the electron density profile and evolution. However, there is a large discrepancy for the electron temperature without a heating source other than precipitation. Including a significant field-aligned current density can explain the rapid heating. Our results complemented by the one-dimensional tranport result of Lanchester99 provide strong evidence for large field-aligned current densities in or next to discrete aurora.

Chapter 4

Field-Aligned Current

The field-aligned currents (FAC) are the bridge which connects the ionosphere to the magnetosphere. The study of the FAC is critical in understanding the dynamics of the ionosphere-magnetosphere coupling processes. At the beginning of the twentieth century, based on the fact that the luminescence of the aurora is mostly along the magnetic field lines, Kristian Birkeland, a Norwegian scientist, first hypothesized the existence of FAC in the high latitude ionosphere-magnetosphere system and suggested that the connection of these field-aligned currents to the horizontal ionospheric currents closes the ionosphere-magnetosphere electric circuit. So the field-aligned current is often called Birkeland current. This foresighted idea had been debated among researchers due to lack of support from direct observation until the late 60s, when a large amount of data were obtained from satellite observations.

Satellite observation has provided us a unique way to study the field-aligned current in the magnetosphere-ionosphere system. By using $\mathbf{J} = \nabla \times \mathbf{B}$, the magnitude, location and the direction of the field-aligned current can be determined by the horizontal magnetic field perturbations (Zmuda *et al.* [1966]). The magnetometer on TRIAD (the first polar orbited satellite) observed a large magnetic field perturbation in the east-west component

which indicates a current in the vertical direction (i.e. the FAC). Based on the data from the TRIAD, Iijima and Potemra [1978] summarized the large scale FAC distribution in the high latitude ionosphere (Figure 4.1). Several large scale models have been developed to study the large scale FAC in the ionosphere-magnetosphere system (e.g. Wolf [1975]; Boström [1968]; and Rostoker and Boström [1974]). These large scale models have suggested different mechanisms for the closure of the FAC in the magnetosphere.

The large scale FAC pattern is an average picture. However, the purpose of this thesis is to study the dynamics of the small scale ionospheric structures such as the discrete aurora which has a spatial scale between 100 m and 10 km . Recently, by using a much simplified height-resolved ionosphere-magnetosphere coupling model (a MHD model added with an ion-neutral friction term in the ion's momentum equation), Dreher [1997] studied the dynamics of the small scale FAC in the ionosphere with interesting results. There, he simply prescribed a certain altitude profile of the ion-neutral collision frequency in the ion-neutral friction term. It turns out that this prescribed ion-neutral collision frequency profile provides the Pedersen conductivity needed to close the field-aligned current with the ionospheric Pedersen current. Another important result from Dreher's simulation is the suggestion that the plasma density irregularities in the E-region of the ionosphere are a result of the current closure. Since it does not solve the ion-neutral collision frequency self-consistently (because there are no neutral equations in the code), and neglects the electron energy equation, this model cannot resolve other important ionospheric properties such as ionospheric heating and the phenomena associated with the change of the ionospheric conductivities.

My two dimensional three-fluid model is the first model that can resolve the dynamic and nonlinear electromagnetic interaction between the ionosphere and the magnetosphere with a realistic height-resolved neutral atmosphere. In this chapter, I will show some new,

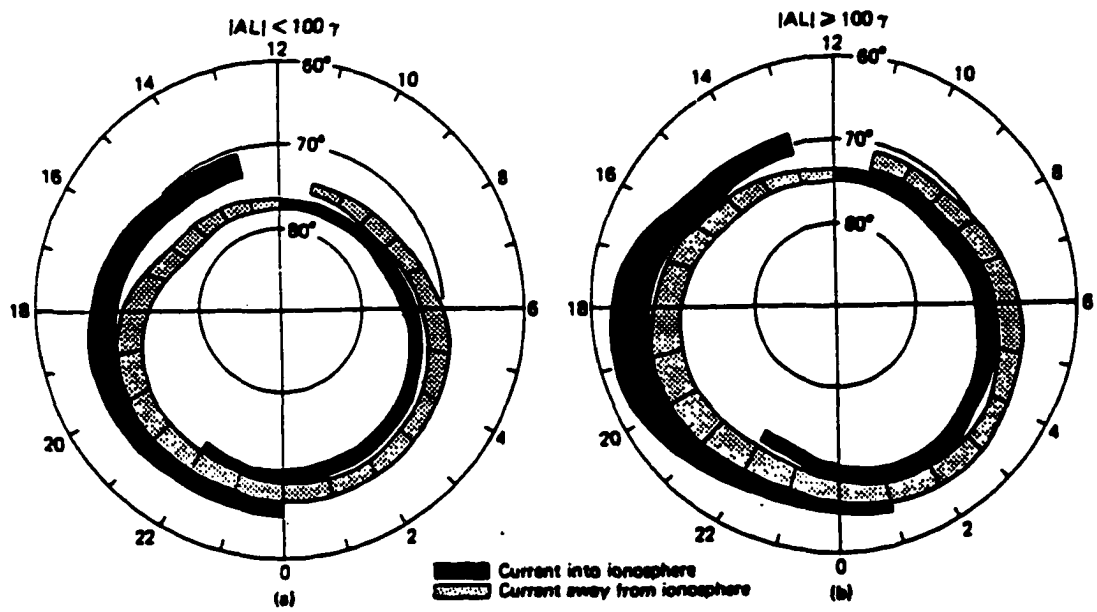

Figure 4.1: Two overlapping rings of field-aligned currents always exist at the high latitudes, in the same region of the auroral oval. During quiet times, the FAC pattern occurs at higher latitude and with small latitude extent. The inner and outer rings are called region 1 and region 2 current respectively. (Iijima and Potemra [1978])

interesting results of the field-aligned currents and their effects on the ionosphere.

4.1 Equilibrium and initial perturbation

The system is initially set in force equilibrium, i.e. neutral hydrostatic equilibrium. The total neutral number density n_n is the sum of three species, i.e., molecular nitrogen, atomic oxygen, and molecular oxygen, because these three are the dominant species and have important contributions in ionization and electron cooling processes. The neutral mass used in the simulation is an effective mass m_{eff}, which is a weighted average of the above three species. I use the data for the solar maximum condition from the MSIS model (Hedin [1991]) to determine the initial neutral density and temperature profile. The initial neutral temperature at the higher altitudes is chosen to be 1300 K. The initialization of plasma temperature, number density, and pressure profile is described in section 3.1.

The following perturbations are set at the beginning of the simulation:

$$v_y = \frac{v_{y0}}{2}\Big(1 + tanh\big(0.015(z-800)\big)\Big)tanh\big(2.0(x+6.0)\big) \tag{4.1}$$

for $x < 0$ and,

$$v_y = -\frac{v_{y0}}{2}\Big(1 + tanh\big(0.015(z-800)\big)\Big)tanh\big(2.0(x-6.0)\big) \tag{4.2}$$

for $x \geq 0$.

This is the sheared magnetic field and plasma flow perturbation at the top boundary (Figure 4.2) which generates two field-aligned current layers at $x = -6$ km (upward) and $x = 6$ km (downward). The amplitude of this perturbation is $v_{y0} = 0.205$ in simulation unit which corresponds to 500 m/s .

Current Layer Formation:

- Formation of a field-aligned current layer:
  - Sheared plasma flow
  - Alfven wave propagation

Perturbation at the magnetospheric boundary:

$$\delta B_y = -\frac{\delta V_y}{V_A} B_{dipole}$$

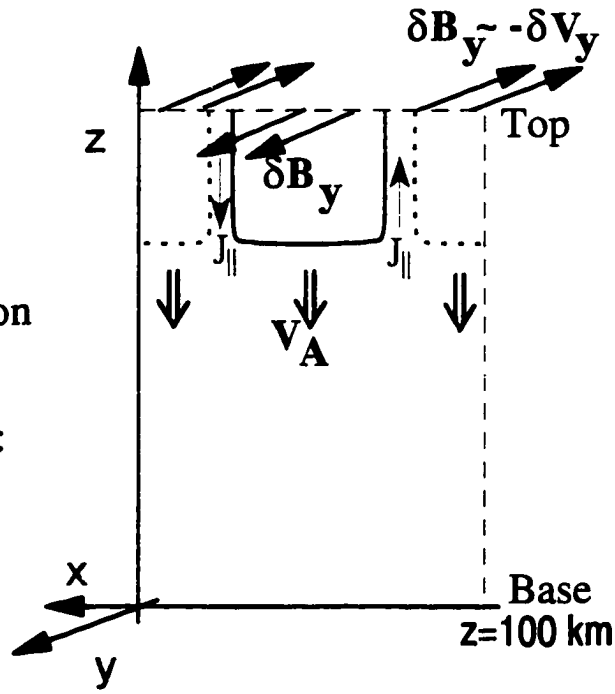

Figure 4.2: A sketch of the Alfvén wave propagation and the FAC formation.

4.1.1 Boundary conditions

The boundary conditions in the simulations of this work are mostly the same as those in section 3.1 except the one for velocity at the top boundary. In this work, I keep the plasma shear flow (velocity) perturbation fixed.

4.2 Results

4.2.1 Alfvén wave propagation and reflection in the ionosphere and the current layer formation

Figure 4.2 shows the sketch of the initial sheared magnetic field and plasma velocity perturbations. These perturbations propagate with Alfvén waves into the ionosphere and generate two field-aligned current layers. When the wave front gets into the ionosphere where the collision frequencies between plasma and neutral are large, part of the wave energy is lost due to the Joule dissipation in the ionosphere associated with Pedersen current, and part of the wave is reflected back to the magnetosphere. The reflection of an Alfvén wave in the ionosphere has been theoretically studied by Hughes and Southwood [1976], Maltsev *et al.* [1977], Newton *et al.* [1978], Ellis and Southwood [1983], and Yark and Southwood [1986]. All these authors studied the total effect of the Alfvén wave reflection by the ionosphere, i.e. they treat the ionosphere as a conducting layer and use the height integrated Pedersen conductivity to calculate the reflection coefficient. By doing this, they assume that the horizontal electric field is constant along the magnetic field line. The reflection coefficient, R, is given by (Maltsev *et al.* [1977]):

$$R = \frac{\Sigma_P - \Sigma_A}{\Sigma_P + \Sigma_A} \tag{4.3}$$

Where Σ_P is the height integrated Pedersen conductivity and $\Sigma_A = (\mu_0 V_A)^{-1}$ with V_A the Alfvén velocity.

The reflection coefficient R is strongly dependent on the height integrated Pedersen conductivity Σ_P. When Σ_P is large, the reflection is more efficient, and for small Σ_P the reflection is less efficient. The Pedersen conductivity is given by:

$$\sigma_P = \frac{en}{B}\left(\frac{\nu_{en}\omega_{ce}}{\omega_{ce}^2+\nu_{en}^2}+\frac{\nu_{in}\omega_{ci}}{\omega_{ci}^2+\nu_{in}^2}\right) \tag{4.4}$$

Where ω_{ce} and ω_{ci} are electron and ion gyro-frequencies respectively, ν_{en} and ν_{in} are electron-neutral and ion-neutral collision frequencies.

To use the height integrated Pedersen conductivity, one has to assume that the electric field along the magnetic field line is constant which implies a steady state assumption. In my study, I use the full dynamics of the propagation as well as reflection of Alfvén waves in the ionosphere-magnetosphere system. My results show the details of the Alfvén wave reflection processes in the ionosphere with better temporal and spatial resolution. Figure 4.3 shows a time sequence of the Alfvén wave propagation along the magnetic field line from the magnetosphere into the ionosphere at the earlier times of the simulation. We see that during the early time, before the Alfvén wave reaches the lower ionosphere, the amplitude of the magnetic field perturbation increases slightly with time as the wave is propagating. This indicates that the wave is gradually reflected (Zhu *et al.* [1999]). The major part of the Alfvén wave reflection is achieved when the wave reaches the lower E-region of the ionosphere (after 0.82 s) where the Pedersen conductivity is very large. The mechanism of the reflection is the friction between plasma and neutrals. The Pedersen conductivity is the quantity describing the plasma-neutral friction and it is determined by the collision frequencies between plasma and neutral (i.e. ν_{en} and ν_{in}) as well as the plasma number density. The ion-neutral friction is more important because in the lower E-region of ionosphere, ν_{in} is much larger than ω_{ci} while ν_{en} is still smaller than ω_{ce}, such that the

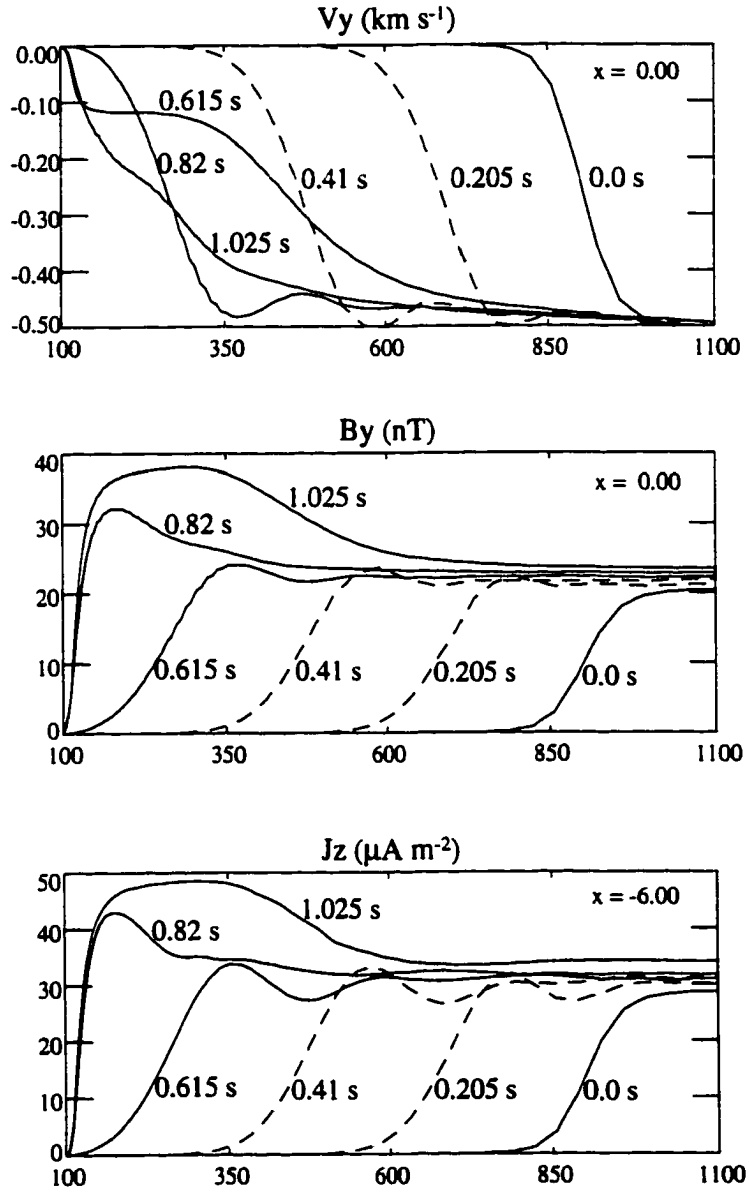

Figure 4.3: Simulation results of the time evolution of the Alfvén wave propagation and reflection in the ionosphere and the field-aligned current layer.

dominant term for large Pedersen conductivity is from the term of ion-neutral collision.

Figure 4.4 shows the formation of the field-aligned current layers. When the initial magnetic field shear perturbation propagates with Alfvén waves into the lower ionosphere along the magnetic field lines, two field-aligned current layers are built up. Both, the magnitudes of the magnetic field perturbation and the FAC are enhanced due to the Alfvén wave reflection. The magnetic field perturbation increases from its initial value of ± 22 nT to ± 32 nT , and the FAC density increases from ± 32 μA m^{-2} to ± 43 μA m^{-2}.

4.2.2 Density depletion

The FAC is closed by the Pedersen current in the lower E-region of the ionosphere. Since the FAC is mostly carried by electrons, while the Pedersen current is largely carried by ions, at the base of a field-aligned current layers where the FAC is connected to the closing Pedersen current, the plasma number density changes according to the pattern of the plasma motions. At the base of the upward field-aligned current layer the plasma number density increases as a result of the plasma's convergent flow, i.e., electrons moving downward and ions moving inward. On the other hand, at the base of the downward field-aligned current layer, the plasma number density decreases due to the plasma's divergent flow, i.e., electrons moving upward and ions moving outward. This mechanism implies that if the downward FAC layer can stay in the same location for a certain period of time, a number density hole will be generated at the base of the current layer.

Figure 4.5 shows a sketch of the downward FAC and the associated electron as well as ion motion. We can use the continuity equation to briefly estimate the decreasing rate of the plasma number density. The continuity of the current requires that $\nabla \cdot \mathbf{j} = e\nabla \cdot n(\mathbf{v}_i - \mathbf{v}_e) = 0$, but for electrons, $\nabla \cdot n\mathbf{v}_e \neq 0$ which, from the continuity equation, implies that $\frac{\partial n}{\partial t} \neq 0$.

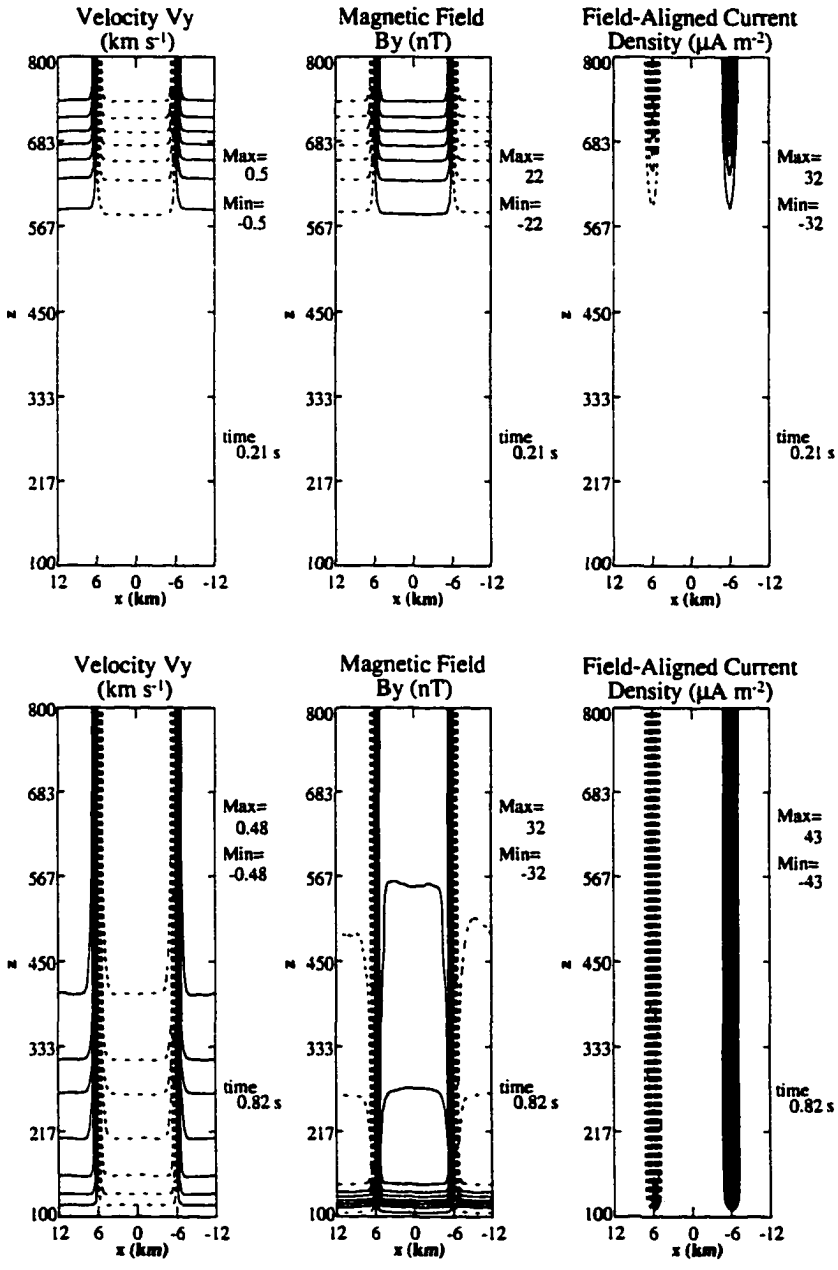

Figure 4.4: Contour plot of the Alfvén wave propagation and the field-aligned layer formation. Top plots show the perturbation of velocity (left), magnetic field(middle), and field-aligned current layers (right) at the early simulation time $t = 0.21$ s. The bottom plots show the same parameters at the time of 0.82 s.

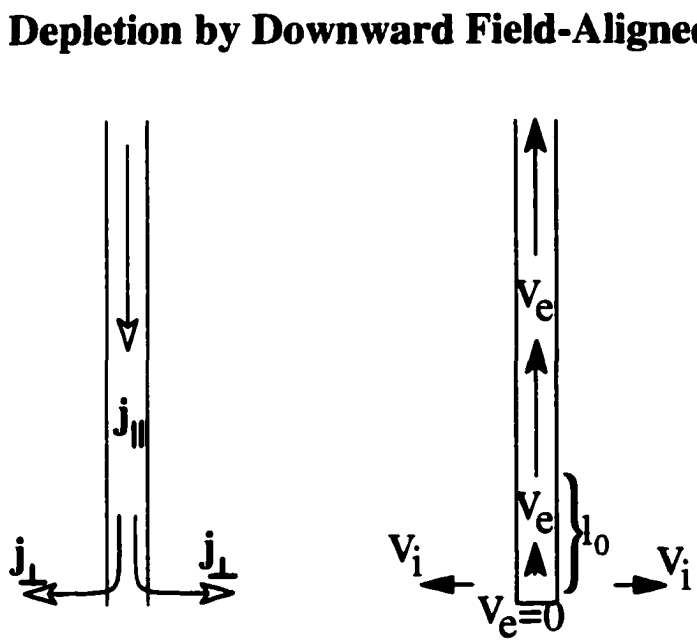

Figure 4.5: A sketch of the electron and ion motion in the downward field-aligned current layer. The divergent of both electron and ion at the base of the downward FAC layer generates a plasma density hole.

The continuity equation is given by:

$$\frac{\partial n}{\partial t} = -\nabla \cdot n\mathbf{v}_e \tag{4.5}$$

Inside the current layer, $\mathbf{j} \approx \mathbf{j}_{||} \approx -en\mathbf{v}_e$, so that we can rewrite the continuity equation as:

$$\frac{\partial n}{\partial t} = \frac{1}{e}\frac{\partial j_z}{\partial z} \tag{4.6}$$

This equation can be solved in the region with the gradient of the field-aligned current as:

$$n_e = n_{e0}(1 + \lambda t)$$

where, $\lambda \approx \frac{1}{e}\frac{\Delta}{l_0} \approx -\frac{|j_{||}|}{el_0}$, and l_0 is the distance from the base of the current layer where $\mathbf{v}_{e||} = 0$ (i.e. $\mathbf{j}_{||} = 0$) to the altitude that $\mathbf{j}_{||}$ reaches constant.

As a result of the plasma density irregularity associated with the field-aligned current layer, the original conductivity pattern in the lower E-region of the ionosphere in the vicinity area of the field-aligned current layer is changed. The conductivity increases (decreases) in time around the base of the upward (downward) FAC layer. Figure 4.6 shows the simulation result of this phenomena 8 seconds after the field-aligned current layers have reached the E-region. The top panel shows the FAC closed by the Pedersen current at the lower E-region and the ion as well as the electron flow pattern. We can see that the FAC is indeed carried by the electrons, and the closing Pedersen current is largely carried by the ions. The bottom panel shows the plasma number density irregularity and the Pedersen as well as Hall conductivities change due to the different patterns of the plasma motion associated with the FAC. We can see a density hole (peak) and minimum (maximum) conductivities at the base of the downward (upward) field-aligned current layer (at $x = 6$ km). Figure 4.7 shows the density variation with time at the different locations of the simulation box, i.e., inside the upward current layer at $x = -6$ km (top panel), outside the current layer at $x = 0$ km (middle panel), and inside the downward current layer at $x = 6$ km (bottom

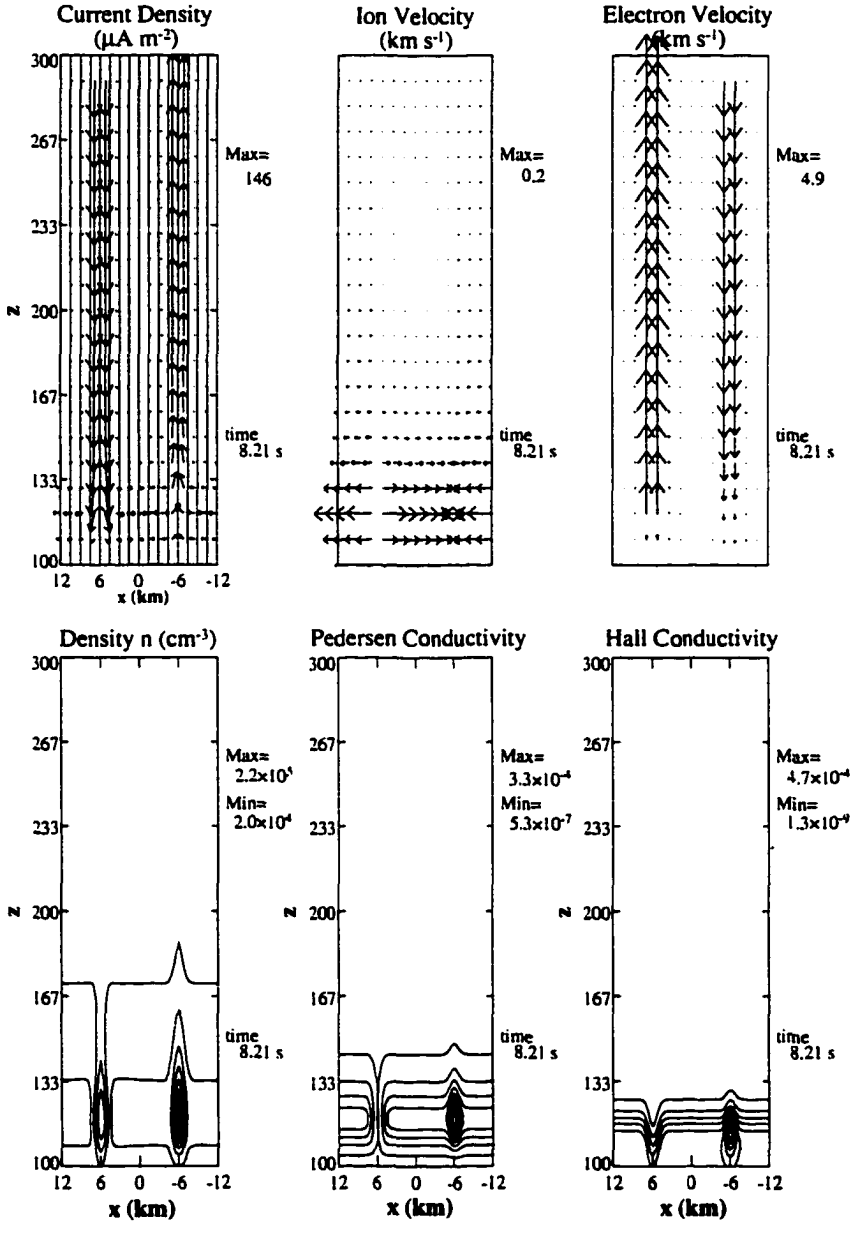

Figure 4.6: Simulation results of the FAC, the ion and electron motions related to the FAC layers in the ionosphere (top plots), density hole, and Pedersen as well as Hall conductivities (bottom plots).

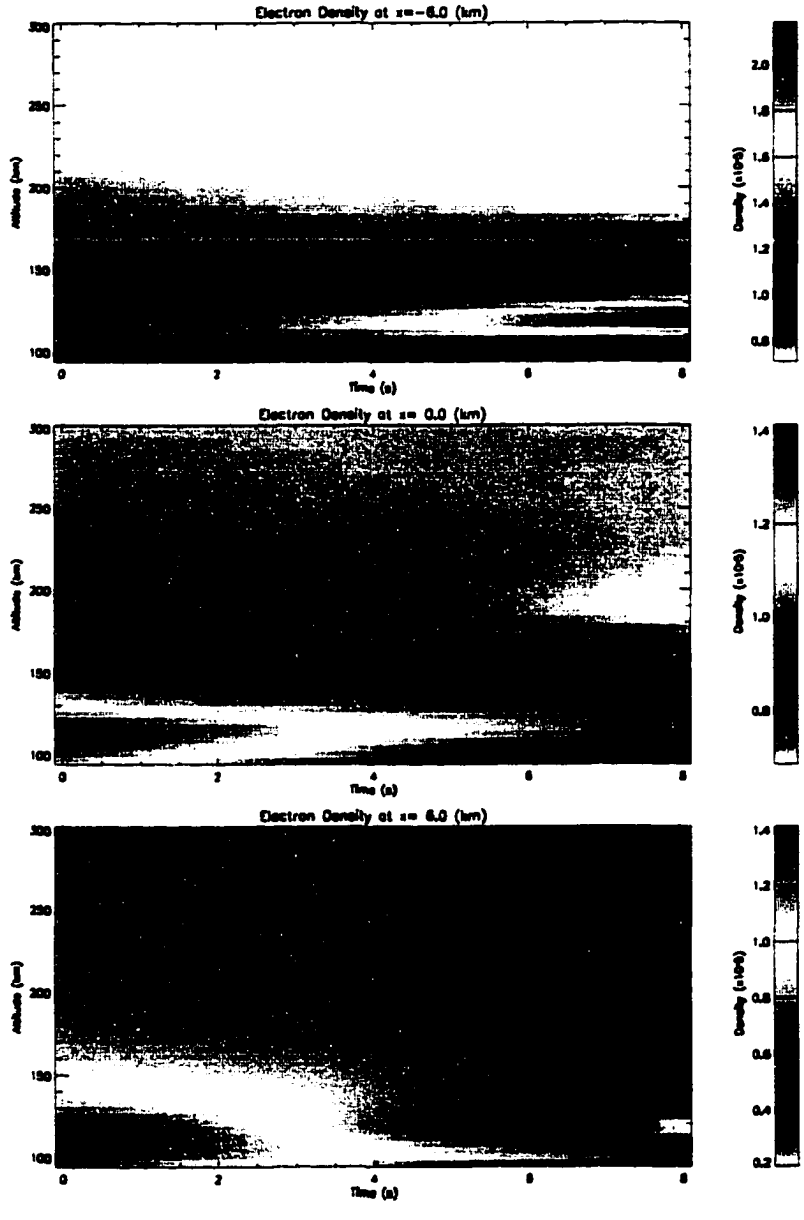

Figure 4.7: The plots of time evolution of the electron number density at the different locations: inside the the upward field-aligned current layer at $x = -6$ km (top), outside the current layers at $x = 0$ km (middle), and inside the the downward FAC layer at $x = 6$ km (bottom).

panel). Notice that beside the density change associated with the FAC, we see the density decreasing everywhere at the lower altitude due to the recombination processes. The time scale of the recombination is longer than that of the density hole formation by FAC.

4.2.3 Widening of the downward field-aligned current

Another interesting effect of the FAC is that the density hole at the base of the downward field-aligned current layer makes the current layer wider. Figure 4.8 shows the plots of plasma number density, Pedersen conductivity, and Hall conductivity along a horizontal cut at the altitude of 120 km where we find the closing Pedersen current, at the times of 1.0 and 8.2 seconds. We see that after 8 seconds, due to the plasma density change, the Pedersen conductivity at the location of upward FAC increases from about 2×10^{-4} to about 3.5×10^{-4} mho/m . But in the region of downward FAC layer, Pedersen conductivity strongly decreases to 3×10^{-5} mho/m. With such a small Pedersen conductivity, Pedersen current cannot close at the center area of the density hole, and a large part of the field-aligned current connects to the Pedersen current at the edge of the hole where the Pedersen conductivity is large enough (Figure 4.6). This change in conductivity widens the downward FAC layer. The decreasing of the plasma number density, and Pedersen and Hall conductivities outside the current layers is due to the fast recombination processes in the lower ionosphere. Figure 4.9 shows contour plots of the three components of the current density at times 1.0 and 8.2 seconds. We see that the downward field-aligned layer after 8 seconds is much wider than that at the early time and significantly wider than the upward FAC layer. One interesting thing is that although the density hole is only localized at the lower E-region of the ionosphere, the widening effect of the downward FAC layer is through out the entire current layer. This shows one aspect of the important role that the lower E-region of ionosphere plays in regulating the field-aligned current. The increase of the current density magnitude is due

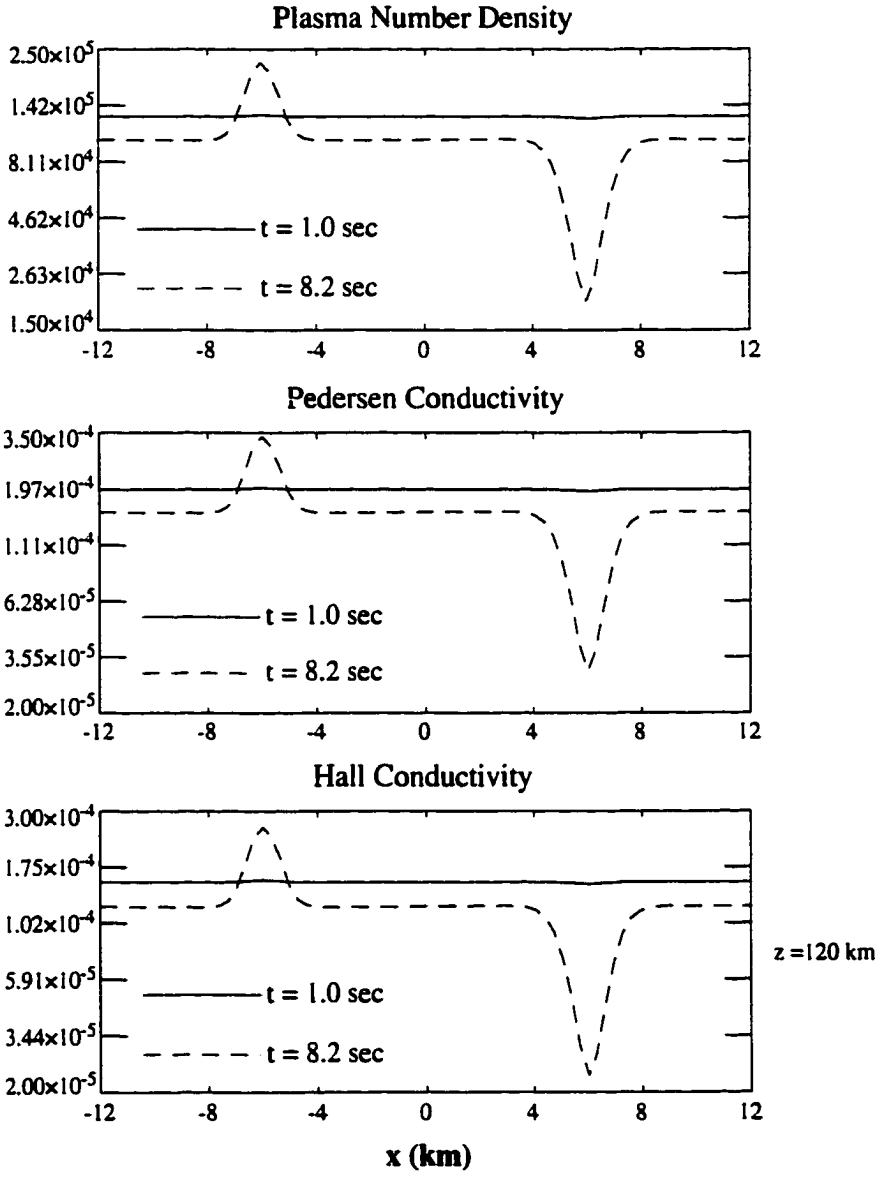

Figure 4.8: The change of plasma number density (top), the Pedersen (middle) and Hall (bottom) conductivities between from the early time $t = 1.0$ s (solid lines) to the time of $t = 8.2$ s (dash lines) at the altitude of $z = 120$ km .

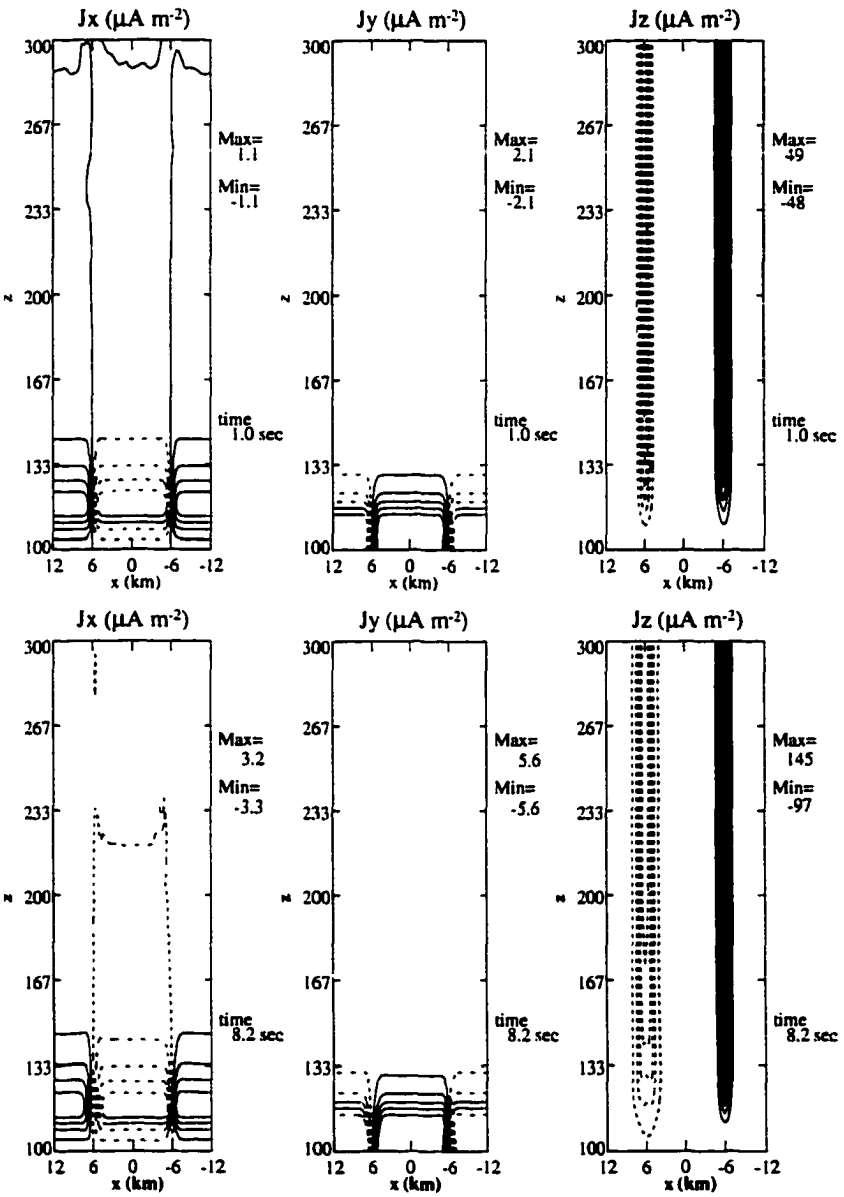

Figure 4.9: The ionospheric current at time $t = 1.0$ s (top) and $t = 8.2$ s (bottom), and the widening of the downward FAC layer.

to the Alfvén wave reflection.

4.2.4 Finite field-aligned current filament

Ellis and Southwood [1983] pointed out that in appropriate circumstances an Alfvén wave incident on an ionosphere with a steep horizontal gradient in conductivity can give rise to sheets of FAC set up on the edge of the ionospheric region of enhanced conductivity. They obtained their results by using the height integrated Pedersen conductivity, a constant electric field, and treating the ionosphere as a boundary. However, in a realistic environment the electric field varies with altitude, with the horizontal direction, and with time. I investigated this phenomenon in detail with the full dynamics and an altitude resolved ionosphere by adding a localized soft particle precipitation in the region around the upward FAC layer.

The initial configuration and perturbation is set the same as the FAC simulation I described above. But in this computer experiment, a particle precipitation with a characteristic energy of 500 eV and an energy flux of 80 mW m^{-2} is added in the region between $x = -2$ km and $x = -10$ km. The upward field-aligned current layer is located at $x = -6$ km. Figure 4.10 shows the altitude profile of the ionization rate for this precipitation. This precipitation yields a maximum plasma number density at the altitude of about 160 km. The precipitation process is parameterized by using input from an ionospheric transport computation (Lummerzheim [1992]).

Figure 4.11 shows the vector plot of the current density of the simulation results at time 6.15 second. It shows (top panel) that a downward field-aligned current filament is generated at the sharp edges of the particle precipitation ($x = -2$ km and $x = -10$ km) where the Pedersen conductivity has a strong gradient due to the large difference of the plasma number density between the two sides. The interesting fact is that this field-aligned current filament does not go down to the lower E-region of the ionosphere (120

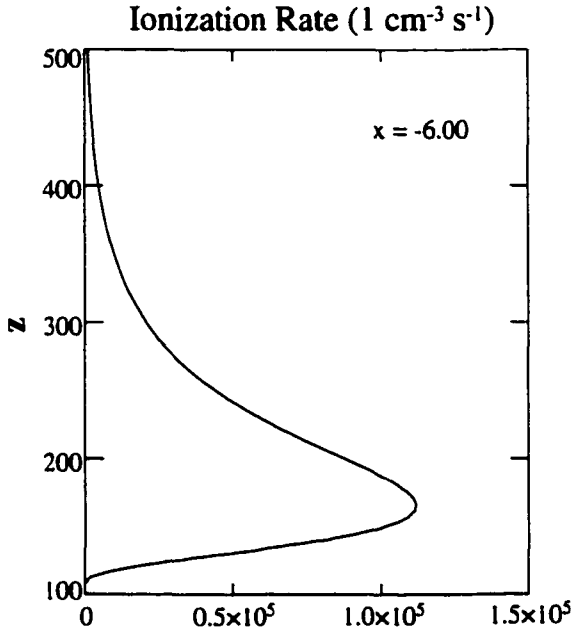

Figure 4.10: Ionization profile with the characteristic energy of 500 eV and the energy flux of 80 mW m^{-2}.

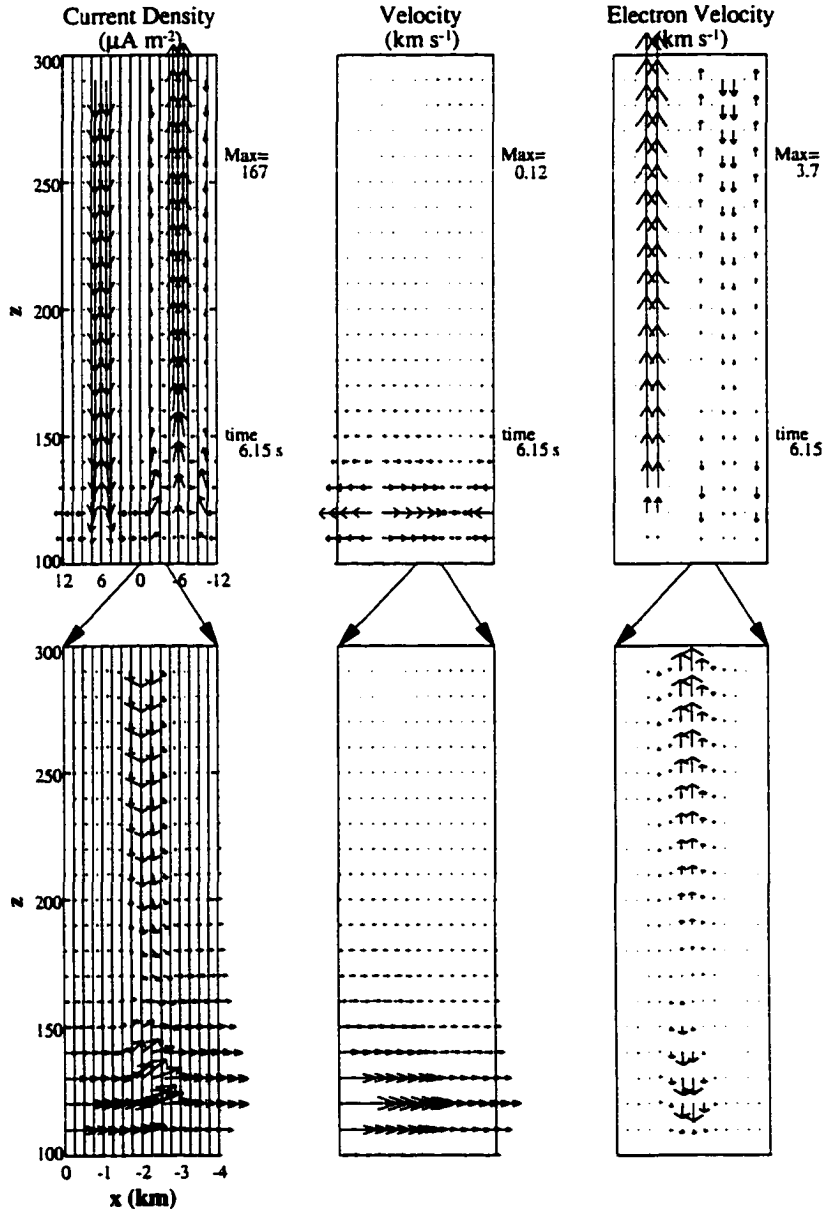

Figure 4.11: Finite FAC filament at the sharp edge of the particle precipitation boundary and the ion as well as electron motion. The bottom panel shows the amplified structure.

km) like the usual FAC does. It stops at an altitude of about 160 km, where the plasma number density in the region of precipitation reaches a maximum, and from there connects to the main upward field-aligned current through the Pedersen current. Below 160 km, on the other hand, we see an upward field-aligned current filament at the edges of the particle precipitation region. The bottom panel of Figure 4.11 shows magnified plots of the adjacent region of the field-aligned current filament (i.e. between $x = -4$ km and $x = 0$ km).

The physical mechanism of the field-aligned current filament at the steep edge of the precipitation region can be illustrated by the differences of the Alfvén wave reflection on the two sides. The Alfvén wave reflection in the ionosphere depends strongly on the Pedersen conductivity (i.e. the friction between ions and neutrals plays an important role). In the region of electron precipitation, the plasma number density in the lower ionosphere is much larger than outside, such that the Pedersen conductivity is greatly enhanced in the E and F-region of the ionosphere inside the precipitating area, which yields more efficient reflection of Alfvén waves. As time proceeds, the increase of the plasma number density due to the precipitation (with a maximum at 160 km) extends the large Pedersen conductivity region to higher altitudes such that the Alfvén wave in the precipitating region is reflected at higher altitudes. Figure 4.12 shows contour plots of the plasma number density, and Pedersen and Hall conductivities in the ionosphere. The difference of the Alfvén wave reflection on the two sides of the edge of the precipitation generates an additional velocity as well as magnetic field shear which introduces the field-aligned current filaments right at the edge of the precipitation.

At altitudes above 160 km, more of the Alfvén wave is reflected inside the precipitating region, where the Pedersen conductivity is higher, than outside. Since the reflection of Alfvén waves increases the magnetic field perturbation (Zhu *et al.* [1999]), it follows that the magnetic field perturbation inside the precipitating region is larger than that outside

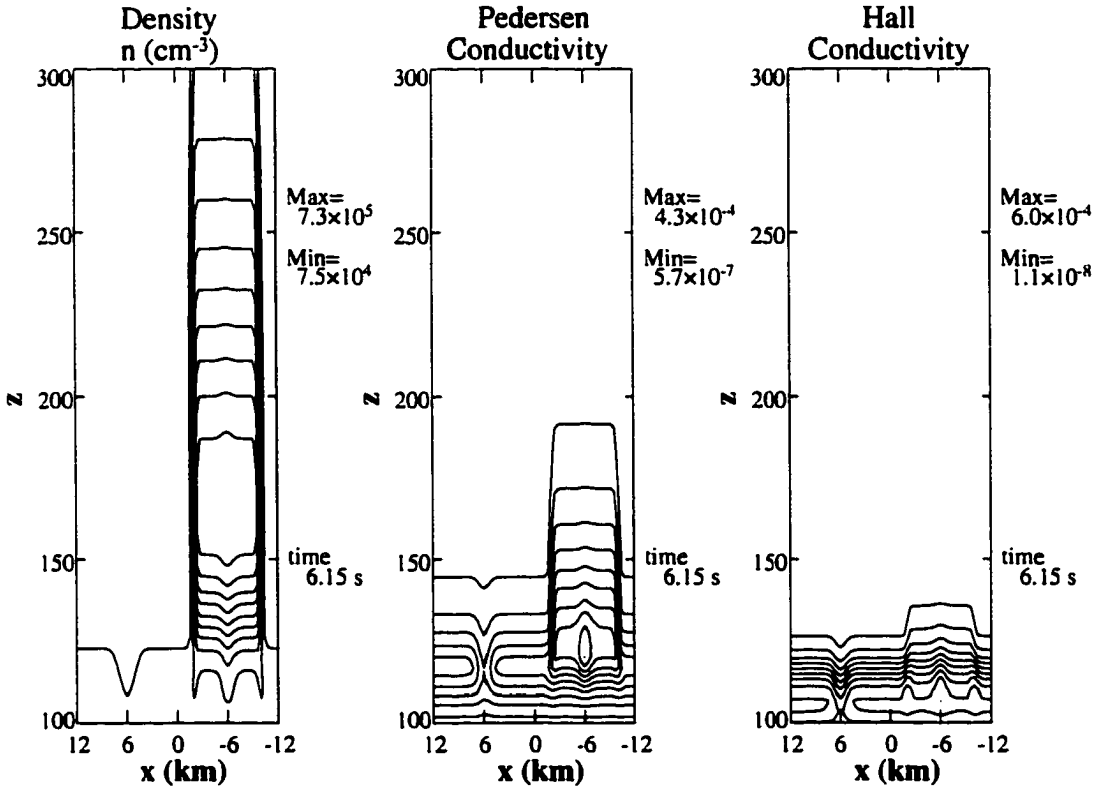

Figure 4.12: Contour plots of the plasma number density (left), Pedersen (middle) and Hall (right) conductivities in the simulation of the field-aligned current with particle precipitation in teh vicinity of the upward FAC layer.

and a magnetic field shear is formed at the edge of the precipitation region. The top panel of Figure 4.13 shows the magnetic field perturbation at the altitude of 250 km. We see the shear (gradient) of the magnetic field at the edge of the precipitation region (i.e. $x = -2$ km and $x = -10$ km) with the larger value inside the precipitation region. These magnetic field shears are equivalent to two downward field-aligned current filaments.

On the other hand, at the altitudes below 160 km, since less of the Alfvén waves penetrate to this altitude inside the region of precipitation than outside, a shear of magnetic field perturbation in the opposite direction is formed at the edge of the precipitation region. So at these lower altitudes, an upward field-aligned current filament is formed at the edge of the precipitation region. The bottom panel of Figure 4.13 shows the magnetic field perturbation at the altitude of 132 km.

The lower portion of the upward field-aligned current filament can be also explained from the point of view of the enhancement of Pedersen conductivity inside the precipitation region. Since the large Pedersen conductivity inside the precipitation region extends up to higher altitudes, the corresponding Pedersen current which closes the field-aligned current also extends to higher altitudes. The continuity of current require that part of the Pedersen current outside the precipitation region at the lower altitudes has to go up to connect with the high altitudes Pedersen current inside the precipitation region (Figure 4.11).

4.3 Summary and discussion

In this chapter, I have presented some new, interesting and important results of the field-aligned currents and their effect in the ionosphere. These results indicate that the ionosphere is not just a passive recipient of the magnetospheric dynamics. It can play a very important or even a crucial role in the ionosphere-magnetosphere coupling system.

Field-aligned current layers are formed when sheared magnetic field perturbations in the

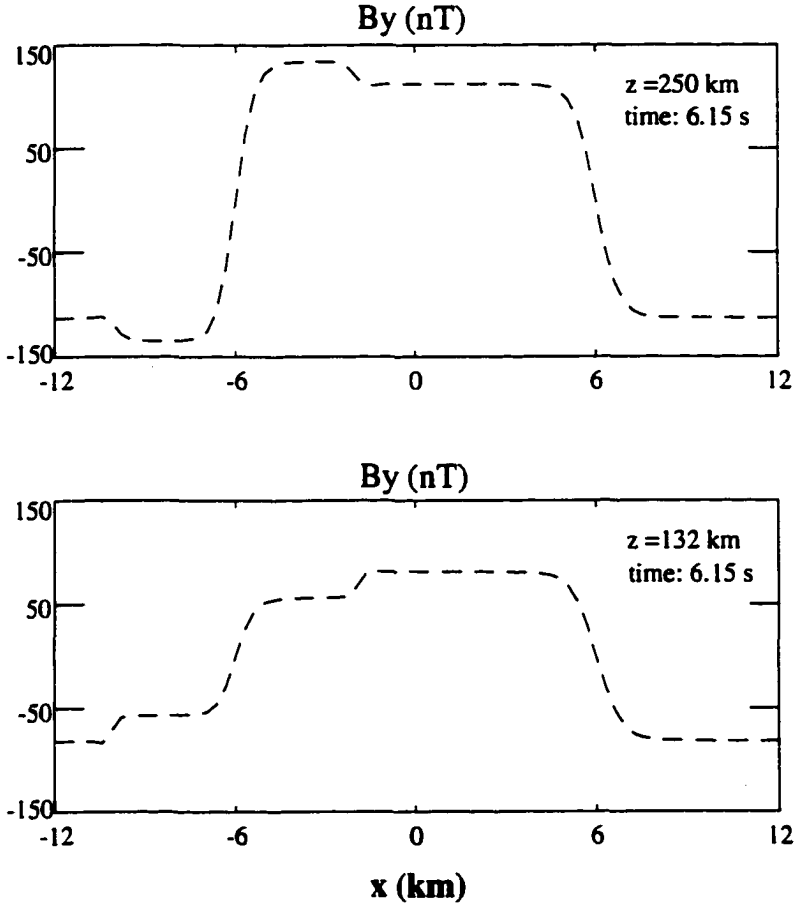

Figure 4.13: Magnetic field perturbation at the altitude of 250 km and 132 km at the time of 6.15 s in the simulation of the FAC with particle precipitation in the vicinity of the upward field-aligned current layer. The magnetic shear is in the opposite direction at these two altitudes at the edges of the particle precipitation boundaries.

magnetosphere propagate along the magnetic field lines (carried by Alfvén waves) down to the ionosphere. Due to the high ion-neutral collision frequency in the lower ionosphere, the field-aligned currents are closed by the so called ionospheric Pedersen current in the lower E-region (around 120 km). The field-aligned currents are mostly carried by the electrons, while the closing Pedersen current is carried mainly by the ions.

Irregularities of the plasma number density and the associated ionospheric conductivities are found at the altitudes of the closing Pedersen current (lower E-region) as a result of the different plasma motion in the upward and downward field-aligned current layers. In the upward field-aligned current layer, the electrons move downward to the lower E-region of the ionosphere, while the ions that carry the Pedersen current, by the continuity law of the current, move towards the base of the upward field-aligned current layer, so that the plasma number density increases at the base of the upward field-aligned current layer due to the convergent motion of both the electron and ion particles. On the other hand, a plasma depletion is generated at the base of the downward field-aligned current layer because of divergent electron and ion motion. Consequently, the irregularity of the plasma number density changes the distribution of the Pedersen and Hall conductivities in the ionosphere.

The very low Pedersen conductivity at the base of the downward field-aligned current layer, due to the plasma density depletion, stops the closing Pedersen current from going into the central area of the downward field-aligned current layer. Hence as the density hole is getting deeper and larger, the downward field-aligned current layer is becoming wider.

The change of the conductivities in the ionosphere can strongly affect the ionospheric currents. The simulation of the FAC with particle precipitation added in the vicinity of the upward field-aligned current layer showed a very interesting result, i.e., the finite field-aligned current filament generated at the edge of the sharp particle precipitation boundary. This field-aligned current filament is not like the regular FAC that extends all the way

down to the lower E-region of the ionosphere. It stops at a certain altitude depending on the characteristic parameters of the precipitation (about 160 km in this simulation) and connects to the main field-aligned current. The cause for this field-aligned current filament is the difference in the Alfvén wave reflection across the boundary, because of the different plasma number density as a result of the particle precipitation. Moreover, at the altitudes below this field-aligned filament, another field-aligned current filament in the opposite direction is formed due to the different Pedersen conductivities on the two sides of the precipitation boundary.

Chapter 5

Tall Auroral Red Ray

A longstanding unresolved problem of auroral physics has been the formation of tall red rays in the ionosphere (Størmer [1955]). The formation of these rays requires the resolution of two problems: what causes the spatial structure and what is the energy source. Tall rays appear as luminous pencil-like beams that, if sufficiently bright, are usually red, the signature of the $O(^3P\text{-}^1D)$ transition. The excitation threshold of $O(^1D)$ is 1.96 eV, and at these high altitudes the excitation is caused primarily by collisions between ground state O atoms and electrons.

To be visible to the naked eye the rays require a luminosity of more than 5 kR. Assuming a line of sight thickness of 10 km, a luminosity of 5 kR ($= 5 \cdot 10^9$ photons cm^{-2} s^{-1}) in a steady state corresponds to an energy production rate inside the tube of about 10^4 eV cm^{-3} s^{-1}, corresponding to an energy deposition rate of about 0.1 eV per electron per second for an electron density of 10^5 cm^{-3}.

In the non-sunlit atmosphere rays can extend as high as 600 km (Størmer [1955]) where the atomic oxygen density, even during solar max conditions, is less than about 10^8 cm^{-3}. One of the challenging problems is their relatively constant luminosity over a large altitude

range compared to the neutral oxygen scale height.

In this chapter I examine the ohmic heating in field-aligned current sheets as the energy source for tall rays. The only dissipation mechanisms considered are classical collisions, i.e., Coulomb and electron/ion neutral collisions. Since only classical collisions are invoked, derived heating and energy deposition rates represent a minimum and may be higher if turbulent processes contribute to the energization. Strong field-aligned currents are naturally confined to small spatial regions or thin sheets, and are thus consistent with the limited horizontal size of tall rays. However, here I do not address the three-dimensional localization, which requires a 3D model.

5.1 Outline of the simulation

The results presented were obtained with a two-dimensional simulation model (Zhu *et al.* [1999]) which was introduced in the previous chapter. The simulation is initiated by specifying a two-dimensional Alfvénic perturbation only at the upper boundary, from which point onward the self-consistent evolution of ionospheric structure and properties is computed. The perturbation carries two field-aligned current layers into the ionosphere. The wave is partially reflected in the lower ionosphere and creates a downward and an upward field-aligned current. For most of the presented results I refer to a case where the current density in the upward field-aligned current reaches about 600 μAm^{-2} after 4 seconds and is then kept approximately constant at a value of 600 to 650 μAm^{-2}. The downward current assumes an asymptotic value of about 500 μAm^{-2}. For comparison I have included two cases where the current densities have been reduced by 2/3 and 1/3, respectively, of these magnitudes. For the 3 cases the current densities and electron temperatures in the center of the upward current are plotted in Figure 5.1 as functions of altitude 8 seconds into the simulation.

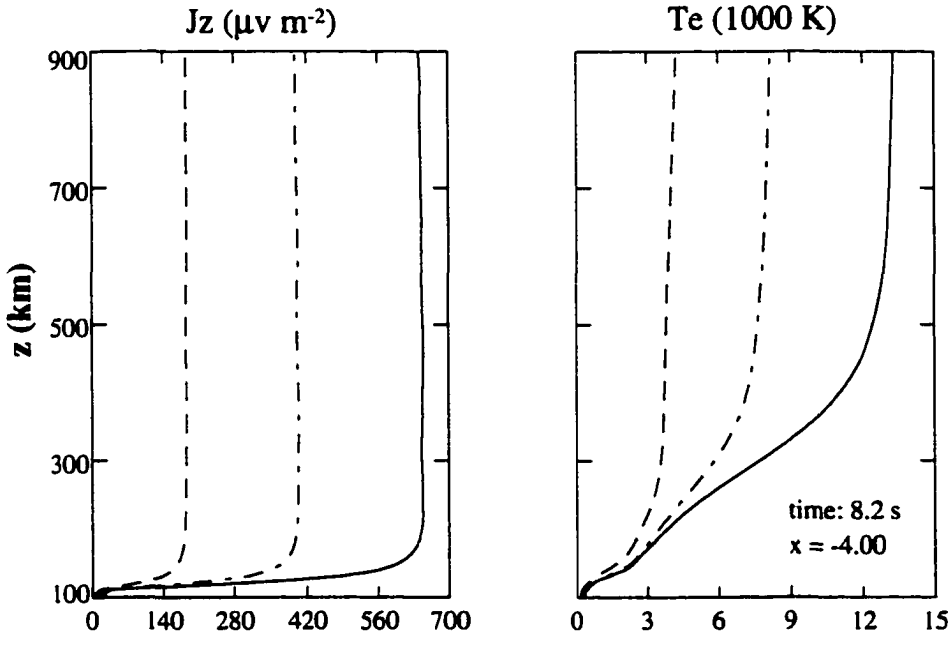

Figure 5.1: Current density (left) and electron temperature (right) profiles in the center of the upward current layer 8 seconds into the simulation for the reference case (solid), a 2/3 perturbation amplitude (dash-dotted), and 1/3 perturbation amplitude (dashed).

I have considered whether runaway electrons can alter the fluid model results. Kinetic simulations indicate that this is negligible for the considered parameters. To produce runaway, the electric force on an electron must be stronger than the frictional force due to Coulomb (and electron-neutral) collisions with the ambient plasma (and neutrals). To illustrate this, consider only electron-electron collisions, and let a single test electron collide with a thermal (Maxwellian) electron background. Furthermore, assume that the test electron has a kinetic energy, E_k, which is much higher than the thermal energy, kT, of the background electrons (where k is Boltzmann's constant), so that the thermal motion of the background may be ignored. Then the *critical* electric field, needed to overcome the frictional force, is

$$E_c = \frac{1}{4\pi}\frac{e^3}{\epsilon_0^2}\ln\Lambda\frac{n}{E_k}. \tag{5.1}$$

where SI units are used, e is the elementary charge, ϵ_0 the permitivity of vacuum, $\ln\Lambda$ the Coulomb logarithm (accounting for Debye screening), and n the (background) electron density. Using typical parameters $\ln\Lambda = 15$, $n = 10^5$ cm^{-3}, and $E_k = 1$ eV we get $E_c \approx 4 \times 10^{-5}$ V/m. By comparison, typical F-region electric fields, from Ohm's law, are of order 10^{-6}V/m with the current densities used in our calculation. Thus even in the energetic part of the electron population, the electric field needed to cause runaway is about 10 times stronger than the actual electric field. A fluid model should therefore be adequate to compute the O(^{1}D) excitation rate.

5.2 Heating and energy balance

The cross section for the O(^{1}D) excitation starts at about 2 eV and becomes large at about 3 eV. Thus a significant excitation of this state occurs only if there is a large number of electrons at these energies. In order to produce visible rays the energization of electrons

has to be maintained at a rate of several 0.1 eV s^{-1} per electron at altitudes from 200 to 500 km to pump oxygen into the excited state.

Figure 5.2 shows the electron temperature profile with altitude for the largest current density case in the up- and downward current regions for different times. While the initial temperature increase is similar in the two current layers the final temperature is significantly larger in the upward current. A second striking difference is the larger temperature gradient between 150 and 400 km altitude in the upward current compared to the downward current. The overall lower temperature in the downward current is partially caused by an increase of the E-region density at the base of the field-aligned currents (Zhu *et al.* [1999]). However, the different gradient in the temperature is generated also by a significant contribution from heat advection in the fast (60 km s^{-1}) drifting electron fluid in the current as illustrated by the results of Figure 5.3. The figure shows all electron energy source and loss terms as a function of altitude for the results of Figure 5.2. The dominant source is ohmic heating (solid line). However, there is a significant contribution from heat advection due to the temperature gradient and the fast electron drift which is positive in the upward and negative in the downward current layer. In the altitude range from 300 to 400 km this contributes 0.3 to 0.4 eV s^{-1}, almost half of the energy which is locally deposited. In the downward current the advective term is negative.

In the upward current the $O(^1D)$ excitation maximizes at about 350 km altitude and becomes the dominant loss mechanism at this altitude and above. The $O(^1D)$ excitation is also significantly larger in the upward than in the downward current due to the larger temperature in the upward current layer.

The fairly steady temperature profile at lower altitudes is caused by increasing collision frequencies with decreasing altitude. They imply a shorter charcteristic time scale at lower altitudes for the relaxation to a steady temperature. Here source and loss terms are reason-

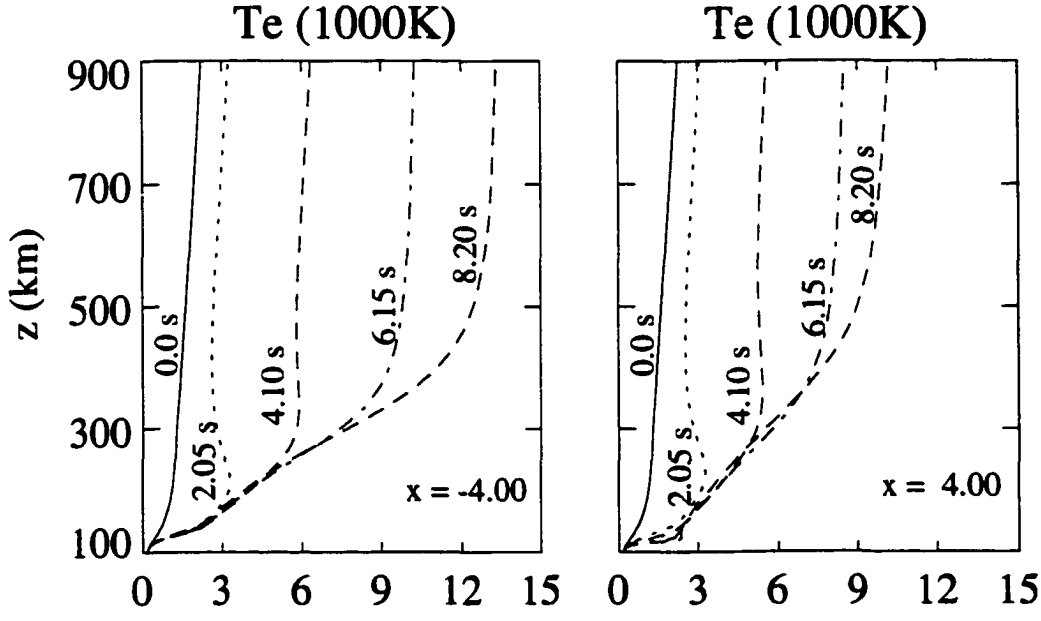

Figure 5.2: Electron temperature profiles for the reference case at increasing times in the center of the upward (left) and downward current (right).

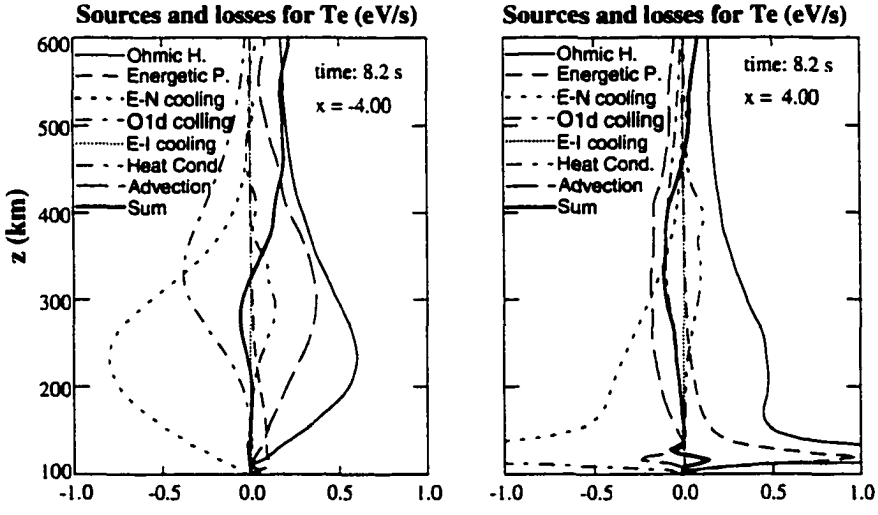

Figure 5.3: Source and loss terms in the electron energy at $t = 8$ seconds for the up- (left) and downward (right) currents. Shown are: the sum (heavy solid), ohmic heating (solid), advection (long dashes), heat conduction (dash double dotted), precipitation with characteristic energy 1.5 keV and a flux of 10 mW m^{-2} (medium dashes), cooling by Coulomb collision (dotted), cooling by $O(^1D)$ excitation (dash-dotted), and all other electron-neutral cooling terms (short dashes).

ably balanced after 8 seconds. The temperature obviously has not reached a steady state in the upward current above 400 km altitude.

The energetic electron precipitation is included in the simulation only to maintain the plasma density by ionization at E-region altitudes. This term, loss by Coulomb collisions, and heat conduction are of minor importance for the altitude range and time scale of interest.

Using the derived excitation rates (Rees and Roble [1986]), Figure 5.4 illustrates the luminosity for steady state emission conditions. Note that the half life of the $O(^1D)$ state is about 100 seconds. Thus heating for about 10 seconds yields roughly 10% of the luminosity shown in Figure 5.4. Similarly twice the column thickness gives twice the luminosity. Figure 5.5 shows the luminosity for steady state emission conditions for the large field-aligned current layer case in contour plots.

Over the altitude range from 250 km to about 450 km the emission rate stays above 50% of its maximum value, consistent with the altitude range for tall auroral rays which is much larger than for ordinary aurora. The decrease of neutral density in this altitude range is in part compensated by the increasing electron temperature. The rapid increase of the luminosity from 150 to 250 km is caused by the increase in temperature and quenching of the emission at lower altitudes. The decrease at high altitudes is caused by the exponential decrease of the neutral density and to a lesser extent by the decrease of the electron density. The excitation rate and the luminosity in the downward current (right plot in Figure 5.4) is smaller by a factor of 5.

For comparison the thin dotted line in Figure 5.4 (left) illustrates the luminosity from precipitation with a low characteristic energy (250 eV) and an energy flux of 40 mW m^{-2}. The result demonstrates that much higher precipitating energy fluxes are necessary to obtain a similar magnitude for the luminosity. The altitude range of the luminosity caused by

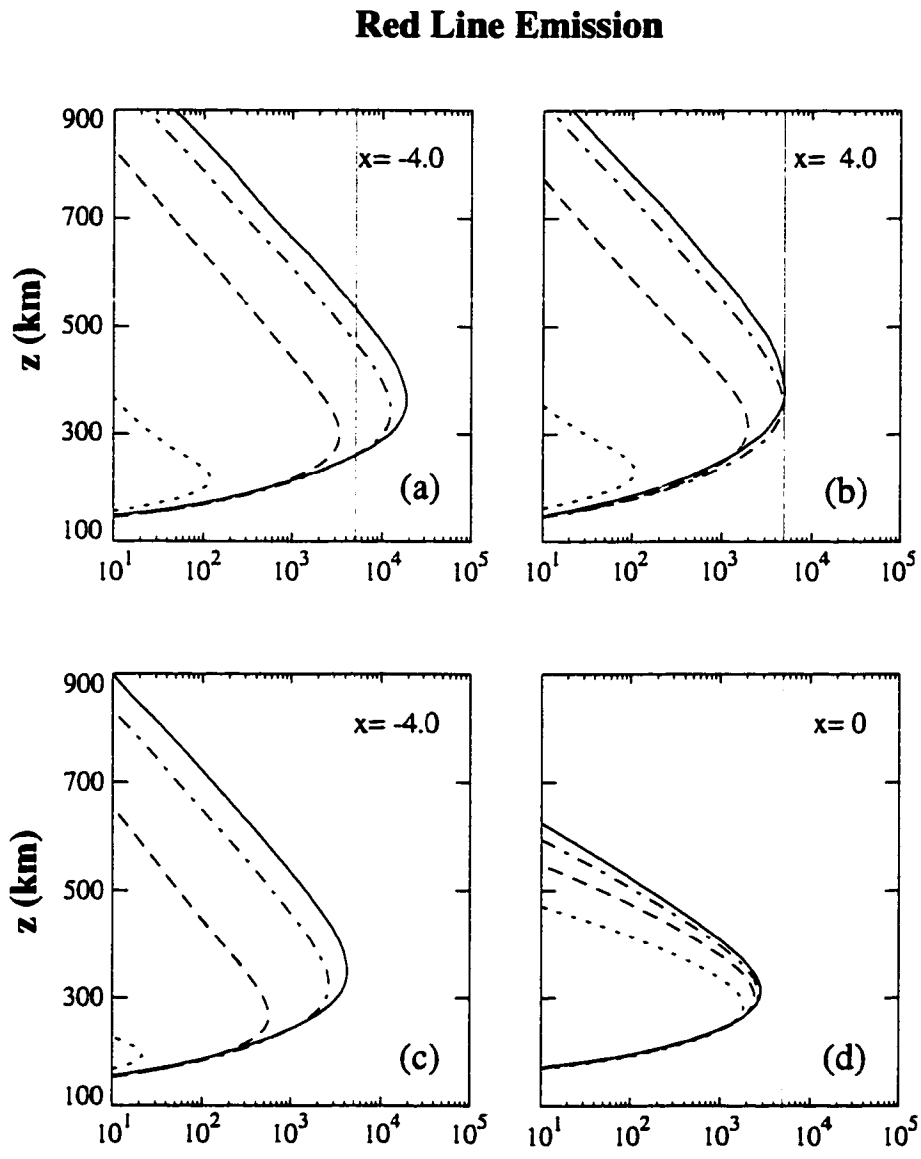

Figure 5.4: Redline emission in Rayleighs assuming steady emission conditions and a column width of 10 km for different cases. Dotted and dashed lines with increasing maximum luminosity correspond to 2, 4 and 6 seconds and the solid line to 8.2 seconds. Plots (a) and (b) are in the center of the upward and downward large field-aligned current (650 μA m^{-2}) layers. Plot (c) is in the center of a smaller upward current layer (400 μA m^{-2}). Plot (d) represents the luminosity from a precipitation of 40 mW m^{-2} with a low characteristic energy of 250 eV. The red vertical line indicates the 5 kR threshold for visible brightness.

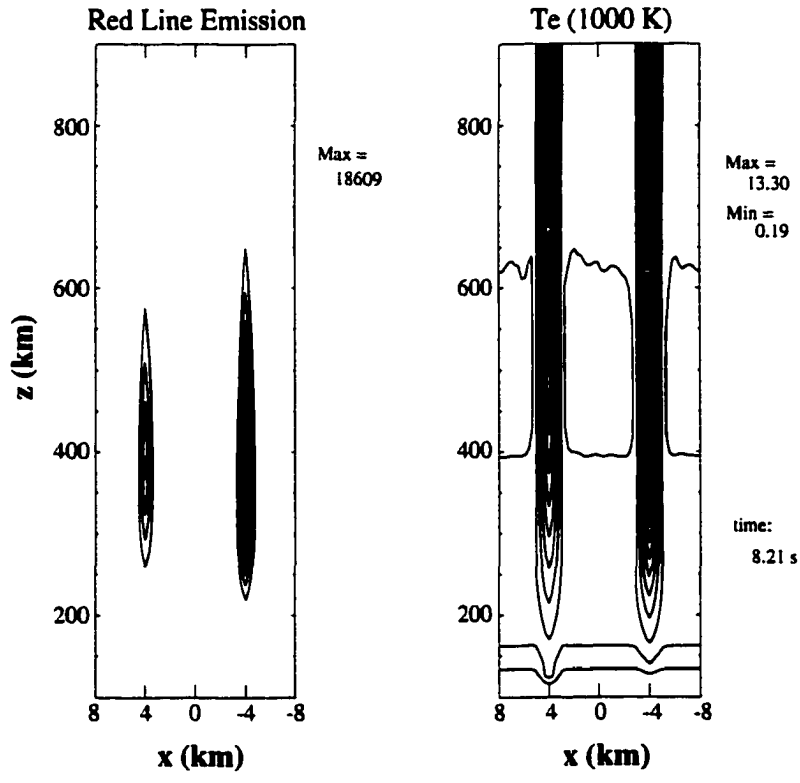

Figure 5.5: Contour plots of auroral red line emission (left) assuming a steady emission conditions and a column of 10 km and the electron temperature (right) in the simulation of large field-aligned current (about 650 μA m^{-2}) layers.

precipitation is narrower.

5.3 Summary and discussion

The results presented in this chapter demonstrate the efficiency of local energy deposition (in the upper F region ionosphere) by ohmic heating in field-aligned current layers. The energy deposition rate can be several 0.1 eVs^{-1} per electron for current densities of several 100 μAm^{-2}.

For tall red auroral rays a high oxygen density is necessary to deposit the available energy in the $O(^1D)$ state. I used a hot neutral atmosphere (T_{exo} = 1300 K) to provide sufficient density at high altitude. This is consistent with Størmer's observation that these rays occur during solar maximum conditions. For our brightness estimates we used conservative values by requiring sufficient excitation to produce visible brightness from a 5-10 km long slant path through the ray. Størmer detected many of the tall red rays only after he started to use a particularly red sensitive film, indicating that tall rays are often sub-visual. Our results show that the brightest tall rays require that the oxygen is exposed to the heated electron gas for several tens of seconds.

Our model does not require that the high field-aligned current densities remain in exactly the same location for this time. Large field-aligned current densities are indicated by various observations (e.g., Stasiewicz *et al.* [1998]; Lanchester *et al.* [1997]), but such currents would have a rather small width (few 100 m to 1 km) and move on average with considerable velocity (1 km s^{-1}) such that plasma is typically only exposed for a fraction of a second to the ohmic heating. Repeated exposure of a column of oxygen for sufficient time will have an integrating effect because of the long radiative lifetime of $O(^1D)$ of 100 s. The motion of the current layers need not be uniform and parts may stay in one location for a considerable time, folds may develop, or multiple current layers may intersect the same volume of the

thermosphere at different times, and thus contribute to the ray-like appearance of the resulting aurora. This structural aspect of rays requires a three-dimensional model. Note that after sufficient pumping the red-line emission is from the decay of the excited neutral oxgyen and therefore is basically motionless compared to ordinary discrete aurora.

A main limiting factor for the energy deposition is the Coulomb collision cross section. The deposition decreases strongly with increasing temperature. This is expected to change if turbulent plasma processes driven by large electron drifts play a role. I note that the high current density and the considered initial plasma properties do not satisfy the onset condition for ion acoustic turbulence. The final states, however, with high electron temperatures, are ion acoustic unstable. Turbulent processes can enhance the effective collision frequencies vastly, thereby causing much higher energization rates (e.g. Sagdeev and Galeev [1969]; Papadopoulos [1977]; Treumann and Baumjohann [1997]). Here I intended to determine the electron energization in field-aligned currents based on well established classical collisions. They demonstrate that Coulomb collisions alone can increase the electron temperature to well above 10,000 K in narrow regions within a few seconds.

The $O(^1D)$ excitation rate decreases exponentially with decreasing electron temperature and is proportional to oxygen and electron number density. However, for very large electron number densities, the energy deposition per particle is lower, implying lower temperatures. For low electron number densities the obtained temperatures are higher, but limited due to the Coulomb cross section, such that the flux of sufficiently energetic electrons decreases with decreasing number density. The total $O(^1D)$ excitation maximizes for electron number densities of about 10^5 cm^{-3}.

Chapter 6

Ionospheric Conductivies

Ionosphere conductivities are very important in the study of the coupling between ionosphere and magnetosphere. As we have seen in chapter 4, the change of conductivities in the ionosphere strongly affects the current flows in the ionosphere and can even generate new field-aligned current filaments at boundaries where the Pedersen conductivity has a strong gradient. Using ionospheric conductivities, we can express the current in the ionosphere as:

$$\mathbf{j} = \sigma \cdot \mathbf{E} \tag{6.1}$$

where

$$\sigma = \begin{pmatrix} \sigma_P & -\sigma_H & 0 \\ \sigma_H & \sigma_P & 0 \\ 0 & 0 & \sigma_0 \end{pmatrix} \tag{6.2}$$

The three conductivity parameters σ_P, σ_H and σ_0 are called Pedersen, Hall and parallel conductivities, respectively. Here, we are interested only in the Pedersen and Hall conductivities which are associated with the horizontal components of the electric field and the current.

In this chapter, I will first briefly go through the derivation of the commonly used Pedersen and Hall conductivities. After the introduction of the basic idea of the ionospheric conductivities, more discussion will be focused on the height integrated ionospheric current. The height integrated ionospheric current calculated from the real simulation current (i.e. $\mathbf{j} = \nabla \times \mathbf{B}$) is compared to the current computed from the ionospheric electric field and the height integrated Pedersen and Hall conductivities. Finally, the effect of the electron pressure gradient on the height integrated ionospheric current is also discussed. Before looking at these conductivities, I would like first to take a look at the ionospheric electric field (i.e., contributions from different terms in the generalized Ohm's law).

6.1 The electric field in the ionosphere

The generalized Ohm's law in the lower ionosphere is obtained from the electron momentum equation by ignoring the inertia term:

$$0 = -\nabla p_e - ne(\mathbf{E} + \mathbf{v}_e \times \mathbf{B}) - nm_e\nu_{en}\mathbf{v}_e - nm_e\nu_{ei}(\mathbf{v}_e - \mathbf{v}_i) \tag{6.3}$$

Here, for simplicity, the neutral velocity is assumed to be 0. We can rewrite this equation as:

$$\mathbf{E} = -\frac{1}{ne}\nabla p_e + \mathbf{v}_e \times \mathbf{B} + \eta\mathbf{j} - \frac{m_e\nu_{en}}{e}\mathbf{v}_i \tag{6.4}$$

Where $\mathbf{j} = ne(\mathbf{v}_i - \mathbf{v}_e)$, and $\eta = \frac{m_e}{ne^2}(\nu_{en} + \nu_{ei})$ is the resistivity with ν_{en} and ν_{ei} the electron-neutral and electron-ion collision frequencies, respectively. These four terms contribute to the electric field. Although the electron-neutral collision frequency in the lower ionosphere could be very high (above 10^4 s^{-1}), it is still much smaller than the electron's gyro-frequency (about 10^6 s^{-1}). So the $\mathbf{v}_e \times \mathbf{B}$ term is dominant over the collisional terms $\eta\mathbf{j}$ and $\frac{m_e\nu_{en}}{e}\mathbf{v}_i$. The remaining question is whether the electron pressure gradient term is also negligible.

Figure 6.1 shows the simulation results of the contributions from all the four terms in equation 6.4 to the x component of the electric field. This is from the simulation of the field-aligned current with particle precipitation localized in the vicinity of the upward field-aligned current from $x = -2$ km to $x = -10$ km (Figure 4.12). We see that at $x = -1.89$ km, where we have a large electron pressure gradient in the x direction, there is some contribution from the electron pressure gradient term to the x component of the electric field, although it is not large compare to the contribution from the $\mathbf{v}_e \times \mathbf{B}$ term. Another aspect to notice is the non-constant electric field (with altitude), and thus the magnetic field lines are not equal potential lines.

6.2 Ionospheric conductivities

The ionospheric conductivities (Pedersen and Hall conductivities) are derived under the steady state assumption. For simplicity, I consider one species of ion and assume charge neutrality (i.e. $n_e = n_i$). I also assume $\mathbf{v}_n = 0$ because we can always transfer the electric field into the moving neutral frame. As I mentioned above, the electron pressure gradient term has certain contributions to the electric field, but it is relatively small compared to the main contribution from the $\mathbf{v}_e \times \mathbf{B}$ term. For the moment, in deriving the ionospheric conductivities, we just ignore both electron and ion pressure gradient terms in the electron and ion momentum equations. I will discuss the influence of the electron pressure gradient on the ionospheric current in the section considering the height integrated ionospheric current. In the lower ionosphere, we can also neglect gravity as well as the Coulomb collision terms because they are much smaller than the dominant terms (i.e. the electric force, Lorentz force and plasma-neutral collision terms). The ion and electron momentum equations, in

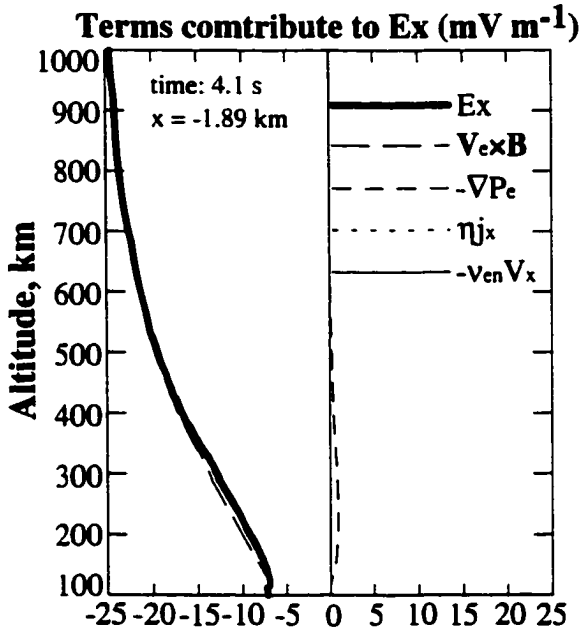

Figure 6.1: Contribution from different terms to the electric field at the location of large electron pressure gradient. There is a sharp electron number density gradient at $x = -2$ km, i.e. the boundary of particle precipitation.

steady state (i.e. ignore the inertia terms), can then be written as:

$$0 = ne(\mathbf{E} + \mathbf{v}_i \times \mathbf{B}) - nm_i\nu_{in}\mathbf{v}_i \tag{6.5}$$

$$0 = -ne(\mathbf{E} + \mathbf{v}_e \times \mathbf{B}) - nm_e\nu_{en}\mathbf{v}_e \tag{6.6}$$

From equations (6.5) and (6.6), the ion and electron velocity components parallel to $\mathbf{B}$ are:

$$\mathbf{v}_{i\|} = \frac{e}{m_i\nu_{in}}\mathbf{E}_\| \tag{6.7}$$

and

$$\mathbf{v}_{e\|} = -\frac{e}{m_e\nu_{en}}\mathbf{E}_\| \tag{6.8}$$

Taking the cross product of equations (6.5) and (6.6) with $\mathbf{B}$ and eliminating the terms of $\mathbf{v}_i \times \mathbf{B}$ and $\mathbf{v}_e \times \mathbf{B}$, respectively, yields

$$\mathbf{v}_i = \frac{e}{m_i\nu_{in}}\mathbf{E}_\| + \frac{1}{B}\frac{\omega_{ci}}{\omega_{ci}^2 + \nu_{in}^2}(\nu_{in}\mathbf{E}_\perp - \omega_{ci}\hat{\mathbf{b}} \times \mathbf{E}) \tag{6.9}$$

and

$$\mathbf{v}_e = -\frac{e}{m_e\nu_{en}}\mathbf{E}_\| - \frac{1}{B}\frac{\omega_{ce}}{\omega_{ce}^2 + \nu_{en}^2}(\nu_{en}\mathbf{E}_\perp + \omega_{ce}\hat{\mathbf{b}} \times \mathbf{E}) \tag{6.10}$$

Where $\hat{\mathbf{b}}$ is a unit vector in the direction of $\mathbf{B}$, ω_{ci} and ω_{ce} are ion's and electron's gyrofrequencies, respectively, that are defined by

$$\omega_{ci} = \frac{eB}{m_i} \tag{6.11}$$

and

$$\omega_{ce} = \frac{eB}{m_e} \tag{6.12}$$

Now, using $\mathbf{j} = ne(\mathbf{v}_i - \mathbf{v}_e)$, we have

$$\mathbf{j} = \sigma_0\mathbf{E}_\| + \sigma_P\mathbf{E}_\perp + \sigma_H\hat{\mathbf{b}} \times \mathbf{E} \tag{6.13}$$

Where σ_0, σ_P, and σ_H are the so called parallel, Pedersen and Hall conductivities given by

$$\sigma_0 = \frac{ne^2}{m_e\nu_{en}} + \frac{ne^2}{m_i\nu_{in}} \tag{6.14}$$

$$\sigma_P = \frac{ne}{B}\left(\frac{\omega_{ci}\nu_{in}}{\omega_{ci}^2+\nu_{in}^2} + \frac{\omega_{ce}\nu_{en}}{\omega_{ce}^2+\nu_{en}^2}\right) \tag{6.15}$$

$$\sigma_H = \frac{ne}{B}\left(\frac{\omega_{ce}^2}{\omega_{ce}^2+\nu_{en}^2} - \frac{\omega_{ci}^2}{\omega_{ci}^2+\nu_{in}^2}\right) \tag{6.16}$$

The horizontal components of the current, j_x and j_y (assuming $\hat{\mathbf{b}}$ is in z direction), can then be calculated by

$$j_x = \sigma_P E_x - \sigma_H E_y \tag{6.17}$$

and

$$j_y = \sigma_H E_x + \sigma_P E_y \tag{6.18}$$

Remember that the above derivation is for the lower ionosphere, where we ignored the Coulomb collision between ions and electrons. For higher altitudes where we cannot ignore the Coulomb collisions, a small correction should be made to the parallel conductivity.

$$\sigma_0 = \frac{ne^2}{m_e(\nu_{en}+\nu_{ei})} + \frac{ne^2}{m_i\nu_{in}} \tag{6.19}$$

Since ionospheric conductivities are proportional to plasma number density and also depend on the ion-neutral and electron-neutral collision frequencies that are strongly related to the ion as well as electron temperatures, they change with time according to the change of the space weather environment (i.e. the neutral density and temperature and ion as well as electron density and temperature). Figure 6.2 shows a typical conductivity profiles for the mid-latitude ionosphere Johnson [1961].

Figure 6.3 shows the ionospheric conductivity profiles from one of the simulation results, the simulation of the field-aligned current layers with particle precipitation localized in the vicinity of the upward field-aligned current layer (chapter 4).

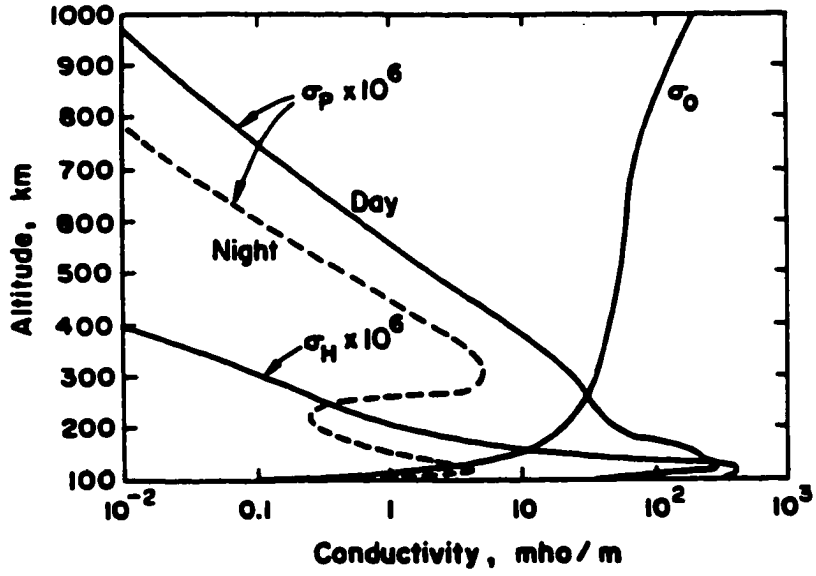

Figure 6.2: Typical conductivity values for the mid-latitude ionosphere. Notice that the value for Pedersen and Hall conductivities are multiplied by 10^6. [From "Satellite Environment Handbook," edited by F. Johnson (1961).]

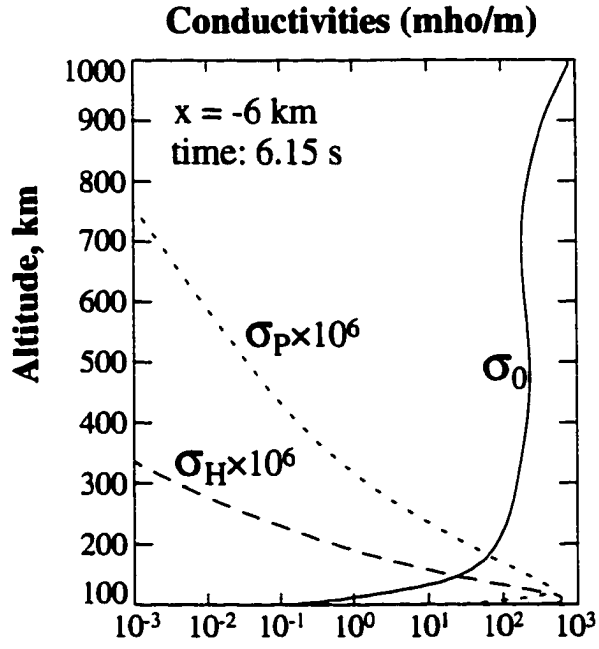

Figure 6.3: Ionospheric conductivity profiles in the center of the upward field-aligned current layer where a particle precipitation with characteristic energy of 250 eV and energy flux of 40 mW/m^2 is added.

6.3 Height integrated conductivities

Ionosphere-magnetosphere coupling is a rather complicated problem. To address this problem, one usually needs to make assumptions depending on where the emphasis is, i.e. whether it is in the magnetosphere (large scale) or in the ionosphere (small scale). It also depends on the time scale of a given problem. For instance, because of the collisionless property of the plasma in the magnetosphere, charged particles are frozen in the magnetic field. Magnetic field lines for collisionless plasma are at equal potential such that the electric field along the magnetic field line is constant. Based on this idea, several global (large) scale magnetosphere-ionosphere coupling models have been developed (e.g. Raeder *et al.* [1996]; Raeder *et al.* [1998]; Spiro *et al.* [1981]; Reiff *et al.* [1981]; Wolf [1975]; and Wolf *et al.* [1982]). Under the assumption that the magnetic field lines are equal potential, all these large scale models map the electric field in the magnetosphere down to the ionosphere so that they can use the height integrated conductivities to calculate the ionospheric currents and the resulting coupling. Implicit in the boundary condition these large scale models also use a steady state assumption, i.e., their time scale is longer than the Alfvén wave bounce time in the ionosphere-magnetosphere system.

If the electric field is constant with altitude (assumed by many global magnetosphere-ionosphere coupling models such as Raeder *et al.* [1996]; Spiro *et al.* [1981]; Reiff *et al.* [1981]; and Wolf *et al.* [1982]), we can integrate the equation (6.13) along the magnetic field line and obtain the horizontal component of the height integrated current as

$$\begin{aligned} \mathbf{J}_\perp &= \int dz(\sigma_P \mathbf{E}_\perp + \sigma_H \hat{\mathbf{b}} \times \mathbf{E}) \\ &= \Sigma_P \mathbf{E}_\perp + \Sigma_H \hat{\mathbf{b}} \times \mathbf{E} \end{aligned} \tag{6.20}$$

Where $\Sigma_P = \int \sigma_P dz$ and $\Sigma_H = \int \sigma_H dz$ are the height integrated Pedersen and Hall conductivities, respectively.

These large scale models are qualitatively good to solve problems with large scale structures such as the plasma convection motion in the magnetosphere-ionosphere system. In solving this kind of problem, they treat the ionosphere as a boundary layer. Thus they do not pay attention to the detailed structures within the ionosphere. But the height integrated ionospheric current in equation (6.20) is not sufficient because one also needs to consider the average over time and horizontal spatial scales. For a correct description of the large scale (and slowly varying) $\mathbf{J}_\perp$, global models require the properly averaged (in time and space) height integrated ionospheric conductivities, i.e.:

$$\begin{aligned}
\tilde{\mathbf{J}}_\perp &= \frac{1}{T_0}\frac{1}{L_x}\int_t^{t+T0} \mathrm{d}t \int_x^{x+L_x} \mathrm{d}x \mathbf{J}_\perp \\
&= \frac{1}{T_0}\frac{1}{L_x}\int_t^{t+T_0} \mathrm{d}t \int_x^{x+L_x} \mathrm{d}x \int \mathrm{d}z(\sigma_P \mathbf{E}_\perp + \sigma_H \hat{\mathbf{b}} \times \mathbf{E}_\perp) \\
&= \Sigma_P \tilde{\mathbf{E}}_\perp + \Sigma_H \hat{\mathbf{b}} \times \tilde{\mathbf{E}}_\perp
\end{aligned} \tag{6.21}$$

where, T_0 and L_x are typical time and horizontal spatial scales, respectively. So for a correct description of the large scale (and slowly varying) $\tilde{\mathbf{J}}_\perp$, global models require the properly averaged (in time and space) height integrated ionospheric conductivities. From equation (6.21), the height integrated Pedersen conductivity is given by:

$$\Sigma_P = \frac{1}{\tilde{\mathbf{E}}_\perp}\langle\langle \int \sigma_P \mathbf{E}_\perp \mathrm{d}z \rangle_t \rangle_x \tag{6.22}$$

However, in the study of the fast temporal and small spatial scale ionospheric structures such as the discrete aurora, the assumption that the magnetic field line is at equal potential does not apply because the plasma, especially ions, in the lower ionosphere are highly collisional. Due to the resistivity the parallel component of the electric field ($\mathbf{E}_{||}$) is no longer zero. So the electric field is not constant along the magnetic field line in the ionosphere (Figure 6.1). Furthermore, the time scale for discrete aurora is only a few seconds or even less. The structure of dynamic auroral arcs usually changes in a short time period.

Can we still use the ionospheric conductivities to calculate the ionospheric currents although the ionospheric conductivities are defined for the steady state assumption? The answer is yes for most cases, because ionospheric conductivities are actually a measure of the plasma-neutral collision frequencies. The Pedersen and Hall conductivities get their maximum values at the lower ionosphere (about 120 km) and drop very rapidly with altitude. At the altitude where the Pedersen and Hall conductivities are most effective, the ion-neutral and electron-neutral collision frequencies are very large, higher than $10^4\ s^{-1}$. The time scale for these collisions is less than 10^{-4} seconds, which can set the lower ionosphere into equilibrium in a time much shorter than the typical time scale for the small spatial scale structure in the ionosphere. Figure 6.4 shows contour plots of the ionospheric current (j_x and j_y) from the field-aligned current simulation results (the top panel) which is calculated by using $\mathbf{j} = \nabla \times \mathbf{B}$, and the Pedersen and Hall current (the bottom panel) computed from the electric field and ionospheric conductivities by using equation (6.17) and (6.18), at the simulation time of 4.1 s. The Pedersen conductivity σ_P and Hall conductivity σ_H are calculated by using the parameters (i.e., electron number density, electron temperature, magnetic field, etc.) from the simulation. If we overlap the top and the bottom panels, the two results are almost identical.

Since we can use the ionospheric conductivities, can we also use the idea of height integrated conductivities to compute the height integrated ionospheric current? If we can, then to what altitude should the height integration of the ionospheric conductivities extend? And, to calculate the ionospheric current, what electric field should be used? Should it be the electric field in the magnetosphere or the one in the ionosphere? I have investigated this problem with my three fluid time-dependent ionospheric model which is an excellent tool to address this problem.

Let us first look at a simple example, i.e. the simulation without particle precipitation

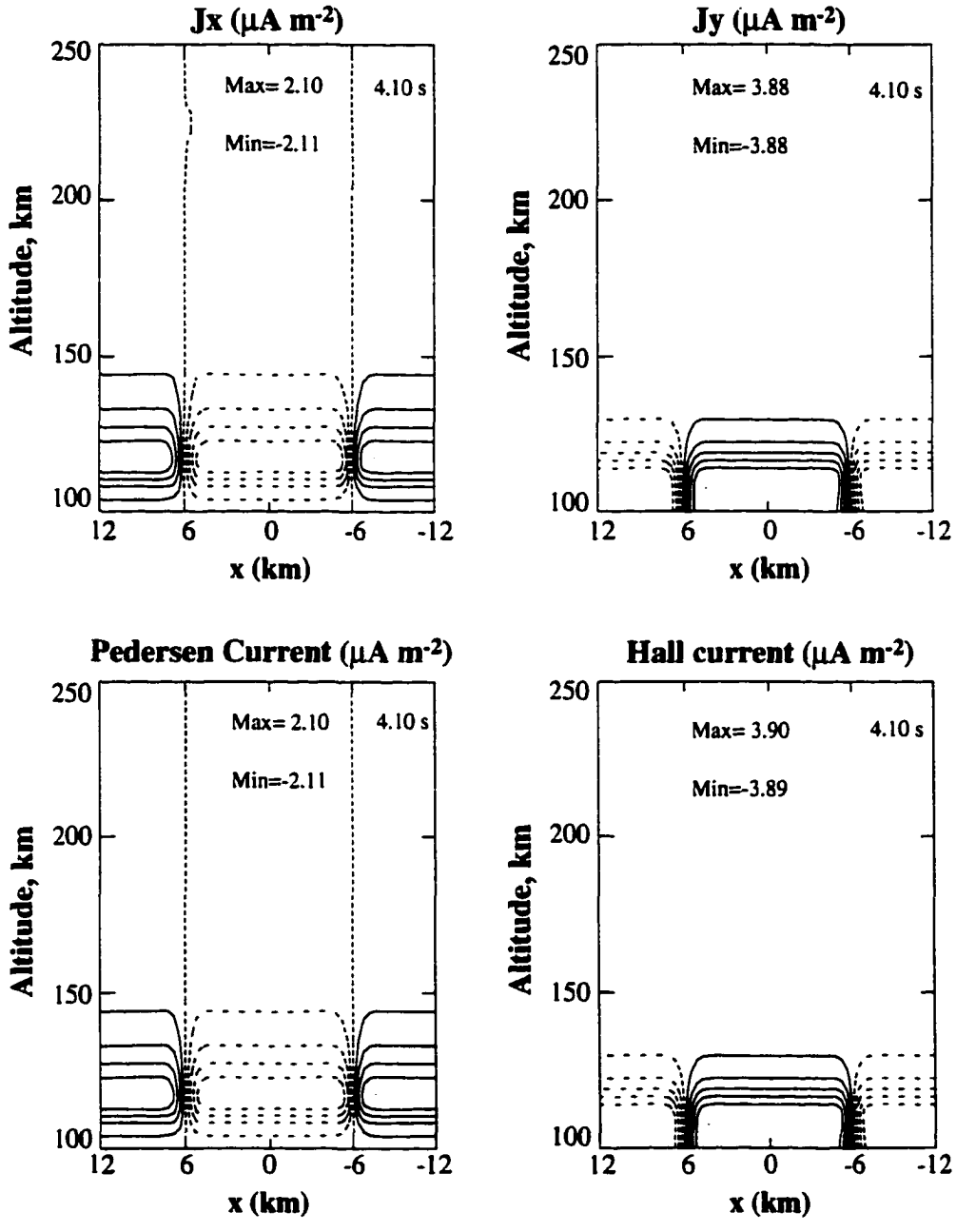

Figure 6.4: Contour plots of current for j_x and j_y (the top panel) from the field-aligned current simulation results (derived from $\mathbf{j} = \nabla \times \mathbf{B}$), and the Pedersen and Hall current (the bottom panel) computed from the electric field and ionospheric conductivities, at the simulation time of 4.1 s.

which is mentioned in chapter 3. Figure 6.5 shows the electric field (left) and ionospheric conductivity (right) profiles at $x = 0$ km (i.e. outside the current layers) at the time $t = 1.026$ s (top) and $t = 4.1$ s (bottom) of the simulation. The ionospheric conductivity profiles at these two times are actually the same because there is no particle precipitation in this case and the effect of the recombination processes is not obvious in such a short time. The amplitude of the electric field (E_x) increases from 5 mV/m at $t = 1.026$ s to more than 10 mV/m at $t = 4.1$ s. Noticing that in this case, it is not easy to distinguish the contributions from different source terms because the $\mathbf{v}_e \times \mathbf{B}$ term is absolutely dominant over all other terms and in the plots is overlapping the total value of E_x. All other terms are actually lined along the zero line.

We can now compute the height integrated current, i.e. integrate the current density from the simulation (obtained by $\mathbf{j} = \nabla \times \mathbf{B}$) along the magnetic field line (altitude), and compare it with the ionospheric current calculated from the electric field and the height integrated ionospheric conductivities. To do this, we first need to determine to what altitude the integration should extend, and because the electric field obviously is not constant along the magnetic field line, we also need to determine which value of the electric field (at what altitude) to use. The idea of the large scale models, i.e., to map the electric field in the magnetosphere into the ionosphere, using the electric field in the magnetosphere (at the top boundary), seems unreasonable. The original concept of the height integrated conductivities was to assume that the electric field ($\mathbf{E}_\perp$) in the ionosphere does not change much (Nishida [1978]). So we should use the value of the electric field in the ionosphere.

Figure 6.5 demonstrates that the Pedersen as well as Hall conductivities drop to very low values at altitudes above 200 km (less than 1% of their maximum value at about 120 km). So it is safe to extend the integration to 250 km. Both Pedersen and Hall conductivities have large values in the lower ionosphere (below 120 km), and it appears that the electric

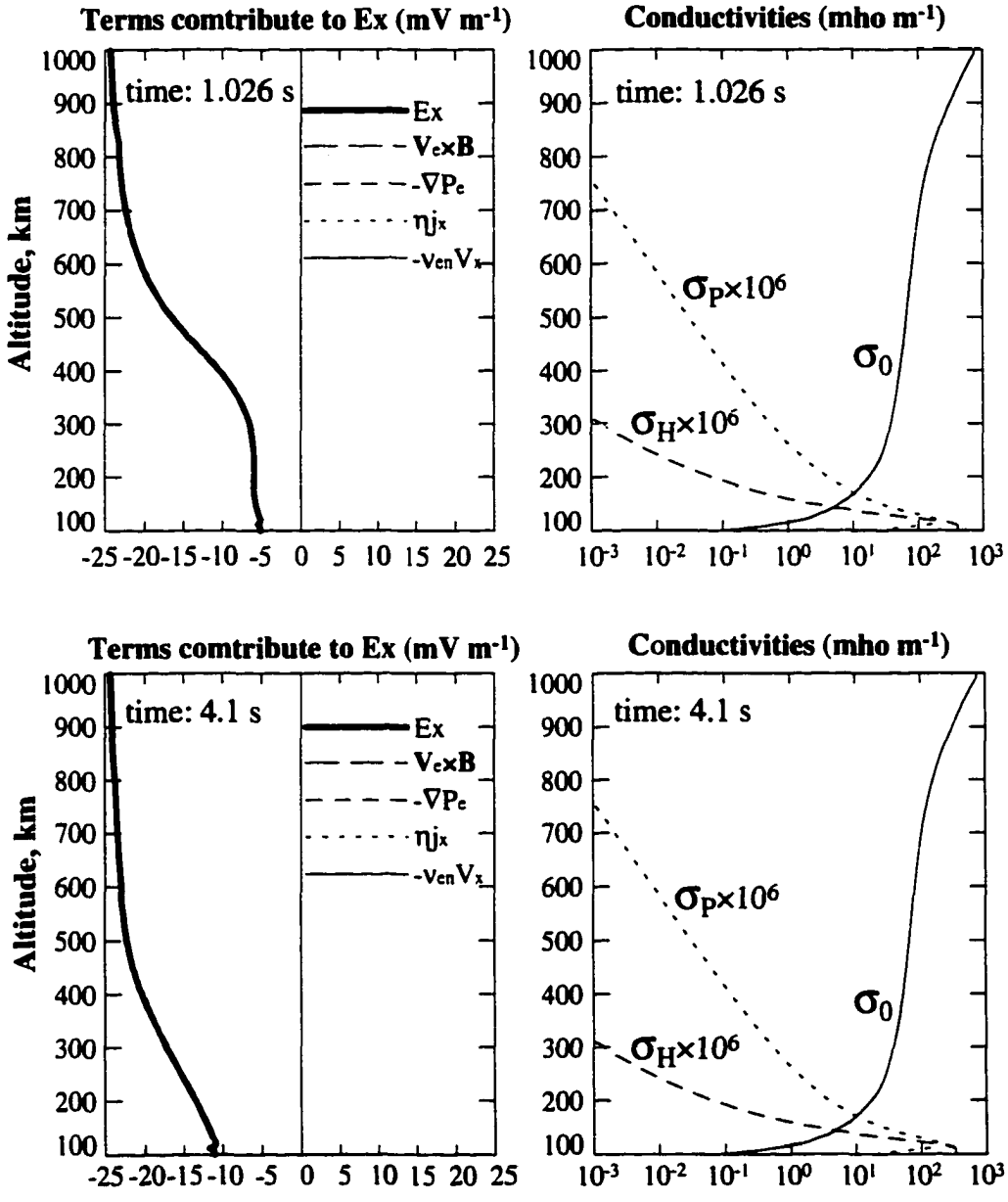

Figure 6.5: Contribution from all terms in generalized Ohm's law to the x component of the electric field (left) and the ionospheric conductivity profiles (right) in the field-aligned current layers simulation mentioned in chapter 3 at the location of $x = 0$ km (i.e. outside the current layers) at the time $t = 1.026$ s (right after the Alfvén wave reflection) (top panel) and $t = 4.1$ s (bottom panel).

field below 120 km is also relatively constant. Thus it is reasonable to use the value of the electric field near the lower boundary (below 120 km). The plots in Figure 6.6 show comparisons between the height integrated current directly calculated from the simulation results (i.e. integrating $\mathbf{j} = \nabla \times \mathbf{B}$ along the altitude up to 250 km) (solid lines) and the current obtained from the electric field and the height integrated ionospheric Pedersen as well as Hall conductivities by using equation (6.20) (dashed lines). The electric field used here is the value at the altitude of 116 km. The plots in the top panel are at the simulation time of 1.026 s, shortly after the Alfvén wave is reflected at the lower boundary. The bottom panel is at $t = 4.1$ s. The solid lines are the results directly from the simulation (i.e. integrating $\mathbf{j} = \nabla \times \mathbf{B}$ along the magnetic field line) and the dotted lines are the results derived from the electric field and the height integrated ionospheric conductivities. The two results agree quite well.

For comparison, Figure 6.7 shows the same plots as Figure 6.6 but using the electric field at the altitude of 250 km (instead of the value at 116 km) in calculating the ionospheric current from the height integrated ionospheric conductivities. Since the electric field is not constant along the magnetic field line, the result is not the same as shown in Figure 6.6. The ionospheric current calculated from the ionospheric conductivities by using the electric field at the altitude of 250 km does not agree well with the real height integrated ionospheric current from the simulation. Using the result from Figure 6.6, the error in the current densities computed from the height integrated conductivity is approximately equal to the ratio of the electric field assumed as input for equation (6.20) and the electric field at the altitude of 116 km. In Figure 6.5, we see that electric field in the magnetosphere (i.e., at the top boundary) is about five and two times as large as its value in the lower ionosphere at times $t = 1.026$ s and $t = 4.1$ s, respectively. If we use the electric field in the magnetosphere (top boundary) to calculate the height integrated ionospheric current

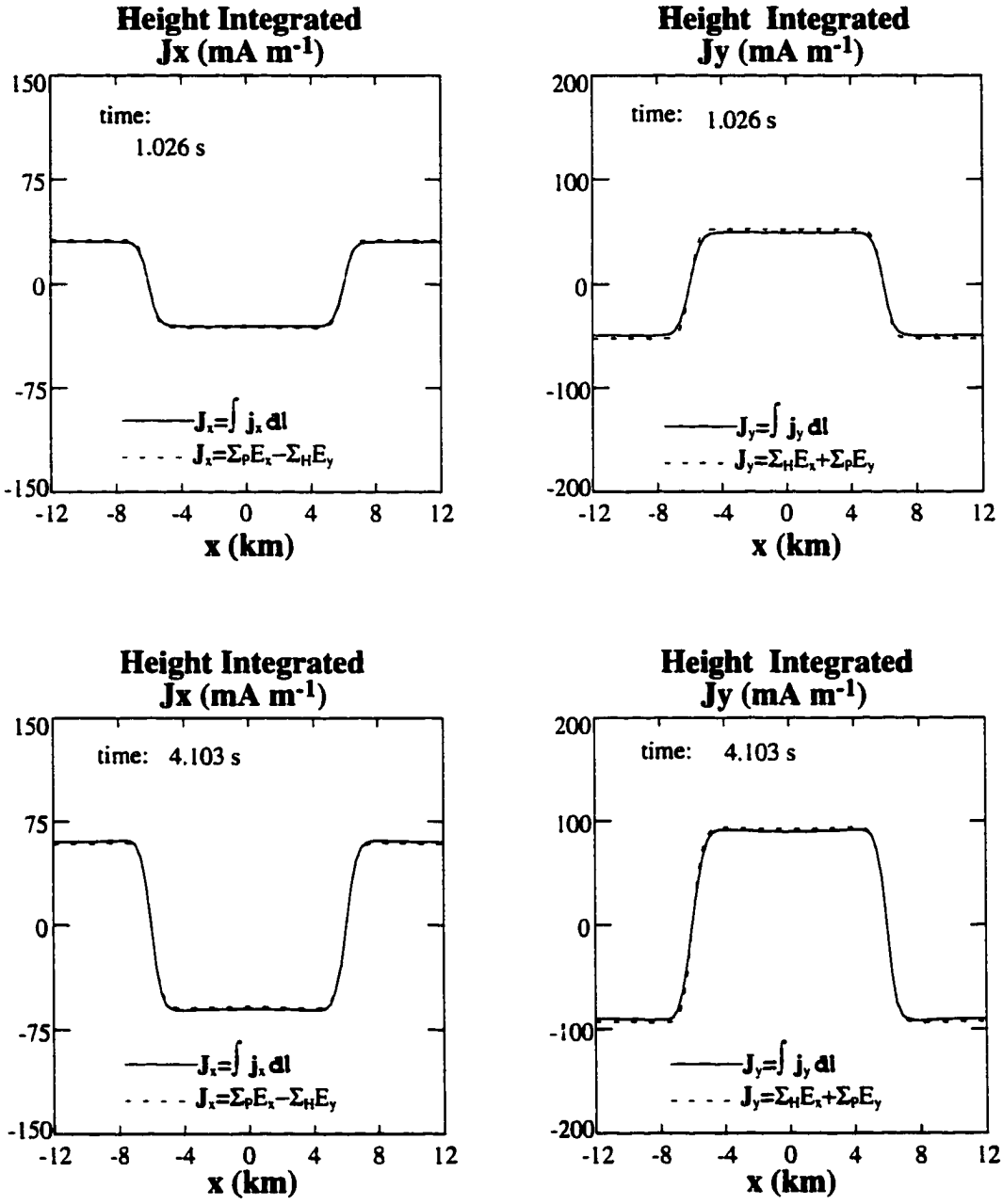

Figure 6.6: Comparison between the height integrated ionospheric current from the simulation results and the current calculated from the electric field at 116 km and the height integrated ionospheric conductivities. The top panel is at $t = 1.026$ s, shortly after the Alfvén wave is reflected at the lower boundary. The bottom panel is at $t = 4.1$ s. The solid lines represent the results directly from the simulation, i.e. integrating $\mathbf{j} = \nabla \times \mathbf{B}$ along the magnetic field line, and the dotted lines are the results obtained from the electric field and the height integrated ionospheric conductivities

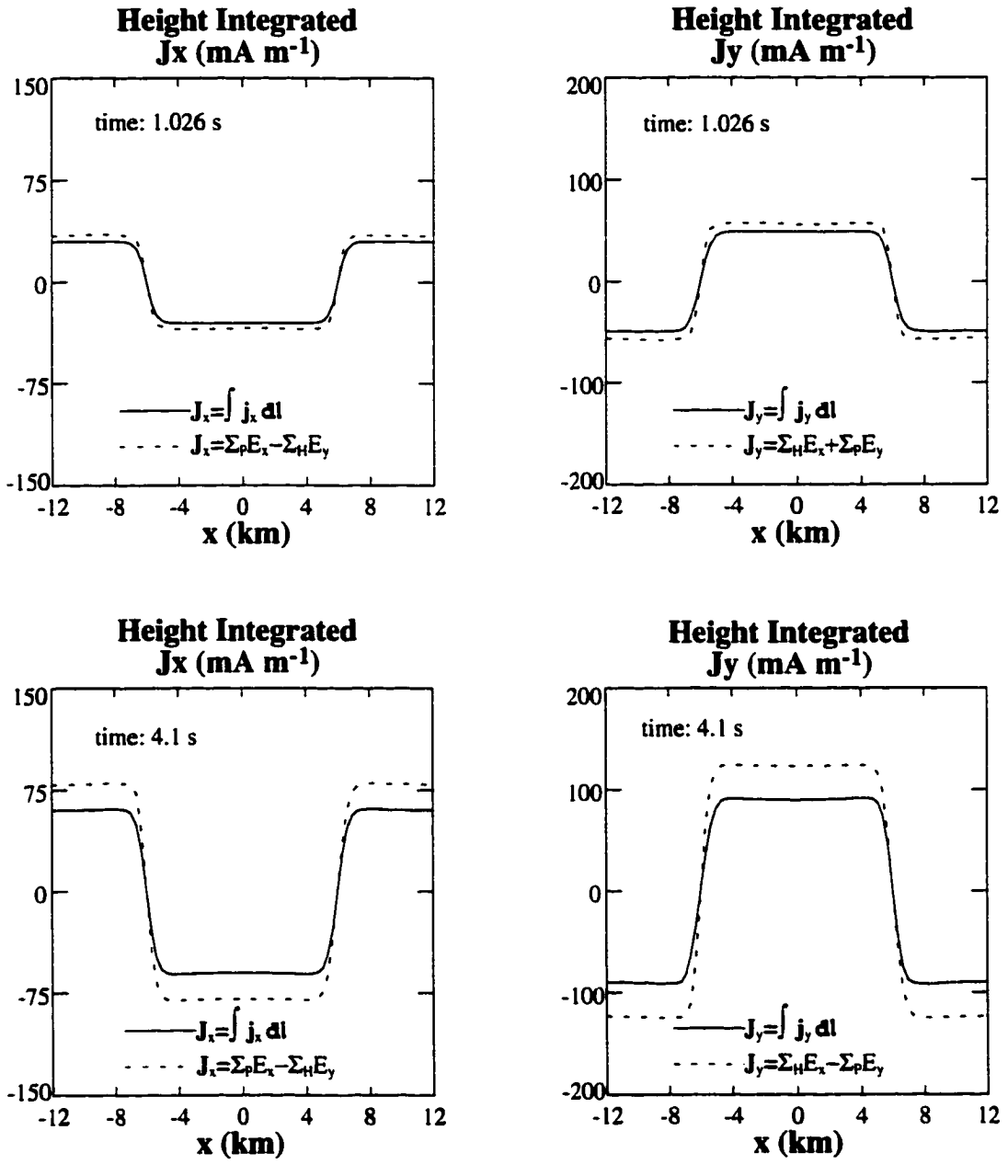

Figure 6.7: Comparison between the height integrated ionospheric current from the simulation results and the current calculated from the height integrated ionospheric conductivities by using electric field at 250 km. The solid lines represent the results directly from the simulation, i.e. integrating $\mathbf{j} = \nabla \times \mathbf{B}$ along the magnetic field line, and the dotted lines are the results obtained from the electric field and the height integrated ionospheric conductivities.

(as people did in most global scale ionosphere-magnetosphere coupling models), the results can be much worse.

Let us consider another example. This is the simulation of the field-aligned current with particle precipitation added in the vicinity of the upward field-aligned current layer (Chapter 4). The characteristic energy and energy flux of the precipitation are 250 eV and 40 mW/m^2, respectively. In this simulation, there is a strong electron pressure gradient at the two sharp precipitation boundaries, i.e. at $x = -2$ and $x = -10$ km. As mentioned above, the derivation of the ionospheric conductivity has ignored the pressure gradient terms in both the ion and electron momentum equations. This is the usual way to derive the ionospheric conductivities, and it makes the derivation much easier. Here I want to clarify the role and influence of a large horizontal plasma pressure gradient on the integral horizontal currents computed with the height integrated conductivity.

Figure 6.8 shows the electric field and conductivity profiles at $x = -1.89$ km, which is close to the sharp precipitation boundary at $x = -2$ km. The top panel is at the simulation time of $t = 1.026$ s and the bottom panel is at $t = 4.1$ s. Notice that at both $t = 1.026$ s and $t = 4.1$ s, there is a contribution from the electron pressure gradient to the electric field. The Pedersen and Hall conductivities at the lower ionosphere increase to higher values at $t = 4.1$ s, although it is not easy to see in the scale of this plot.

Figure 6.8 shows that the electron pressure gradient does have a certain contribution to the electric field, even though it is not large. Since the derivation of the Pedersen and Hall conductivities does not include the pressure gradient terms, i.e., these conductivities cannot reflect any effect from the electron pressure gradient, we need to verify whether the contribution from the plasma pressure gradient terms has a severe impact on the calculation of the ionospheric current. Let us first look at the ion and electron momentum equations with the plasma pressure gradient terms. When the ion pressure gradient term is included,

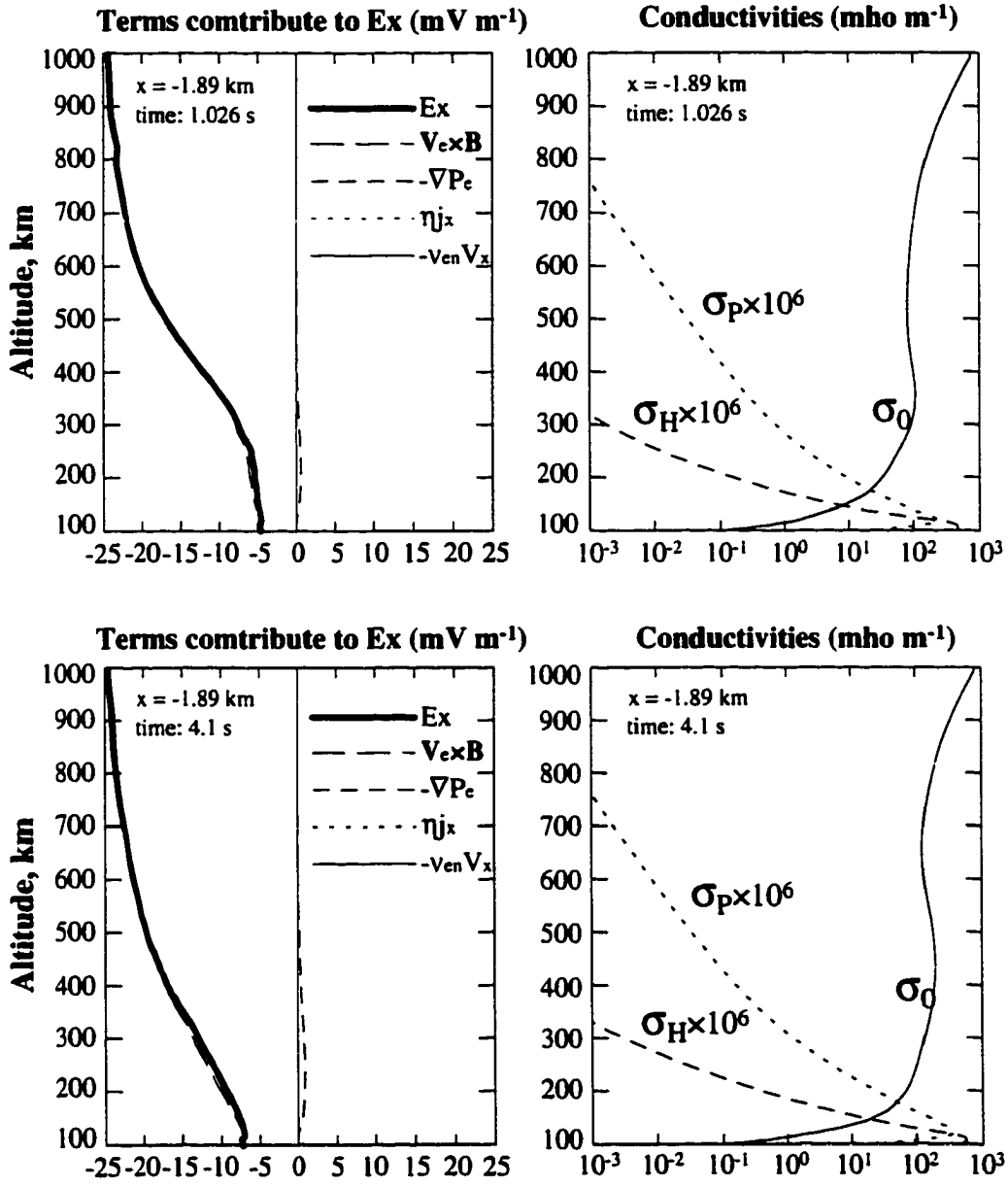

Figure 6.8: Contribution from all terms in generalized Ohm's law to the x component of the electric field (left) and the ionospheric conductivity profiles (right) in the simulation of field-aligned current layers with particle precipitation in the vicinity region of the upward field-aligned current layer (chapter 3). All the plots are at the location of $x = 1.89$ km (where the electron pressure gradient is large). The top panel is at the time $t = 1.026$ s (which is right after the Alfvén wave reflection). The bottom panel is at $t = 4.1$ s.

equation (6.9) can be rewritten as

$$\begin{aligned}\mathbf{v}_i &= \frac{e}{m_i\nu_{in}}\mathbf{E}_{\parallel} + \frac{1}{B}\frac{\omega_{ci}}{\omega_{ci}^2+\nu_{in}^2}(\nu_{in}\mathbf{E}_{\perp} - \omega_{ci}\hat{\mathbf{b}}\times\mathbf{E}) \\ &\quad -\frac{1}{nm_i}\frac{\omega_{ci}}{\omega_{ci}^2+\nu_{in}^2}\left(-\hat{\mathbf{b}}\times\nabla p_i + \frac{\nu_{in}}{\omega_{ci}}\nabla p_i\right) \qquad (6.23)\end{aligned}$$

Similarly, the electron velocity equation (6.10) can be rewritten as

$$\begin{aligned}\mathbf{v}_e &= -\frac{e}{m_e\nu_{en}}\mathbf{E}_{\parallel} - \frac{1}{B}\frac{\omega_{ce}}{\omega_{ce}^2+\nu_{en}^2}(\nu_{en}\mathbf{E}_{\perp} + \omega_{ce}\hat{\mathbf{b}}\times\mathbf{E}) \\ &\quad -\frac{1}{nm_e}\frac{\omega_{ce}}{\omega_{ce}^2+\nu_{en}^2}\left(\hat{\mathbf{b}}\times\nabla p_e + \frac{\nu_{en}}{\omega_{ce}}\nabla p_e\right) \qquad (6.24)\end{aligned}$$

There are two terms in the electron velocity equation that are related to the electron pressure gradient. One is the Hall-like term (i.e. $\hat{\mathbf{b}}\times\nabla p_e$), and the other is the Pedersen-like term ($\frac{\nu_{en}}{\omega_{ce}}\nabla p_e$). Since the electron gyrofrequency ω_{ce} is much larger the the electron-neutral collision frequency ν_{en} in the ionosphere, we can ignore the Pedersen-like term. Since both the electron and ion motions contribute to the current, we need also to verify the importance of the ion pressure gradient terms. The ratio of the coefficient in front of the ion pressure gradient terms to the one in front of the electron pressure gradient term is

$$\frac{\omega_{ci}^2}{\omega_{ci}^2+\nu_{in}^2}\frac{\omega_{ce}^2+\nu_{en}^2}{\omega_{ce}^2}$$

Since $\omega_{ce} \gg \nu_{en}$ in the ionosphere, the ratio is

$$\frac{\omega_{ci}^2}{\omega_{ci}^2+\nu_{in}^2}$$

The maximum value of this ratio is 0.5 at the altitude when $\omega_{ci} = \nu_{in}$. In the lower ionosphere, we have $\omega_{ci} \ll \nu_{in}$, while at high altitude, it is the opposite, i.e. $\omega_{ci} \gg \nu_{in}$, but both cases make the ratio much less than unity. This means that the height integrated effect of the ion pressure gradient is negligible compared to the contribution from the electron pressure gradient. So the only large influence of the plasma pressure gradient terms on the

ionospheric current is from the Hall-like term $\hat{\mathbf{b}} \times \nabla p_e$. In the simulation, $\nabla p_e = \frac{\partial p_e}{\partial x}\hat{x}$, the Hall-like electron pressure gradient term contributes to the y component of the ionospheric current.

Figure 6.9 shows the comparison of the height integrated ionospheric current calculated from the integration of the real simulation current (i.e. $\mathbf{j} = \nabla \times \mathbf{B}$) and the ionospheric current derived from the electric field and the height integrated Pedersen as well as Hall conductivities. The top panel is at time $t = 1.026$ s, and the bottom panel shows the results at $t = 4.1$ s. Again, the solid lines are the height integrated real simulation currents, and the dotted lines represent the ionospheric currents calculated from the height integrated ionospheric conductivities and using the electric field at the altitude of 116 km. We see that the two results agree well in the x component, which is associated with Pedersen current. But in the y component (Hall current), the real height integrated current shows big spikes right at the two sharp precipitation boundaries (in agreement with my estimate), while the current calculated from the height integrated conductivities and electric field does not show any change related to the large electron pressure gradient. Other than the big spikes at the two sharp precipitation boundaries, the two results of the y component of ionospheric current agree very well in other locations.

6.4 Summary and discussion

I have investigated the ionospheric electric field, Pedersen and Hall conductivities, and the height integrated ionospheric current in this chapter. The main results are:

(1) The simulation results show that on short time scale (a few seconds), the electric field in the ionosphere in not constant along the magnetic field line. But if the plasma convection in the magnetosphere is steady such as the simulation examples shown in this chapter (i.e. the plasma velocity perturbation is fixed at the top boundary of the simulation

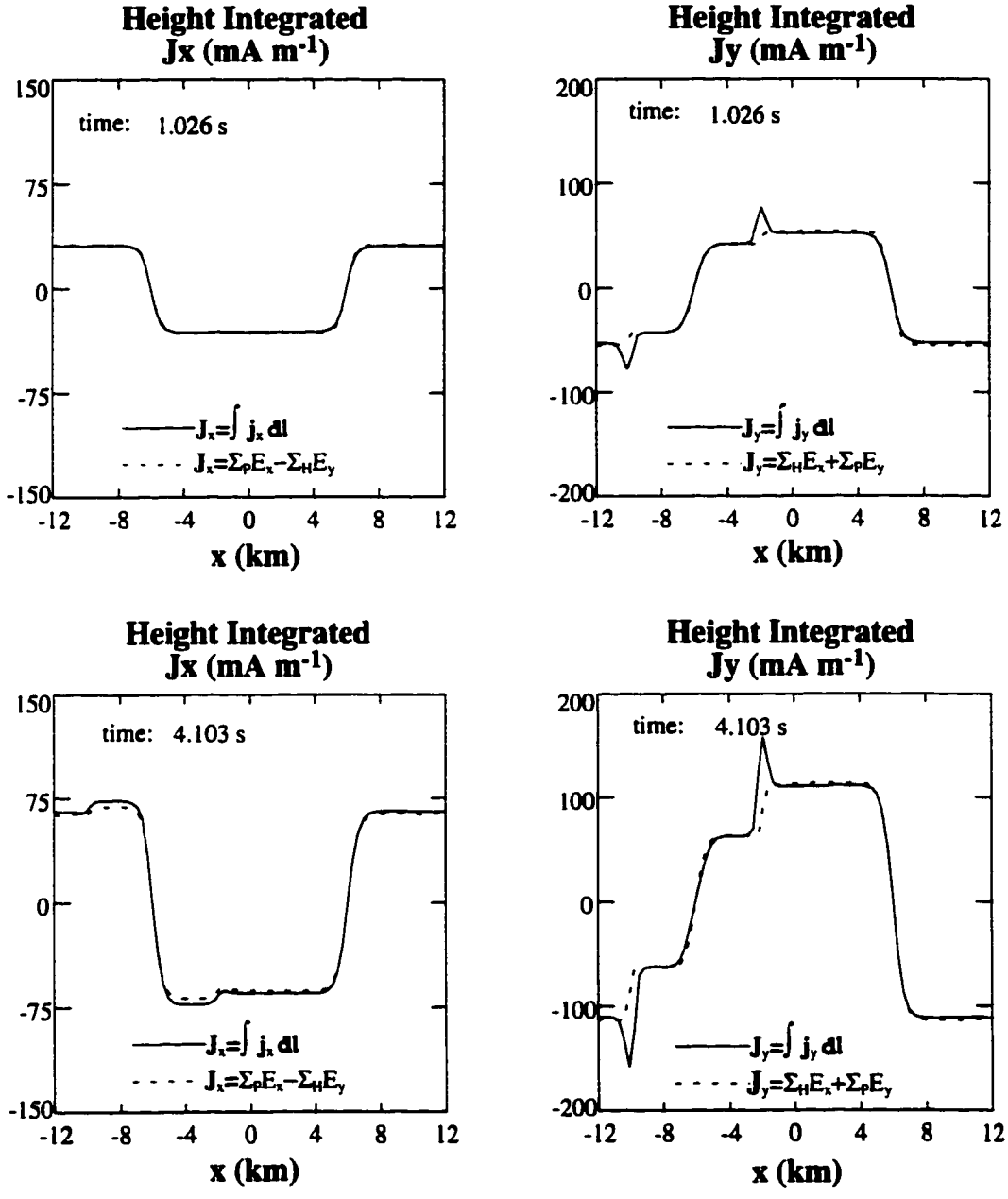

Figure 6.9: Height integrated ionospheric current for the field-aligned current simulation with particle precipitation added in the vicinity area of the upward field-aligned current layers. The solid lines represent the results directly from the simulation, i.e. integrating $\mathbf{j} = \nabla \times \mathbf{B}$ along the magnetic field line, and the dotted lines are the results obtained from the electric field (at 116 km) and the height integrated ionospheric conductivities. The top panel is at $t = 1.026$ s, and bottom panel is at $t = 4.1$ s.

box), as time goes on, the ionospheric electric field has the tendency to increase its value to bring it closer to the electric field in the magnetosphere. That is the reason why in large scale and steady state magnetosphere-ionosphere coupling models one can map the electric field in the magnetosphere down to the ionosphere. The electron pressure gradient term has some contribution to the electric field in the region of large electron pressure gradient, although it is relatively small compared to the contribution from the $\mathbf{v}_e \times \mathbf{B}$ term.

(2) The ionospheric conductivities (i.e. Pedersen and Hall conductivities) are derived in the usual simplified way, i.e., ignoring all the terms associated with inertia, pressure gradient, and gravity, and assuming one species of ion and the charge neutrality.

(3) To calculate the height integrated ionospheric current by using the height integrated conductivities and the electric field, we should use the electric field at the lower ionosphere, i.e., below 120 km. The integration needs not to be extended higher than 250 km.

(4) The height integrated ionospheric current calculated from the height integrated Pedersen and Hall conductivities (derived in the usual way) and the lower ionospheric electric field agrees with the height integrated ionospheric current computed from the real simulation current (i.e. $\mathbf{j} = \nabla \times \mathbf{B}$) if there is no large electron pressure gradient.

(5) The large electron pressure gradient has a Hall-like contribution to the ionospheric current, but has little influence on the Pedersen current.

Chapter 7

Conclusion

The problem of the ionosphere-magnetosphere coupling processes has been studied for many years. Several global (large scale) models have been developed to study the magnetosphere-ionosphere coupling with emphasis on the magnetospheric physics (e.g. Raeder *et al.* [1996]; Raeder *et al.* [1998]; Slinker *et al.* [1999]; Lyons [1998]; Kan [1993]; Papadopoulos [1977]; Spiro *et al.* [1981]; Reiff *et al.* [1981]; Wolf [1975]; and Wolf *et al.* [1982]). These global models consider a large scale and averaged magnetosphere-ionosphere coupling, such as the coupling of the magnetospheric convection motion into the ionosphere at a time scale much longer than the Alfvén wave bounce time in this system. Although some researchers have emphasized the effect of the ionosphere in the coupling between the ionosphere and the magnetosphere (e.g. Atkinson [1970]), it seems that the only aspect of this coupling which is widely accepted is the role of the ionosphere in supplying plasma to the magnetosphere. Recent research and observations have shown that the ionosphere is not merely a passive recipient of the magnetospheric dynamics (e.g. Newell [1998]). The ionosphere can be very important and sometimes even plays the crucial role in the ionosphere and magnetosphere coupled system.

There are ionospheric models which focus on vertical transport and therefore are one-dimensional, i.e., they treat the altitude dependence of the relevant transport property (e.g. Lummerzheim and Lilensten [1994]; Link [1992]; Strickland *et al.* [1976]; Nagy and Banks [1970]; Mantas [1974]; Lanchester *et al.* [1997]; and Lanchester *et al.* [1998]). Others are large scale ionospheric convection models (e.g. Roble and Rees [1977]; Fuller-Rowell and Rees [1980]; Sojka [1989]; Schunk [1988]; Roble *et al.* [1987]; and Maurits and Watkins [1996]) that determine convection by a steady state ion momentum equation. These large scale models cannot deal with the small spatial structure such as the discrete auroral arcs, and since they neglect the ion inertia term in the ion momentum equation, they cannot resolve the Alfvén wave propagation in the system which is so important in the study of the ionosphere-magnetosphere coupling. Therefore they cannot resolve the small scale time dependent ionosphere dynamics. The study in this thesis is focused on small spatial ($\sim$ 1-10 km) and fast temporal (less than 10 seconds) ionospheric phenomena such as the discrete auroral arcs. The two dimensional three-fluid model used in my thesis is tailored to this study.

7.1 The two-dimensional three-fluid ionosphere-magnetosphere coupling model

Starting with the three-fluid model (ion, electron, and neutral dynamics) originally developed by Birk and Otto [1996], I have improved it to a more realistic, dynamic, and quantitative ionospheric model. The model uses the force balanced hydrostatic neutral atmosphere profiles from the MSIS model (Hedin [1991]), depending on the solar condition as the initial setting, and then simulating the small scale ionosphere-magnetosphere coupling processes by using a full set of neutral, ion and electron electromagnetic dynamic

equations. The model includes ionization and recombination processes, the Hall term in Ohm's law, various heat sources in the energy equations that enable it to compute the ionospheric heating of the plasma by different mechanisms, such as the ion heating by the ion-neutral friction, electron heating by particle precipitation, and electron heating by ohmic dissipation. The plasma-neutral contact effects that cool the plasma are also included. The electro-dynamic response and the evolution of the collision frequencies are treated self-consistently in the height resolved ionosphere, such that the model can resolve the dynamic change of the ionospheric conductivities (Pedersen and Hall) and investigate the effect of the ionospheric conductivity change in response to the ionospheric current. The inertia term in the ion momentum equation enables the model to simulate the propagation of Alfvén waves along the magnetic field lines and the evolution of the field-aligned current layers in the ionosphere-magnetosphere system.

This model is the first and to our knowledge the only simulation model that can resolve the dynamic and nonlinear electromagnetic interaction between the ionosphere and the magnetosphere. The interesting and important results from the simulation using this model will be summarized in the following section.

7.2 Main results

I have obtained some very interesting and important new results such as the ion and electron heating in the ionosphere, the effects of the field-aligned current in the ionosphere, tall auroral red rays generated by large field-aligned current layers, and the influence of the electron pressure gradient on the height integrated ionospheric current. All these results will help us to have a better understanding of the role of the ionosphere in the ionosphere-magnetosphere coupling processes.

7.2.1 Ionospheric heating

The three-fluid model used in this work is unique in simulating the ion and electron heating processes in the ionosphere. It includes particle precipitation as well as recombination processes, calculates the collision frequencies between the plasma and neutral (ν_{in} and ν_{en}) self-consistently, and allows Alfvén waves to propagate in the ionosphere-magnetosphere system which enables the computation of the time evolution of the field-aligned current.

The evolution of the ion temperature as a function of height is determined by the following equation:

$$\frac{\partial T}{\partial t} = -\nu_n[\alpha(\mathbf{v}-\mathbf{v}_n)^2 - (T-T_n)] \tag{7.1}$$

where T is ion temperature, T_n is neutral temperature, ν_n is effective ion-neutral collision frequency, α a constant, $\mathbf{v}$ and $\mathbf{v}_n$ are ion and neutral velocities, respectively. When the Alfvén wave propagates from the magnetosphere into the ionosphere, it sets the ion in the ionosphere in motion. This ion motion together with the large ion-neutral collision frequency rapidly heats the ions in the lower ionosphere. The reflection of the Alfvén wave reduces the ion velocity in the incoming wave which lowers the ion heating rate in the lower ionosphere. At the same time, the ion-neutral contact with the large ion-neutral collision frequency in the lower ionosphere strongly cools the ions at lower altitudes so that after the rapid initial ion heating in the lower ionosphere, the maximum ion temperature due to the heating by the Alfvén wave moves to higher altitudes. The altitude extent of the strong ion heating by Alfvén waves depends on the solar conditions. During solar maximum, the altitude of strong ion heating extends from 150 km to about 450 km, while in the solar minimum time, the ion heating is more localized at the lower altitudes (below 280 km). Strictly speaking, a steady state implies $T - T_n = const(\mathbf{v}-\mathbf{v}_n)^2$ but it takes an unrealistic long time scale to achieve a steady state at high altitudes because ν_n decreases exponentially with height.

Electrons can be heated by energetic particle precipitation or by Ohmic dissipation in the field-aligned current layers. The magnitude and the height extent of the electron heating by particle precipitation depends largely on the characteristic energy and the energy flux of the precipitation. But similar to the ion heating, due to the cooling by electron-neutral contact, the maximum electron temperature moves from lower altitudes (at early times) to higher altitudes (at later times). The field-aligned current layers are formed by the shear of the plasma motion (which causes the sheared magnetic field), and inside the field-aligned current layers the ion velocity is generally small, so that the electron heating by the field-aligned current is usually in a different region than the ion heating.

The ionospheric heating simulation is motivated by optical and radar (EISCAT) observations of small scale discrete aurora (Lanchester *et al.* [1999]). The results of the ionospheric ion and electron heating agree quantitatively well with the observation results.

7.2.2 The effects of the field-aligned current in the ionosphere

The propagation of the plasma shear motion from the magnetosphere with the Alfvén wave into the ionosphere forms the field-aligned current in the ionosphere-magnetosphere system (chapter 4). The self-consistently computed ion-neutral collision frequency affects the field-aligned current closed by the Pedersen current in the lower E region of the ionosphere. The field-aligned current simulation also shows the following interesting results:

(1) In two dimensional structures (field-aligned current layer related to the discrete auroral arcs), the field-aligned current can change the plasma number density and the conductivities at the base of the field-aligned current layer. At the base of the upward field-aligned current layer, the convergent motion of both the ions and electrons increases the plasma number density which then increases the Pedersen as well as the Hall conductivities. At the base of the downward field-aligned current layer, on the other hand, the plasma

number density and conductivities decrease due to the divergent motion of the plasma, such that a plasma density hole is formed.

(2) As a result of the plasma density hole and decreasing Pedersen conductivity at the base of the downward field-aligned current layer, this layer widens. The depleted Pedersen conductivity at the center of the base of the downward field-aligned current layer forces the closing Pedersen current around the area of the depleted density, thereby widening the current layer and expanding the region of density depletion.

(3) Due to the different refiection of the Alfvén wave on the two sides of the edge of the sharp particle precipitation boundary, a finite field-aligned current filament in the opposite direction to the main current layer is formed right at the boundary.

(4) In chapter 5, I showed that in the time of the solar maximum, which gives rise to high oxygen density at high altitudes needed for the $O(^1D)$ excitation in the ionosphere, the large field-aligned current provides a reasonably good mechanism for the red line emission in the tall auroral red rays often observed in the solar maximum years.

7.2.3 Ionospheric conductivities

The ionospheric current can be calculated by using a simple Ohm's law $\mathbf{j} = \sigma \cdot \mathbf{E}$. When the customary assumption that the electric field does not change much with height within the ionosphere holds, we can compute the height integrated ionospheric current with the electric field and the height integrated Pedersen as well as Hall conductivities by equation (6.20).

Although the electric field in the ionosphere is not constant in the short time scale considered in this study, i.e., a few seconds, chapter 6 shows that equation (6.20) is reasonably satisfied if we use the value of the electric field at altitudes below 120 km. The reason is that the large value of the Pedersen and Hall conductivities is very localized at the lower E

region of the ionosphere and the electric field is relatively constant at lower altitudes (below 120 km), so the contribution of the height integrated ionospheric current is mostly from the lower E-region. As discussed in chapter 6, the assumption used in most global scale ionosphere-magnetosphere coupling models, i.e., the magnetic field lines are equal potential such that one can map the electric field in the magnetosphere down to the ionosphere, is invalid in the small spatial and fast temporal scale structures. The height integral of the ionospheric current is wrong when the electric field in the magnetosphere is used. In addition, neglecting the averaging over time and horizontal spatial scales in the calculation of the height integrated ionospheric currents is also unreasonable.

The usual way to derive the ionospheric conductivities does not include the effect from the plasma pressure gradient. The analysis I carried out in chapter 6 shows that there is a Hall like term from the electron pressure gradient contributing to the ionospheric Hall current. This causes the difference between the real height integrated Hall current and the current of the Hall component obtained from the electric field and height integrated ionospheric conductivities at the location where there is a large electron pressure gradient. The plasma pressure is insignificant for the height integrated Pedersen current.

7.3 Future work

This thesis shows some important new results concerning ionosphere-magnetosphere coupling processes using the newly developed two-dimensional three-fluid ionosphere model. This model enables us to quantitatively simulate dynamics of small scale two-dimensional ionospheric structures, such as the field-aligned current layers related to discrete auroral arcs. The results demonstrate the capabilities and potential of the model for ionosphere-magnetosphere coupling processes, with the emphasis on the ionospheric dynamics.

But the real ionosphere is a three dimensional system. Most of the ionospheric phenom-

ena, for instance, the curl and vortex structures in the discrete aurora, are three dimensional structures. Although I have studied the mechanism for tall auroral rays, it also is really a three dimensional problem. The interesting result of the formation of the plasma density hole at the base of the downward field-aligned current layer also needs to be verified in a three dimensional calculation. Thus, a three-dimensional model is needed to fully address the ionospheric dynamics. Otto and Birk [1993] have studied the formation of the thin discrete auroral arcs by a simplified three dimensional MHD model. They proposed a mechanism to illustrate the formation of the thin auroral arcs. But in their model, the ionosphere was treated as a boundary, important ionospheric physical processes such as particle precipitation and recombination were not included, and the plasma-neutral collision frequencies were also not calculated self-consistently. Since we have developed a good two-dimensional quantitative ionosphere-magnetosphere coupling model in the work of this thesis, it is desirable to extend this into three dimensions.

7.4 Conclusion

A quantitative time dependent two dimensional three-fluid ionospheric model was developed for the study of the small scale ionosphere-magnetosphere coupling processes, with emphasis on the ionospheric dynamics. This is the first model that can resolve the dynamic and nonlinear electromagnetic interaction between the ionosphere and the magnetosphere. The results of the ionospheric heating simulation quantitatively agree well with optical and radar (EISCAT) observations. The field-aligned current simulation shows new, interesting results, such as the plasma density hole formation at the base of the downward field-aligned current layer, the widening of the downward field-aligned current layer, and the finite field-aligned current filament at the edge of the sharp boundary of the particle precipitation. All these results have clear physical mechanisms and indicate that the ionosphere could play a very

important role in the ionosphere-magnetosphere coupling system.

Bibliography

Akasofu, S.-I., The development of the auroral substorm, *Planet. Space Sci.*, *12*, 273, 1964.

Akasofu, S.-I., The magnetospheric current: an introduction, *Magnetospheric current, edited by T.A. Potemra*, p. 29, 1984.

Atkinson, G., Auroral arcs: results of the interaction of a dynamic magnetosphere with the ionosphere, *J. Geophys. Res.*, *75*, 4746, 1970.

Axford, W., Magnetospheric convection, *Rev. Geophys.*, *7*, 421, 1969.

Birk, G. and A. Otto, A three-dimensional plasma-neutral gas-fluid code, *J. Comp. Phys.*, *125*, 513–525, 1996.

Birk, G. and A. Otto, Consequences of a resistive instability operating in the upper auroral ionosphere, *J. Atmos. Terr. Phys.*, *59*, 835, 1997.

Birn, J., Computer studies of the dynamical evolution of the geomagnetic tail, *J. Geophys. Res*, *85*, 1214, 1980.

Borovsky, J., Auroral arc thicknesses as predicted by various theories, *J. Geophys. Res.*, *98*, 6101, 1993.

Boström, R., Currents in the ionosphere and magnetosphere, *Ann. Geophys.*, *24*, 681, 1968.

Dreher, J., On the self-consistent description of dynamic magnetosphere-ionosphere coupling phenomena with resolved ionosphere, *J. Geophys. Res*, *102*, 85, 1997.

Dungey, J., Interplanetary magnetic field and the auroral zones, *Phys. Rev. Lett.*, *6*, 47, 1961.

Ellis, P. and D. Southwood, Reflection of Alfvén waves by non-uniform ionospheres, *Planet. Space Sci.*, *31*, 107, 1983.

Fuller-Rowell, T. and D. Rees, A three-dimensional and time-dependent global model of the thermosphere, *J. Atmos. Sci.*, *37*, 2545, 1980.

Haerendel, G., Acceleration from field-aligned potential drops, *Astrophys. J. Suppl.*, *90*, 765, 1994.

Harel, M., R. Wolf, P. Reiff, R. Spiro, W. Burke, F. Rich, and M. Smiddy, Quantitative simulation of a magnetospheric substorm, 1, model logic and overview, *J. Geophys. Res*, *86*, 2217, 1981.

Hedin, A., Extension of the MSIS thermosphere model into the middle and lower atmosphere, *J. Geophys. Res*, *96*, 1159–1172, 1991.

Hughes, W. and D. Southwood, The screening of micropulsation signals by the atmosphere and ionosphere, *J. Geophys. Res*, *81*, 3234, 1976.

Iijima, T., Field-aligned current during northward IMF, *Magnetospheric current, edited by T.A. Potemra*, p. 115, 1984.

Iijima, T. and T. Potemra, Large-scale characteristics of field-aligned currents associated with substorms, *J. Geophys. Res*, *83*, 599, 1978.

Johnson, F., *Satellite Environment Handbook.* Stanford Univ. Press, Stanford, California, 1961.

Kan, J., A global magnetosphere-ionosphere coupling model of substorms, *J. Geophys. Res*, *98*, 17263, 1993.

Kelley, M., *The earth's ionosphere.* Academic Press, Inc, San Diego, California, p. 40, 1989.

Lanchester, B. and M. Rees, Field-aligned current reversals and fine structure in a dayside auroral arc, *Planet. Space Sci.*, *35*, 759, 1987.

Lanchester, B., J. Palmer, M. Rees, D. Lummerzheim, K. Keila, and T. Turner, Energy flux and characteristic energy of an elemental auroral structure, *Geophys. Res. Lett.*, *99*, 2789, 1994.

Lanchester, B., M. Rees, D. Lummerzheim, A. Otto, H. Frey, and K. Kaila, Large fluxes of auroral electrons in filaments of 100 m width, *J. Geophys. Res.*, *102*, 9741, 1997.

Lanchester, B., M. Rees, K. Sedgemore, J. Palmer, H. Frey, and K. Kaila, Ionospheric response to variable electric fields in small-scale auroral structures, *Ann. Geophys.*, *16*, 1343, 1998.

Lanchester, B., D. Lummerzheim, A. Otto, M. Rees, K. Sedgemore-Schulthess, H. Zhu, and I. McCrea, Ohmic heating as evidence for strong field-aligned currents in filamentary aurora, *J. Geophys. Res.*, *submitted*, 1999.

Link, R., Feautrier solution of the electron transport equation, *J. Geophys. Res.*, *97*, 159, 1992.

Lummerzheim, D., Comparison of energy dissipation functions for high energy auroral elec-

tron and ion precipitation, Technical Report UAG-R-318, Geophysical Institute Report, University of Alaska Fairbanks, 1992.

Lummerzheim, D. and J. Lilensten, Electron transport and energy degradation in the ionosphere: evaluation of the numerical solution, comparison with laboratory experiments and auroral observations, *Ann. Geophys.*, *12*, 1039–1051, 1994.

Lyons, L., The geospace modeling program grand challenge, *J. Geophys. Res.*, *103*, 14781–14785, 1998.

Maggs, J. and T. Davis, Measurements of the thickness of auroral structures, *Planet. Space Sci.*, *16*, 205, 1968.

Maltsev, Y., W. Lyatsky, and A. Lyatskaya, Currents over the auroral arc, *Planet. Space Sci.*, *25*, 53, 1977.

Mantas, G., Theory of photoelectron thermalization and transport in the ionosphere, *Planet. Space Sci.*, *22*, 337, 1974.

Maurits, S. and B. Watkins, UAF eulerian model of the polar ionosphere, *STEP Handbook of ionospheric models, edited by R.W. Schunk*, p. 95, 1996.

Nagy, A. and P. Banks, Photoelectron fluxes in the ionosphere, *J. Geophys. Res.*, *75*, 6260, 1970.

Newell, P., New findings about auroras confirm importance of ionosphere in space weather, *EOS Trans. AGU*, *79*, 51, December 22, 1998.

Newton, R., D. Southwood, and W. Hughes, Damping of geomagnetic pulsations by the ionosphere, *Planet. Space Sci.*, *26*, 201, 1978.

Nishida, A., *Geomagnetic Diagnosis of the Magnetosphere.* Springer-Verlag, New York, p. 129, 1978.

Opgenoorth, H., I. Häggström, P. Williams, and G. Jones, Regions of strongly enchanced perpendicular electric field adjacent to aurora arcs, *J. Atmos. Terr. Phys.*, *52*, 458–499, 1990.

Otto, A. and G. Birk, The dynamical evolution of small-scale auroral arc phenomena due to a resistive instability, *J. Geophys. Res.*, *97*, 8391, 1992.

Otto, A. and G. Birk, Formation of thin auroral arcs by current striation, *Geophys. Res. Lett.*, *20*, 2833, 1993.

Otto, A., H. Zhu, D. Lummerzheim, Ø. Lie-Svendsen, M. Rees, and B. Lanchester, F region electron heating and O(^{1}D) emission caused by intense field-aligned currents, *Geophys. Res. Lett.*, *submitted*, 1999.

Papadopoulos, K., A review of anomalous resistivity for the ionosphere, *Rev. Geophys. Space Phys.*, *15*, 113, 1977.

Potter, D., *Computational Physics.* Wiley London, p. 63, 1973.

Raeder, J., J. Berchem, and M. Ashour-Abdalla, The importance of small scale processes in global MHD simulations: Some numerical experiments, in: The physics of space plasmas, *T. Chang and J. R. Jasperse, editors*, *14*, 403, 1996.

Raeder, J., J. Berchem, and M. Ashour-Abdalla, The geospace environment modeling challenge: Results from a global geospace model, *J. Geophys. Res.*, *103*, 14787–14797, 1998.

Rees, M. and R. Roble, Excitation of O(^1D) atoms in aurora and emission of the [OI] 6300-Å line, *Can. J. Phys.*, *64*, 1608, 1986.

Reiff, P., R. Spiro, and T. Hill, Dependence of polar-cap potential drop on interplanetary parameters, *J. Geophys. Res.*, *86*, 7639, 1981.

Roble, R., The NCAR thermosphere-ionosphere-mesosphere-electrodynamics general circulation model (TIME-GCM), *STEP Handbook of ionospheric models, edited by R.W. Schunk*, pp. 281–288, 1996.

Roble, R. and M. Rees, Time-dependent studies of the aurora: Effects of particle precipitation on the dynamic morphology of ionospheric and atmospheric properties, *Planet. Space Sci.*, *25*, 991–1010, 1977.

Roble, R., E. Ridley, and R. Dickinson, On the global mean structure of the thermosphere, *J. Geophys. Res.*, *92*, 8745–8758, 1987.

Rostoker, G. and R. Boström, A mechanism for driving the gross Birkeland current configuration in the auroral oval, Technical Report TRITA-EPP-74-25, Dept. Plasma Phys. Royal Inst. Tech, Stockholm, Sweden, 1974.

Sagdeev, R. and A. Galeev, *Nonlinear plasma theory.* W.A. Benjamin, 1969.

Schunk, R., *The terrestrial ionosphere Solar-terrestrial physics.* D. Reidel, p. 609-676, 1983.

Schunk, R., A mathematical model of the middle and high latitude ionosphere, *PAGEOPH*, *127*, 255, 1988.

Seyler, C., Nonlinear 3-D evolution of bounded kinetic Alfvén waves due to shear flow and collisionless tearing instability, *Geophys. Res. Lett.*, *15*, 756, 1988.

Seyler, C., A mathematical model of the structure and evolution of small-scale discrete auroral arcs, *J. Geophys. Res.*, *95*, 17199, 1990.

Slinker, S., J. A. Fedder, B. A. Emery, K. B. Baker, D. Lummerzheim, J. G. Lyon, and F. J. Rich, Comaprison of global MHD simulations with AMIE simulations for the events of 19-20 May, 1996, *submitted*, 1999.

Sojka, J., Global scale, physical models of the F region ionosphere, *Rev. Geophys.*, *27*, 371, 1989.

Spiro, R., M. Harel, R. Wolf, and P. Reiff, Quantitative simulation of a magnetospheric substorm – 3. plasmasphere electric fields and evolution of the plasmapause, *J. Geophys. Res.*, *86*, 2261–2272, 1981.

Stasiewicz, K. and T. Potemra, Multiscale current structures observed by Freja, *J. Geophys. Res*, *103*, 4315, 1998.

Stasiewicz, K., G. Holmgren, and L. Zanetti, Density depletions and current singularities observed by Freja, *J. Geophys. Res*, *103*, 4251, 1998.

Størmer, C., *Polar Aurora*. Claredon Press, Oxford, UK, 1955.

Strickland, D., D. Book, T. Coffey, and J. Fedder, Transport equation techniques for the deposition of auroral electrons, *J. Geophys. Res*, *81*, 2755, 1976.

Treumann, R. and W. Baumjohann, *Advanced Space Plasma Physis*. Imperial College Press, London, UK, 1997.

Vasyliunas, V., *Mathematical models of magnetospheric convection and its coupling to the ionosphere, in Particle and Fields in the Magnetosphere*. D. Reidel, Dordrecht, Netherlands, p. 60, 1970.

Vasyliunas, V., *Earth's Magnetospheric Processes*. D. Reidel, Hingham, Mass., p. 29, 1972.

Vasyliunas, V., Fundamentals of current description, *Magnetospheric current, edited by T.A. Potemra*, p. 63, 1984.

Wolf, R., Ionosphere-magnetosphere coupling, *Space Sci. Rev.*, *17*, 537, 1975.

Wolf, R., M. Harel, R. Spiro, G. H. Voigt, P. Reiff, and C. K. Chen, Computer simulation of inner magnetospheric dynamics for the magnetic storm of July 29, 1977, *J. Geophys. Res*, *87*, 5949, 1982.

Yark, J. and D. Southwood, The effect of non-uniform ionospheric conductivity on standing magnetospheric Alfvén waves, *Planet. Space Sci.*, *34*, 1213–1221, 1986.

Zhu, H., A. Otto, M. Rees, B. Lanchester, and D. Lummerzheim, Ionosphere-magnetosphere simulation of small scale structure and dynamics, *J. Geophys. Res*, *submitted*, 1999.

Zhu, H., A. Otto, M. Rees, B. Lanchester, and D. Lummerzheim, Field-aligned currents and their effects in the ionosphere: 2D simulation results, *J. Geophys. Res*, *to be submitted*, 2000.

Zmuda, A., J. Martin, and F. Heuring, Transverse magnetic disturbances at 1100 km in the auroral region, *J. Geophys. Res*, *71*, 5033, 1966.